Mechanical behaviour of human epidermal and dermal layers in vivo

CIP-DATA LIBRARY TECHNISCHE UNIVERSITEIT EINDHOVEN

Hendriks, Falke M.

Mechanical behaviour of human epidermal and dermal layers in vivo /
by Falke M. Hendriks. – Eindhoven : Technische Universiteit Eindhoven,
2005.
Proefschrift. – ISBN 90-386-2896-X
NUR 954
Subject headings: skin mechanics / epidermis / ultrasound / optical
coherence tomography / confocal microscopy / finite element model

Cover design: Jan-Willem Luijten (JWL producties)/Falke Hendriks

Printed by Universiteitsdrukkerij TU Eindhoven, Eindhoven, The Netherlands.

This project was financially supported by Philips Research.

Mechanical behaviour of human epidermal and dermal layers in vivo

Proefschrift

ter verkrijging van de graad van doctor
aan de Technische Universiteit Eindhoven,
op gezag van de Rector Magnificus, prof.dr. R.A. van Santen,
voor een commissie aangewezen door het College voor Promoties
in het openbaar te verdedigen op
dinsdag 22 maart 2005 om 16.00 uur

door

Falke Marieke Hendriks

geboren te Sittard

Dit proefschrift is goedgekeurd door de promotoren:

prof.dr.ir. F.P.T. Baaijens
en
prof.dr. D.L. Bader

Copromotor:
dr.ir. C.W.J. Oomens

Voor Ronald,
voor Sterre,
voor mijn ouders.

Contents

Summary

Human skin is the largest organ of the human body. Its mechanical behaviour has been studied for a long time. Knowledge of the mechanical behaviour of the skin *in vivo* is an important consideration in both cosmetic and clinical applications such as the development of creams and personal care products, or in understanding skin diseases and skin ageing. Especially knowledge of the mechanics of the epidermis, the most superficial skin layer, is crucial, since it is the epidermis that interfaces with cosmetic products and where skin diseases manifest. Furthermore, it is well established that the mechanical behaviour of the epidermis is strongly influenced by environmental conditions such as temperature and humidity. In an *in vivo* situation, the epidermis is also hydrated by the underlying dermis, illustrating the need for a non-invasive study on the mechanical behaviour of the different skin layers.

Numerous mechanical experiments have been performed on the skin and many numerical models are proposed to describe the mechanical response of the skin. Common feature of these studies is their assumption that the behaviour of the skin is dominated by the collagen-rich dermis. By contrast, the contribution of the epidermis, with its distinctive structural composition, is largely ignored.

The aim of this study was to examine the mechanical behaviour of different layers of the skin *in vivo*, including the uppermost layers. The work was based on the hypothesis that a combination of suction experiments at different aperture diameters can be used to study the mechanical behaviour of these different skin layers. This means that a small aperture diameter can be used to study the mechanical behaviour of the upper layers of the skin, whereas a large aperture diameter can be employed to examine the mechanical behaviour of the deeper layers of the skin.

Three experimental set-ups were developed combining a mechanical experiment and an imaging technique to visualize the deformation in the skin. Each set-up was designed to examine different skin layers. Various finite element models were developed to describe the experiments and to characterize the mechanical behaviour of the different layers. A suction device with a 6 mm diameter aperture was combined with ultrasound to study the mechanical behaviour of the subcutaneous fat and the skin composite, defined as the combined epidermis and dermis. Suction measurements at varying pressures were performed on the volar forearm skin of 10 subjects aged 19 to 24 years old. Deformation of these layers due to suction was visualized using ultrasound. The experiment was simulated by a finite element model exhibiting extended Mooney material behaviour to account for

the non-linear stress-strain relationship. An identification method was used to compare the experimental and numerical results to identify the parameters of the material model, C_{10} and C_{11}. This resulted in $C_{10} = 9.4 \pm 3.6$ kPa and $C_{11} = 82 \pm 60$ kPa for the skin composite. A first estimate for the fat layer was $C_{10,fat} = 0.02$ kPa.

The contribution of the epidermis and the dermis to the mechanical response of the skin was examined with a suction device with 1, 2 and 6 mm diameter apertures. Suction measurements at varying pressures and aperture sizes were performed on the volar forearm of 13 subjects aged 29-47 years. The deformation of the skin composite was visualized using ultrasound. Optical coherence tomography (OCT) visualized the deformation of the epidermis and the papillar dermis, defined as the upper layer. Ultrasound measurements (6 mm aperture diameter) were performed on hydrated skin, OCT measurements on dry and hydrated skin. Hydration caused ambiguous effects on the mechanical response.
The experiments were simulated by a single layer finite element model representing the skin composite and exhibiting extended Mooney material behaviour. It appeared that ultrasound and OCT combined with suction at varying apertures sizes can be used to differentiate the mechanical behaviour of different skin layers. With increasing aperture diameter, increasing values for material parameters were found although the same material was modelled.

Therefore, the experiments were modelled for small displacements with a two-layered finite element model, representing the upper layer and the reticular dermis to characterize the mechanical behaviour of these layers. Large difference was found in the material parameters for the upper layer and the reticular dermis with estimated values for C_{10} of 0.16 MPa and 0.11 kPa, respectively. The two-layer model was successful in predicting the response in the 1 and 6 mm, but less so for the 2 mm aperture diameter experiment, although these results were explored merely for one subject. Due to the large difference in the stiffness, the existing software that supported the two-layer model could not account for large displacements, which were produced with some of the individuals.

As the resolution of the OCT system did not allow the use of smaller aperture sizes, a third imaging system was needed to examine deformations in the various epidermal layers. A small tensile device was developed that was coupled to a confocal microscope. Three-dimensional image correlation was successfully applied to images up to 160 μm under the skin surface to acquire three-dimensional deformation and strain fields in the epidermis and papillar dermis. Although this technique is promising, several improvements are needed before it can be employed to characterize the mechanical behaviour of the epidermal layers.

In conclusion, the developed techniques used in this study combining experiments of different length scales have proven to be useful tools to examine the mechanical behaviour of different skin layers, including the top layers.

Chapter 1

Introduction

The skin is the largest organ of the human body and it has several functions. The most important is to protect the body against external influences. The mechanical behaviour of skin is an important consideration in a number of cosmetic and clinical implications. For example, knowledge of its mechanical behaviour can help to quantify effectiveness of cosmetic products such as creams, to enhance new developments in electrical personal care products such as shavers, and to study skin ageing. Also improvements in cosmetic surgery can be gained with prediction of surgery results by using numerical models of the skin. Finally, changes in mechanical properties of the skin due to skin diseases may play a role in a better understanding and treatment of these diseases.

In particular the barrier function of skin, which protects the body by preventing fluid loss and the penetration of undesirable substances, is primarily fulfilled by the top layer. In addition, it is the top layer that interfaces with cosmetic products like creams or personal care devices such as shavers. Further clinical problems, such as the development of pressure ulcers is a direct result of breakdown at the interface between the top layer of the skin and its external environment.

Many experiments have been performed on skin and numerous models were developed to describe the complex mechanical behaviour of the skin. None however, takes the layered structure of the skin into account, although it is recognized that the mechanical behaviour varies considerably among the layers. Furthermore, it is well established that the mechanical behaviour of the uppermost layers of the skin is strongly influenced by environmental factors such as temperature and humidity (Wilkes et al., 1973). These changes can only be evaluated in an *in vivo* situation, and this illustrates the need for an experimental system to measure the mechanical behaviour of the top layer and the deeper layers of the skin in a non-invasive manner.

The aim of this thesis is to gain a better understanding in the mechanical behaviour of the skin by characterizing the mechanical behaviour of several distinct skin layers, including the uppermost layers *in vivo*. To achieve this, several experimental set-ups were developed to load the skin mechanically and finite element models were developed to describe the experiments and characterize the mechanical behaviour of the skin layers.

In the following sections, the the structure of the skin, some methods to visualize the skin layers and some experiments and models on the mechanical behaviour of the skin are reviewed to enhance a better understanding of the methods that were used to achieve this aim.

1.1 Structure and function of the human skin

The skin is a highly organized structure consisting of three main layers, called the epidermis, the dermis and the hypodermis (figure 1.1). The superficial layer, the **epidermis**, is approximately 75-150 μm in thickness (Odland, 1991) and consists largely of outward moving cells, the keratinocytes, that are formed by division of cells in the basal layer of the epidermis. The second layer is the **dermis** which is a dense fibroelastic connective tissue layer of 1-4 mm thickness (Odland, 1991). It mainly consists of collagen fibres, ground

substance and elastin fibres and it forms the major mass of the skin. The third layer, the **hypodermis** (or subcutaneous fat) is composed of loose fatty connective tissue. Its thickness varies considerably over the surface of the body.

There are two main kinds of human skin. **Glabrous skin** with its characteristic dermatoglyphics (the grooves on the surface) is found on the palms and the soles. It is characterized by a relatively thick epidermis and lack of hair follicles. In the present study, only **hairy skin** is considered which covers the remaining part of the body and contains hair follicles. However, hairs and hair follicles are ignored.

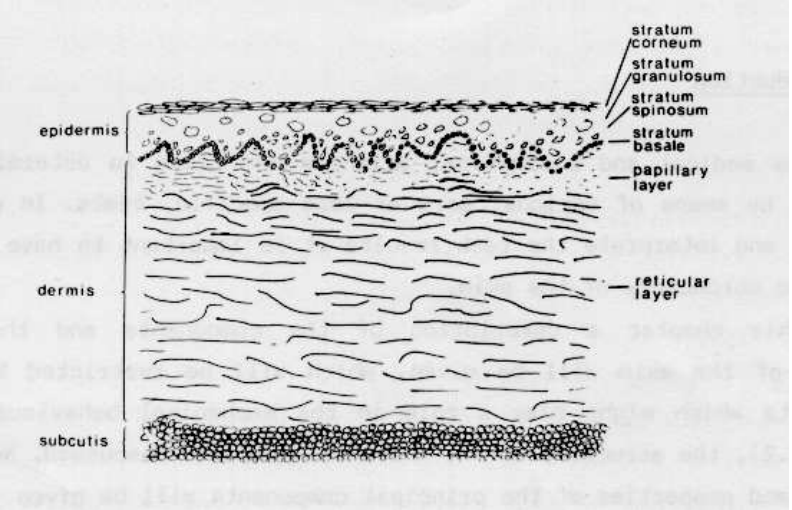

Figure 1.1: *Schematic view of the cross-section of human skin showing the distinct layers. Obtained from Manschot (1985).*

1.1.1 Epidermis

The epidermis consists of keratinocytes which change in cellular constituents as they move peripherically. This results in several well-defined layers (figure 1.2). The deepest layer is the **stratum basale** (or stratum germanitivum) in which cell division occurs. It consists of 1-3 layers of small cuboidal cells with large nuclei and cytoplasm. As the cells move towards the surface, they become larger to form the **stratum spinosum**. The polyhedral cells of the stratum spinosum are connected by desmosomes. Their shape becomes more flattened as they move outward. In the **stratum granulosum** the degradation of mitochondria and nuclei starts and the cytoplasm of the flattened cells becomes almost filled by keratohyalin masses and filaments. Also the cell membranes become gradually thicker. The most superficial layer, the **stratum corneum** consists of 15-20 layers of dead a-nucleate cells that are hexagonal thin flat squames. At this stage the cells are terminally differentiated keratinocytes, called corneocytes.

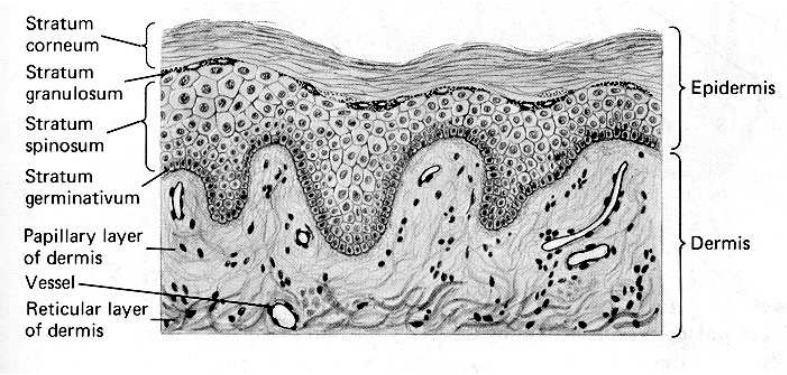

Figure 1.2: *Schematic view of the cross-section of the upper part of the human skin showing the epidermis and part of the dermis. The papillae are the folds at the interface between the dermis and the epidermis. Obtained from Guyton (1985).*

1.1.2 Dermis

Human dermis makes up the bulk of the human skin and contributes to 15-20% of the total body weight. It contains a lot of irregularities such as blood vessels, lymph vessels, nerve endings and the skin appendages such as hair follicles, small hair muscles, sebaceous glands and sweat glands. These irregularities are ignored in the remaining part of this thesis.
The dermis is a moderately dense connective tissue which consists of three fibrin proteins, namely collagen, elastin and minute quantities of reticulin and a supporting matrix or ground substance. Collagen comprises about 75% of the fat free dry weight and 18-30% of the volume of dermis (Ebling et al., 1992). Finlay (1969) showed that the collagen fibre bundles form an irregular network that runs almost parallel to the epidermal surface. Interwoven among the bundles of collagen, is a network of elastin that restores the normal fibrous array following its deformation by external mechanical forces. These elastic fibres contribute to 4% of the fat free dry weight and 1% of the volume of dermis (Ebling et al., 1992). According to Oxlund et al. (1988) direct connections between elastin and collagen fibres have not been shown, but collagen fibrils appear to wind around the elastin cores. At extension rates of about 1.3, the undulated collagen fibrils are straightened.
The amorphous ground substance is composed of glycosaminoglycans, long chains of polysaccharides, which are able to bind a high amount of water. Together they form a gel which does not leak out of the dermis, even under high pressure.

The dermis is arbitrarily divided into two anatomical regions: the **papillary dermis** and the **reticular dermis** (figure 1.1). The papillary dermis is the thinner outermost portion of the dermal connective tissue, constituting approximately 10% of the thickness of the dermis. It contains smaller and more loosely distributed elastic and collagen fibrils than the underlying reticular dermis and it has a greater amount of ground substance. The reticular dermis constitutes the greater bulk of the dermis. This dense collageneous and elastic connective tissue contains a relatively small amount of cells and veins.

The **dermo-epidermal junction** connects the epidermis and the dermis. The junction

provides a physical barrier for cells and large molecules and forms a strong bandage between the dermis and the epidermis by macromolecular attachments. The firmness of the attachment is enhanced by parts of the epidermis penetrating the papillary dermis resulting in large cones and rete ridges, or **papillae**, which can be clearly seen in figure 1.2 (Odland, 1991; Ebling et al., 1992).

1.1.3 Hypodermis

The subcutaneous fat or hypodermis is a fibrofatty layer which is loosely connected to the dermis. Its thickness varies with anatomical site, age, sexe, race, endocrine and nutritional status of the individual. It acts as an insulating layer and a protective cushion and constitutes about 10% of the body weight.

1.2 Skin imaging

The descriptions of the skin structure in the previous section are based on histology: microscopic images of preparations of sections of dead skin which are usually performed perpendicular to the skin surface. To image the skin in a less time consuming way and without taking biological biopsies, various non-invasive *in vivo* skin imaging techniques have been developed.

1.2.1 Ultrasound

Ultrasound is an acoustic technique, which can be used to image the skin perpendicular to its surface. By varying frequency either high resolution (up to 11 μm for high frequencies) or large penetration depth (up to 6 cm for low frequency) can be achieved (Serup et al., 1995).
The physical principle of an ultrasound scanner is the emission of high frequency acoustic waves, caused by electrical signals in a piezo-electric ultrasound transducer. An alternating electric field causes thickness variations in the piezo-electric material. The thickness variations cause pressure waves in the surrounding coupling agent (mostly water): the ultrasound. At each interface between different tissues in the skin, a change in the acoustic impedance of the tissue causes some of the sound to be reflected back to the transducer, while the rest of the energy continues to the next interface. The amount of sound being reflected depends on the difference in acoustic impedance of the materials, with large reflections for increasing differences.
The sound-emission is pulsed, which means that the equipment switches automatically and very rapidly between emission of sound and the registration of sound coming back to the same transducer from the object being studied. The result is a train of pulses returning to the transducer. The time lag between emitted and reflected sound waves is a measure for the travelled distance. It depends on the physical distance between the interfaces and on the tissue material, and can be converted into a distance once the speed of the sound is

known. Estimates of the sound velocity in skin are: stratum corneum 1550 m/s; epidermis 1540 m/s; dermis 1580 m/s and subcutaneous fat 1440 m/s (Edwards and Payne, 1984). The average for normal full-thickness skin is 1577 m/s. Ultrasound velocity of 1580 m/s is commonly used for the calculation of total skin thickness (Serup et al., 1995). Other studies showed that ultrasound velocity depends on body region. Escoffier et al. (1986) found an average of 1605 m/s and Dines et al. (1984) found 1710 m/s for abdominal skin. From a practical point of view, a minor deviation of ultrasound velocity from the true value of a particular location will not influence significantly the result of the thickness measurement, expressed in millimeters to one decimal point.
A two-dimensional image of the skin is obtained by automatically moving the transducer over the skin. The one dimensional pulse trains are processed electronically to obtain a cross-sectional image of the skin (figure 1.3).

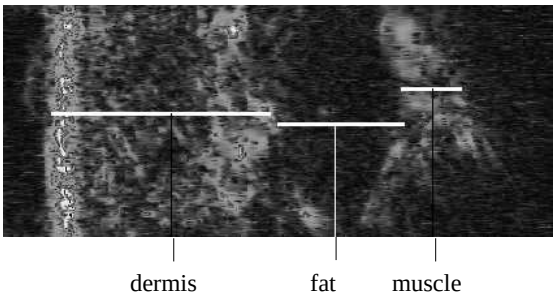

Figure 1.3: *Ultrasound image of the forearm skin showing the entrance echo corresponding to the epidermal surface, the echo-rich dermis, the echo-poor subcutaneous fat and the echo-rich underlying muscle.*

The used ultrasound frequency is a compromise between desired resolution and penetration depth. Axial resolution is defined by the ratio of sound velocity and the ultrasound frequency. Tissue penetration improves with lower frequencies, whereas higher frequencies lead to a better resolution. Ultrasound waves of 10 MHz penetrate deep enough to visualize the subcutaneous fat, while ultrasound waves of 50 MHz allow a more detailed study of the epidermis. Frequencies from 15 to 20 Mhz are mostly used for the skin as they provide a good compromise between resolution and viewing depth to visualize the entire skin. Generally, 20 MHz scanners have an axial resolution of 0.07 mm in skin and a lateral resolution of 0.15-0.35 mm. The viewing field of depth is typically 15-25 mm (Serup et al., 1995; Agner, 1995). At this frequency, differentiation between epidermis and dermis by ultrasound is difficult because the thickness of the epidermis is close to that of the system's resolution.

A high-resolution ultrasound system to study the epidermis was developed by El Gammal et al. (1995). With a 50 MHz transducer an axial resolution of 39 μm could be obtained and with a 100 MHz transducer they obtained an axial resolution of 11 μm. Thickness measurements of all parts of the epidermis using 50 MHz ultrasound correlated well with histometry, except for the stratum corneum which could not be sufficiently resolved, because the thickness of this layer is too small compared to the axial resolution of the transducer.

Ultrasonography is not directly comparable to microscopy as some structures are better visualized by ultrasound than histology and vice versa. *In vivo* 20 MHz ultrasound examination does not have the resolution of histology (Serup et al., 1995). The interface between subcutis and dermis can be clearly identified in all cases, but the dermal-epidermal interface can only be determined for high frequencies ultrasound. The advantage of ultrasound imaging techniques is that it is non-invasive, and therefore no changes occur in the skin due to loss of pretension, blood supply etc.

1.2.2 Confocal microscopy

Confocal microscopy is a very high resolution optical technique that can be used to image the epidermis parallel to the skin surface. Figure 1.4 shows a schematic representation of a backscatter confocal microscope. Excitatory light from a point source is reflected by a dichroic mirror and focused by the microscope objective lens to illuminate a point on the focal plane inside the skin. The illuminated spot is then imaged onto a detector through a pinhole, or point aperture. This aperture acts as a spatial filter, rejecting light that is reflected from out-of-focus portions of the object (dashed line) to fall outside of the focal spot. Only emissions from the focal plane (solid line) are able to pass the aperture, resulting in an image with the high contrast of a thin-section image. By moving the light beam, the desired plane in the specimen can be scanned. In this way a 2D image is obtained. Varying the depth of the focal plane and combining the obtained images computationally, leads to a 3D image (Sheppard and Shotton, 1997; Rajadhyaksha and Zavislan, 1997).

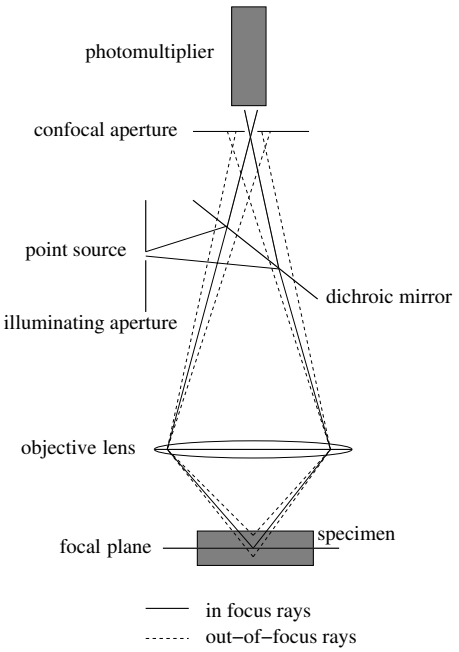

Figure 1.4: *Schematic diagram of a backscatter confocal microscope. Adapted from Sheppard and Shotton (1997).*

Signal contrast in confocal reflectance imaging stems from variations in the refractive-index of the cell structure. This causes differences in reflection, resulting in varying gray scales. Because of the high scattering coefficient of the skin, the maximum penetration depth in skin is in the order of 250-300 μm and a vertical resolution up to 2 μm can be obtained. The various epidermal layers can be distinguished and sizes of the cellular nuclei can be obtained. Even blood cells flowing through the capillary loops of the papillary dermis can be observed in real time.
The performance of the confocal system is mainly determined by the aperture size and the illumination wavelength. Increasing the wavelength leads to deeper penetration and a decreasing lateral and axial resolution (thus increasing section thickness), (Rajadhyaksha and Zavislan, 1997). Small apertures provide good sectioning, whereas large apertures collect more light (Rajadhyaksha et al., 1999a).

Confocal images at several depths show the stratum corneum, the layers of the viable epidermis and the dermal papillae (figure 1.5).

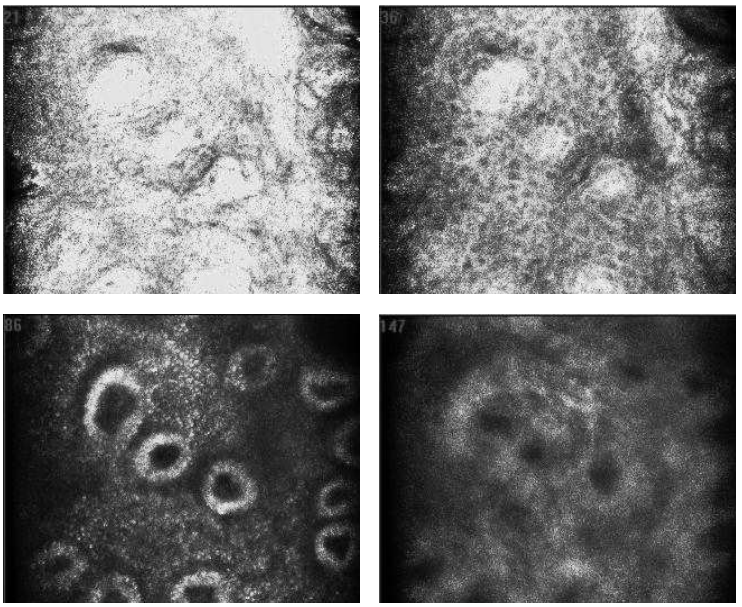

Figure 1.5: *Confocal images at various depths under the skin surface, showing the stratum corneum (upper left), the spinous layer (upper right), the highly reflective basal cells around the papillae (lower left) and the collagen bundles in the dermis (lower right). Adapted from Lucassen et al. (2002).*

In classical histology vertical sections of the skin are made whereas with confocal microscopy horizontal images are made. Therefore, direct comparison is difficult. Rajadhyaksha et al. (1999b) made horizontal histology sections of human skin to make a direct comparison. In confocal images stratum corneum appeared different from that in histology, probably due to lateral and vertical stretching in histology (Rajadhyaksha et al., 1999b). Confocal images of the granular, spinous and basal cell layers correlated well with histology (Rajadhyaksha et al., 1999b).

As confocal images are completely noninvasive, they are free from the artifacts of histology (such as biopsy, fixing, sectioning and staining, all leading to cell degeneration including shrinkage). Artifacts in confocal microscopy can emerge as bright or dark spherical disks on the skin surface due to bubbles or dirt in the immersion medium.

1.2.3 Optical coherence tomography

OCT is an interferometric method which supplies information about optical inhomogeneities of the tissue. Both lateral and axial resolution are in the order of 10-20 μm, whereas the penetration depth is in the order of 1-2 mm (Pan et al., 1996). OCT images are represented as two-dimensional cross-sectional images, which can be compared with high frequency ultrasound scans, but represent optical and not acoustic inhomogeneities of the tissue.

The OCT system is based on the principle of the Michelson interferometer. An example of a system setup is given in figure 1.6.

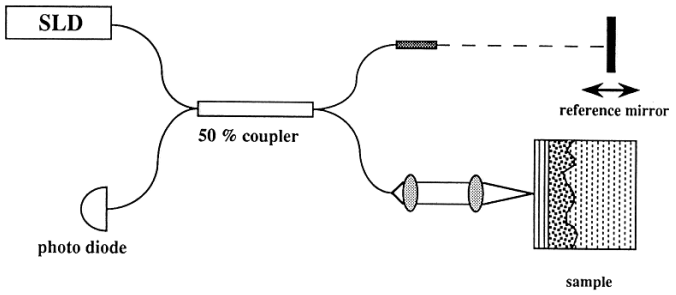

Figure 1.6: *Schematic diagram of the OCT system. Obtained from Welzel et al. (1998).*

Usually the light source is a superluminence diode (SLD) with a wavelength in the near infrared (approximately 1300 nm) and with a short coherence of about 15 μm. The light is coupled into a single-mode fiberoptic interferometer. Within the first interferometer arm, the reference arm, the light is collimated and directed through a scanning mirror system to a reference mirror mounted on a stepper motor. The position of the reference mirror determines the scan position. The light in the sample arm, the second interferometer arm, is focused onto the spot of interest at the tissue sample. The backscattered light from the tissue sample is collected through the same optics and recombined with reflected light from the scanning reference mirror system at two detectors. Coherent interference signal occurs only when the path length between those arms are matched to within the coherence length of the light source.
The axial resolution of the system is determined by the coherence length of the light in biological tissue, while the lateral resolution is given by the focal spot size (Pan et al., 1996).

Skin of the volar forearm has been studied with OCT by amongst others Schmitt et al. (1995), Pan et al. (1996) and Welzel et al. (1998). They claimed to be able to visualize

the dermo-epidermal junction in skin with a wide range of epidermal thicknesses, and thus epidermal thickness could be measured using OCT. The stratum corneum could not be detected and no fine structure could be seen in the reflections of the dermis.

OCT images correlate well with histology in all cases. Due to multiple light scattering and a coherence length longer than most cell diameters, OCT can provide less micro-structural details than light microscopy. However, it can show structures which correlate well with ultrasound and histology to a depth of about 600 μm. Like ultrasound and confocal microscopy images, OCT images are free of artifacts induced by histological processing (Pan et al., 1996).

1.2.4 Nuclear magnetic resonance

Nuclear magnetic resonance (NMR) or magnetic resonance imaging (MRI), a form of NMR, can also be used to image the skin. Its performance is comparable to that of ultrasound and OCT.

To study skin structure, a better resolution is needed than can be provided by the conventional 1.5 T NMR scanners that are used in hospitals. Querleux (1995) adapted a standard MR scanner to enable epidermis investigation. He obtained an axial resolution in the order of 35-70 μm and was therefore able to differentiate the epidermis, dermis and hypodermis and a thickened stratum corneum on the palm and heel.
Ginefri et al. (2001) used a high-temperature super conducting (HTS) coil to image human calf skin *in vivo* in a whole-body 1.5 T NMR scanner. They obtained a spatial resolution of 40 μm perpendicular to the skin surface and 80 μm parallel to the skin surface. The slice thickness was 900 μm. With this method, structures such as fine ramifications connected to hair follicles, the papillary dermis and the subcutaneous fat, can be differentiated.

Much of the information obtained by MRI can also be obtained by high frequency ultrasound techniques. Disadvantages of NMR are high cost, special building requirements, importability and its low speed of obtaining images. (Zemtsov, 1995). However, MRI provides better resolution, which can also be obtained by high-resolution ultrasound (but with smaller penetration depths). Other advantages of MRI are the ability to visualize structures in fat and the fact that no coupling liquid is needed.

1.2.5 Selection of visualization techniques

The previously described techniques and their resolution and penetration depth in the skin are shown in figure 1.7. It is impossible to visualize all layers which we are interested in (the stratum corneum, living epidermis, dermis and fat) with sufficient resolution with one imaging method. Therefore, a combination of imaging techniques is desired.

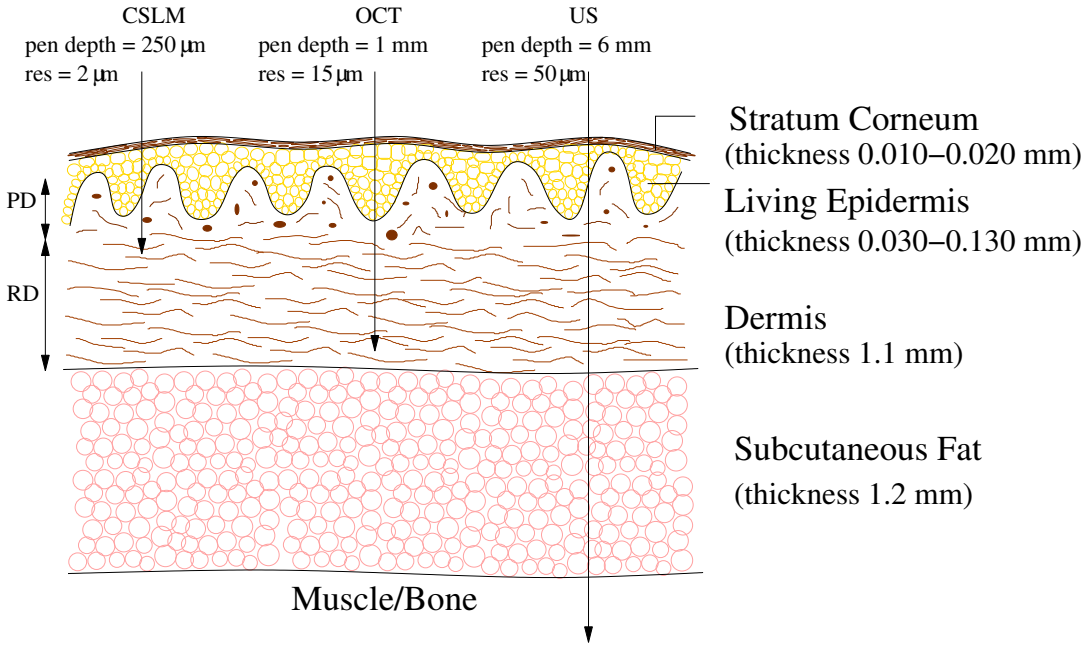

Figure 1.7: *Layer thicknesses of human forearm skin and penetration depth and axial resolution of the various imaging methods.*

For practical reasons it was chosen not to use MRI to image the skin. MRI is expensive, not easy accessible and at present, special skin-surface coils are not commercially available. Therefore, 20 MHz ultrasound was used to visualize the dermis and the subcutaneous fat. With this technique, the epidermis can not be resolved from the dermis. OCT was preferred over high-resolution ultrasound to image the epidermis and part of dermis as OCT does not need a specific coupling liquid, which might affect the mechanical response of the top layers of the skin. This enabled a comparison between measurements with water and air as coupling medium. Finally, confocal microscopy was used to visualize the epidermal layers including the stratum corneum during the mechanical experiments.

1.3 Review of experimental and numerical studies on skin mechanics

Mechanical behaviour of the human skin has been studied for a long time. One of the first investigators was Langer, who punctured skin of human cadavers with a round instrument to study anisotropy in 1861 (Langer, 1861). In the seventies and early eighties of the past century a lot of studies were performed to learn more about skin mechanics (for example by Cook (1976); Wan Abas and Barbanel (1982); Alexander and Cook (1977); Grahame (1970); Barbanel et al. (1972) and Vlasblom (1967)).

They found that human skin is a non-homogeneous, anisotropic, non-linear viscoelastic material which is subjected to a prestress *in vivo*. Its properties vary with age, from site to site and per person. This leads to difficulties in obtaining quantitative descriptions of

mechanical properties of the skin. A second problem is the large variety of instruments, units and measurement conditions that was used which makes it hard to compare results.

In the years that followed, numerous studies were performed with the developed techniques to study effects of age, site, creams etcetera. It was only in the last decade that the availability of new techniques (such as skin imaging techniques and the wide use of computers), gave a new impulse to develop new methods to improve the knowledge of skin mechanics.

Although the stratum corneum is believed to be stiffer than the dermis, usually the contribution of the epidermis to the mechanical properties of full thickness skin is neglected (Wilkes et al., 1973). It seems that biomechanical properties determined from testing whole skin are mainly due to the dermal collagen, since similar results are obtained from collagen tests (Marks, 1991). Only few authors do recognize the influence of the stratum corneum on the overall mechanical properties of the skin (for example Rigal and Lévêque (1985)).

1.3.1 Mechanical properties of dermal components

To understand the mechanical behaviour of the skin, first the mechanical behaviour of the dermal components will be described (Wilkes et al. (1973), Maurel et al. (1998)).

- **Collagen** fibres are the main constituent of the dermis (77% of the fat-free dry weight) and form an irregular network of wavy coiled fibres that run almost parallel with the skin surface (Finlay, 1969). Collagen is characterized by high stiffness (Young's modulus approximately 0.1 GPa (Manschot, 1985) to 1 GPa (Maurel et al., 1998) in the linear region) and low extensibility (rupture at strains in the order of 5-6%).
- **Elastin** fibres are the second main component of the dermis (4% of the fat-free dry weight). They are less stiff than collagen and show reversible strains of more than 100%.
- **Reticulin** is found in much smaller amounts: only 0.4 % of the fat-free dry weight. Mechanical properties of reticulin are not exactly known, but since reticulin has a similar molecular structure and morphology as collagen, the properties are likely to be similar to that of collagen.
- The **ground substance** is responsible for the viscoelastic behaviour of the dermis. It is unlikely that it contributes to the tensile strength of the dermis.

1.3.2 Mechanical experiments on the skin *in vivo*

In most *in vivo* performed experiments, the measured behaviour is ascribed to the dermis. However, as intimate connections exist between the various skin layers, it is hard to isolate the contribution of the dermis to the mechanical behaviour from that of the epidermis and the subcutaneous tissues. Therefore, most tests performed *in vivo* are, in part, also tests of epidermal, stratum corneum and hypodermal properties.

In **tensile** testing the skin is mainly loaded parallel to its surface. This type of mechanical testing is widely used. Two tabs are attached to the skin and pulled apart. The attachment of the tabs to the skin may significantly influence the results as many of the double-sided adhesive tapes exhibit creep deformation. Rapidly bonding cyanoacrylate adhesives can be used to avoid these effects.
A typical example of a uniaxial tensile test is described by Manschot and Brakkee (1986). They performed uniaxial tensile tests on human calf, both across and along the tibial axis. Two square tabs (10×10 mm^2) were attached to the skin with cyanoacrylate adhesive with a distance of 5 mm in between. A skin thickness of 1.2 mm was measured with ultrasound. Four sawtooth shaped loads (maximum 12 N) were applied with a loading and interval time of respectively 10 and 20 seconds. Preconditioning is left out of consideration by neglecting the response to the first load cycle.
A clear non-linear stress-strain relationship was observed. Across the tibia axis a maximum strain of 0.32 and a maximum Young's modulus of 4 MPa was found. Along the tibia axis the maximum observed strain and Young's modulus were 0.3 and 20 MPa respectively.

In **torsion** tests a guard ring and an intermediary disc are attached to the skin. A constant torque or rotation is applied by the disc. According to Escoffier et al. (1989) this method has two advantages: hypodermis and underlying tissues do not effect the measurements and the anisotropic character of the skin is minimized.
Agache et al. (1980) studied skin stiffness with an apparatus that is described by Rigal et al. (1980) who used it to study skin ageing. Application of a torque of $28.6 \cdot 10^{-3}$ Nm during 2 minutes to the dorsal forearm skin resulted in a rotation of 2-6°. The torsional moment was applied by a 25 mm diameter disc surrounded by a 35 mm diameter guard ring. Young's moduli, E, were calculated for the linear part of the stress-strain curve and were found to be $E = 4.2 \cdot 10^5$ Pa for people aged less than 30 years old, and $E = 8.5 \cdot 10^5$ Pa for people over 30 years.

The principle of the **suction** method is the measurement of skin elevation caused by application of a partial vacuum (usually in the range of 5-50 kPa or 50-500 mbar) via a circular aperture in a measuring probe. The deformation is measured with an optical or ultrasound system. Two different instruments, both using an optical system, are commercially available: the Dermaflex (Cortex, Denmark) and the Cutometer (Courage & Khazaka Electronic GmbH, Germany).
Gniadecka and Serup (1995) used the Dermaflex with an aperture size of 10 mm. They claim to measure mechanical properties of mainly the dermis, whereas the Cutometer (when used with the smallest available aperture size of 1 mm) is said to measure mechanical properties of epidermis, papillary dermis and to a lesser degree the reticular dermis and the subcutis.
Barel et al. (1995) used the Cutometer which is available with apertures of 1, 2, 4, 6 and 8 mm. With increasing aperture size, deeper skin layers are deformed by suction. Deformation depended on skin thickness and though the pressure-deformation curve was non-linear, a linear part was found between pressures of 150 and 500 mbar. In that part,

the Young's modulus was calculated at $13 - 26 \cdot 10^4$ Pa for different anatomical sites and 2 mm aperture. Deformations occurred mainly in the dermis. For large strains, small deformations were found in the subcutis.
Diridollou et al. (1998) developed an echo-rheometer, a suction system with an ultrasound scanner (20 MHz) that enabled simultaneous visualization and measurement of deformation of skin structures *in vivo* with an axial resolution of 0.07 mm. The system was applied to the skin with adhesive tape. Distilled water was used as a coupling liquid. The system enabled measurement of the combined thickness of the epidermis and dermis, and that of the subcutis during the suction experiment. Measurements were performed on the volar forearm with aperture diameters of 2 and 6 mm and suction pressures of 5 and 30 kPa. During high pressure on a large area, the thickness of the subcutis increased with 161% and the combined dermal and epidermal thickness decreased with 9.5%, which may be explained by lateral expansion. With a small pressure applied onto a small area, the subcutaneous thickness increased with 17%, and no modification in dermal thickness was observed. This indicated that even under low stress the behaviour of the dermis and epidermis can not be isolated from that of the subcutis.

In **indentation** experiments a rigid indenter is used to apply a known force or deformation to the skin. Bader and Bowker (1983) used a plane-ended indenter to study mechanical behaviour of skin and underlying tissue. Tissue thickness was measured with a skin fold caliper. A pressure of 11.7 kPa was applied through a 20 mm diameter indenter at the forearm, and 7.0 kPa was applied through a 40 mm indenter to the thigh. Young's moduli of $E = 1.1 - 2.5$ kPa were calculated using the Herzian contact theory for indentation and recovery.

A summary of *in vivo* measured Young's moduli of the skin as presented in this section shows large variations between the used techniques (table 1.1).

Table 1.1: *Summary of in vivo measured Young's moduli of the entire skin.*

method	**Modulus [MPa]**	**test region**	**reference**
tensile	$E_{\parallel} = 20$	leg	Manschot (1985)
	$E_{\perp} = 4.6$	leg	Manschot (1985)
torsion	E = 0.42	dorsal forearm (<30 yr)	Agache et al. (1980)
	E = 0.85	dorsal forearm (>30 yr)	Agache et al. (1980)
	E = 1.12	ventral forearm	Escoffier et al. (1989)
suction	E = 0.13-0.26	various anatomical sites	Barel et al. (1995)
indentation	$E = 1.99 \cdot 10^{-3}$	male thigh	Bader and Bowker (1983)
	$E = 1.51 \cdot 10^{-3}$	male forearm	Bader and Bowker (1983)
	$E = 1.09 \cdot 10^{-3}$	female forearm	Bader and Bowker (1983)

1.3.3 Mechanical experiments on the skin *in vitro*

An advantage of *in vitro* testing on the skin is the possibility to separate the skin layers. However, it is not clear what the effect is of this disruption on the mechanical properties of the individual skin layers. Numerous *in vitro* experiments have been performed on the skin in the past. Unfortunately, most of them are poorly documented and often it is not clear whether merely dermis or the total skin is tested.

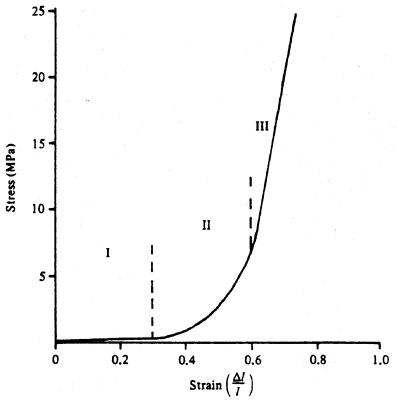

Figure 1.8: *Non-linear stress-strain diagram for the skin.*

A significant study is performed by Daly (1982). He described the relation between dermal structure and the non-linear stress-strain relationship that was found in tensile tests. The stress-strain curve for the skin can be divided in four stages (figure 1.8). In the first stage, the contribution of the undulated collagen fibres can be neglected and elastin is responsible for the skin stretching. In this stage, the stress-strain relation is approximately linear with a Young's modulus of approximately 5 kPa (Daly, 1982). In the second phase, a gradual straightening of an increasing fraction of the collagen fibres causes an increasing stiffness. In the third phase, all collagen fibres are stetched and the stress-strain relation becomes linear again. Beyond this phase, yielding and rupture of the fibres occur.

Oxlund et al. (1988) showed with an experiment on rat skin of which part of the elastin was removed, that the elastin fibres mainly affect the mechanical behaviour at small strain values. The elastin fibres are especially responsible for the recoiling mechanism when stress or deformation is released.

1.3.4 Mechanical experiments on stratum corneum

Stratum corneum properties are highly influenced by environmental properties such as temperature and relative humidity, both *in vivo* and *in vitro*.

Several groups investigated the effect of moisture on the tensile properties of *in vitro* stratum corneum (table 1.2). Park and Baddiel (1972) studied the effect of the relative humidity on the elastic modulus of pig's ear stratum corneum, which differs only slightly from human stratum corneum. *In vitro* tensile experiments were performed on prestretched

samples for 30-100% RH and 25°C. The total extension observed at fracture was 1%. Young's moduli of 1-4 GPa were found for 30% RH. For 75% and 100 % RH Young's moduli of 200 Mpa and 6 Mpa were found, respectively.

Papir et al. (1975) studied the effect of water and temperature on the tensile properties of newborn rat stratum corneum *in vitro*. Stress-strain measurements were performed for relative humidities varying from 26-100% RH at 25°C, and for temperature varying from 25-60°C at 32% RH.

Table 1.2: *In vitro tensile properties for stratum corneum at various environmental conditions.*

E [MPa]	$\epsilon_{\mathbf{fracture}}$	**conditions**	**source**	**reference**
2000	-	RH= 30%, 25°C	pig's ear	Park and Baddiel (1972)
6	-	RH=100%, 25°C		
8900	1.9	RH= 26%, 25°C	rat	Papir et al. (1975)
2400	7.7	RH= 68%, 25°C		
12	140	RH=100%, 25°C		
2600	5.0	RH= 32%, 37°C		
110	120	RH= 32%, 60°C		

Hendley and Payne (1982) developed a simple point indentation device to measure variations in measured force due to age, sex and site *in vivo*. The instrument consisted of a needle (11 μm at the tip) that was held perpendicular to the surface and moved rapidly 10 μm into the skin. They claim that the rapidity of the indentation ensures that predominantly stratum corneum properties are tested. Observed forces were typically in the order of 3.0 N, and hydration resulted in lower forces.

Rigal and Lévêque (1985) extended the torsional technique as described by Rigal et al. (1980) and Agache et al. (1980) to measure the effect of hydration on stratum corneum behaviour *in vivo*. The inner disc (18 mm) and the guard ring were glued to the skin, leaving an annular size for the skin of 1, 3 or 5 mm. The observed relative increase in immediate deformation U_e due to hydration, was larger for 1 mm annular size (80% increase) than for 3 mm annular size (15% increase). Therefore, they concluded that the contribution of the stratum corneum on the mechanical response of the entire skin increases with a decreasing gap size.

However, as with many *in vivo* experiments, it is difficult to interpret the influence of deeper skin layers on the overall response.

1.3.5 Numerical models to describe skin mechanics

It was already recognized at an early stage that a full description of the mechanical behaviour of the skin requires an anisotropic, non-linear, visco-elastic model. In 1973, Fung pointed out that the Young's modulus, E, is relatively meaningless unless the exact stress level is specified (Fung, 1973, 1981). He defined an anisotropical exponential strain

energy function, which could be fitted well to biaxial experimental results performed on rabbit skin (Lanir and Fung, 1974; Tong and Fung, 1976). However, the model could not predict experiments with slightly different boundary conditions.

Numerous other strain energy functions have been proposed to model the skin. Besides this continuum approach, which was used by for example Crisp (1972); Allaire et al. (1977) and Veronda and Westman (1970), also models were developed which take the structure of the skin into account. Lanir (1979) summarized some of these structural models and proposed a biaxial model with collagen and elastin fibres. Both fibres were defined elastic and the interaction with the ground substance was ignored. A good qualitative agreement was found with results from experiments on rabbit skin.

Barbanel (1979) developed a one-dimensional linear visco-elastic model, to account for the time-dependent behaviour of the model. Wijn (1980) developed a structural visco-elastic model, consisting of visco-elastic elastin fibres for small deformation of the skin. He used it to quantitatively relate the results of torsion measurements and uniaxial strain measurements in different directions.

Oomens et al. (1987) used a mixture approach to describe the nonlinear elastic and nonlinear time-dependent behaviour of the skin and subcutis. The model consisted of a porous solid (representing the fibre network embedded in the colloid-rich part of the ground substance) and a freely movable fluid (the colloid-poor part of the ground substance). The model is based on the hypothesis that skin behaves as a sponge-like material, consisting of a porous solid with a fluid in it. This mixture approach is especially valuable for tissues under compression.

In the last two decades, finite element models are used to simulate the mechanical behaviour of the skin. Larrabee et al. used the finite element technique to model wound closures and skin deformations (Larrabee and Sutton, 1986; Larrabee and Galt, 1986). They modelled the skin as an isotropic two-dimensional system connected to a rigid plane with linear springs, representing the subcutaneous attachment. A linear stress-strain relationship was used and time dependence and pretension were ignored.

To account for large deformations and large strains, Kirby et al. (1998) extended the model by Larrabee to a non-linear, isotropic finite element model. Retel et al. (2001) extended Larrabee's model to allow for compression which can occur during wound closure.

Bisschoff et al. (2000) used the eight-chain model by Arruda and Boyce (1993) as an elastic constitutive equation for their finite element model. They obtained data of three different experiments from literature to determine the unknowns in the constitutive equations. Although a lot of assumptions had to made to be able to use those data, they were quite successful in simulating the experiments.

Meijer et al. (1999) combined uniaxial extension experiments and a finite element model with Lanir's structural skin model (Lanir, 1983) as a constitutive equation to characterize the anisotropic non-linear behaviour of human skin *in vivo*.

1.4 Aim and objectives

The previous sections showed large variations in material parameters for the skin for the various experiments that were conducted. This is caused by the use of over simplified models to simulate the experiments, such as the use of linear models to describe the non-linear stress-strain relationship, and the fact that it is often not clear what part of the skin is examined and in which (environmental) conditions the experiments are performed. Furthermore, there is a paucity of studies in the literature which have examined the influence of the different layers on the mechanical response of the skin.
The aim of the present thesis is to gain a better understanding in the mechanical behaviour of the skin by characterizing the mechanical behaviour of four skin layers *in vivo*: the subcutaneous fat or hypodermis, the dermis, the living part of the epidermis and the stratum corneum. The work is based on the hypothesis that a combination of experiments of different length scales can be used to study the mechanical behaviour of those skin layers. Application of experiments with a small length scale enables examination of the mechanical behaviour of the top layers of the skin, whereas experiments at large length scale can be used to examine the mechanical behaviour of the deeper layers.

To achieve this aim, several objectives were defined. The *first objective was to develop several experimental set-ups which are able to apply mechanical loading to the skin and to visualize the resulting deformation of the different skin layers.* Suction was chosen to load the skin mechanically. An advantage of suction is that it loads the skin both perpendicular and parallel to the skin surface. Second, due to the axi-symmetric nature of the load, the anisotropy in the plane parallel to the the skin surface will play a minor role. Third, as the skin is glued to the suction device, the boundary conditions are clearly defined. Finally, suction is easy to combine with an imaging method as the region of interest is visible through the suction aperture.

To visualize hypodermal and dermal deformations, ultrasound was combined with a 6 mm diameter aperture suction experiment. Optical coherence tomography was employed to visualize epidermal and dermal deformations in 1, 2 and 6 mm diameter aperture suction experiments. Finally, deformations in stratum corneum and living epidermis were examined by confocal microscopy during a tensile experiment.

The *second objective was to quantify deformations that were applied to the skin.* Therefore, the OCT and the ultrasound images were processed to obtain displacements of the skin surface and the papillar/reticular dermis interface and the dermis/fat interface, respectively. Digital image correlation was applied to the images obtained with confocal microscopy to obtain displacement fields and strain fields.

The *third objective was to characterize the mechanical behaviour of the different skin layers.* To achieve this, the experiments were described with dedicated finite element models and a numerical-experimental method was used to identify the parameters of the material models. As the primary interest was the separation of the response of the different layers, only non-linear elastic material behaviour was studied and time-dependence, inhomogeneity and anisotropy parallel to the skin surface were neglected.

1.5 Outline

Chapter 2 describes a numerical-experimental method which is developed to evaluate the mechanical behaviour of the skin. The dermis and the hypodermis are visualized with high-resolution ultrasound and the skin is loaded with suction through an aperture of 6 mm diameter. The experiment is simulated with a finite element model consisting of one layer representing the dermis and the epidermis. The influence of superficial skin hydration and the influence of the size of the aperture diameter on the mechanical response of the skin is studied in chapter 3. The upper part of the dermis and the epidermis are visualized during the experiment with optical coherence tomography, while the dermal thickness is measured after the experiment with ultrasound. The finite element model that was described in chapter 2 is used to simulate the experiments and calculate the material properties for the various aperture diameters. In chapter 4, a finite element model is developed which consists of two layers, representing the reticular dermis and the combined papillar dermis and epidermis. With this model experiments with various aperture diameters can be simulated. Chapter 5 describes the third experimental set-up. Tension is applied to the skin while the epidermis and the uppermost part of the dermis are visualized with confocal microscopy. Finally, in chapter 6 a general discussion is given on the presented results and some recommendations are given for future work.

The contents of chapters 2 and 3 are written in journal format. Therefore, these chapters can be read independently. Unfortunately, this led to some recurrence and overlap between the chapters.

Chapter 2

A numerical-experimental method to characterize the non-linear mechanical behaviour of human skin using high resolution ultrasound

The contents of this chapter are based on Hendriks et al. (2003). **A numerical-experimental method to characterize the non-linear mechanical behaviour of human skin.** *Skin Research and Technology 9: 274-283, 2003.*

2.1 Introduction

Knowledge about the mechanical behaviour of the skin *in vivo* is of importance for cosmetic and clinical applications. It can help to quantify the effectiveness of cosmetic products and to evaluate both skin diseases and pressure sores. Mechanical behaviour of the human skin is complex. The skin shows a non-linear stress-strain relationship, behaves time-dependent, incompressible, anisotropic and inhomogeneous, and is subjected to a prestress. The complex structure of the skin leads to complex mechanical behaviour.

Several studies have been performed to determine the mechanical properties of the skin *in vivo*. Overviews were given by Piérard et al. (1995) and Rodrigues and the EEMCO group (2001). The most frequently used techniques are tensile, indentation, torsion and suction experiments. Diridollou et al. (1998) already mentioned that the data obtained are mainly descriptive. Occasionally, a model exhibiting (linear) Hookean material behaviour is applied to obtain a Young's modulus E. However, the value of the Young's modulus obtained is affected by various factors such as the amount of deformation (due to the non-linear stress-strain behaviour), hydration, skin thickness and the length scale of the experiment (for example, indenter diameter or aperture size). It also varies considerably for different experimental techniques. Bader and Bowker (1983) obtained $E = 1.1 - 2.0$ kPa for indentation measurements using a 20 mm indenter. Agache et al. (1980) obtained $E = 0.42 - 0.85$ MPa from torsion experiments using a disc of 25 mm diameter and guard ring of 35 mm diameter. Manschot (1985) obtained $E = 4.6 - 20$ MPa for tensile tests using load pads of 10×10 mm^2 with a distance of 5 mm. Suction tests performed by Barel et al. (1995) using the Cutometer with an aperture size of 2 mm resulted in $E = 0.13 - 0.26$ MPa. Suction experiments performed by Diridollou et al. (2000) applying 10 kPa (100 mbar) suction and an aperture size of 6 mm resulted in $E = 153$ kPa. In the above mentioned papers different constitutive models were used. What all these papers have in common, is the use of simplified geometric models and boundary conditions, because all authors wanted to use closed form solutions for the mechanical analysis. This might explain the different outcomes for different types of experiments. In fact, this means that the models only successfully describe the mechanical behaviour of the skin for the particular loading case used in the experiment.

One way of circumventing this problem, is to use a more accurate modelling of the geometry and boundary conditions in the experiment. This implies that closed form solutions no longer exist and that a numerical analysis of the experiment can no longer be avoided. Our aim is to develop a method to characterize the non-linear mechanical skin behaviour using a numerical-experimental technique. In the present chapter, this method is used to develop a non-linear finite element model that is able to predict the skin behaviour during suction at varying pressures. If the method proves useful, it can be used in the future to develop a non-linear finite element model that is able to predict the mechanical behaviour of the skin during different loading conditions such as suction at various aperture sizes or torsion, indentation and tensile experiments.

Suction was chosen, because it loads the skin both parallel and perpendicular to the skin surface. A second advantage of suction is that the boundary conditions are clearly

defined. Furthermore, this method is easy to combine with an imaging method.

The suction experiment developed is similar to that described by Diridollou et al. (1998). Subsurface deformation of the skin is visualized using ultrasound. A numerical-experimental method, combining the results of a finite element model and the experiment, is used to identify the material parameters.

2.2 Materials and methods

The mechanical behaviour of the skin will be characterized using a numerical-experimental method, based on three major steps:

- Measurement of deformation of the skin composite (defined here as the combined epidermis and the dermis) in response to applied suction.
- Finite element modelling of the suction experiment.
- An iterative scheme to compare numerical and experimental results. In each iterative step, parameters are updated until convergence is reached.

This method is frequently used to model mechanical behaviour of materials. See for example Oomens et al. (1993), Sol and Oomens (1997) and Meijer et al. (1999).

2.2.1 Experimental set-up

Suction is based on applying partial vacuum (relative underpressure) to the skin. *In vivo* suction experiments were applied to the volar forearm skin. This site was chosen since it is easily accessible and relatively flat. Furthermore, the epidermis at this site is thin. Therefore, at this moment, the contribution of the epidermis to the mechanical response of the entire skin was neglected.

A frequency of 20 MHz ultrasound was employed during the suction experiment to measure the deformation of the skin. A commercially available ultrasound system was used: DUB 20 (Taberna Pro Medicum, Germany). This system generates real-time two-dimensional (2D) images (B-scans) with a lateral dimension of 12.8 mm. The step size of the scanning system is 100 μm. The axial dimension of the images depends on the penetration depth. The obtained axial resolution is defined by the ratio of the sound velocity and the frequency and is 79 μm.

A suction device that can be coupled to the ultrasound system was built to load the skin (figures 2.1 and 2.2). It consists of a pressure chamber which was attached to the skin with double-sided adhesive tape. The diameter of the aperture plate touching the skin is 24 mm. The maximum outer diameter of the chamber is 50 mm and the maximum height is 27 mm. The detachable unit of the chamber can be detached, so different aperture sizes can be used. In this study an aperture size of 6 mm was used.

Distilled water was added to the pressure chamber through the water inlet to serve as coupling liquid for the ultrasound. Addition of water hydrates the stratum corneum and

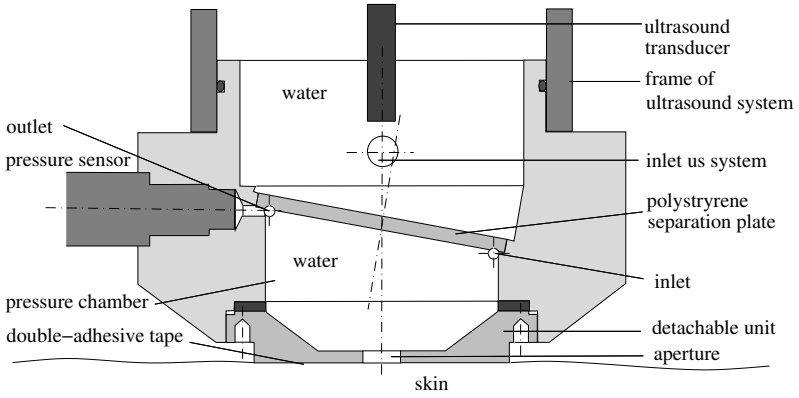

Figure 2.1: *Schematic representation of the suction device attached to the ultrasound system. The device consists of a pressure chamber that can be closed to load the skin through the aperture and of a water filled part which connects the pressure chamber to the ultrasound system. The detachable unit enables use of various aperture sizes.*

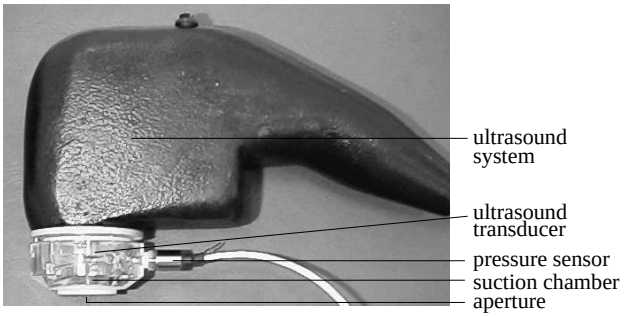

Figure 2.2: *Picture of the suction device attached to the ultrasound system.*

causes a decrease in Young's modulus of the stratum corneum (Park and Baddiel, 1972). This decreases its contribution to the mechanical behaviour of the total skin.

To prevent air bubbles sticking to the walls of the chamber, a small amount of detergent was added to the distilled water (one drop per liter). Air bubbles were removed through the water outlet. The polystyrene plate that separates the pressure chamber and the ultrasound system is positioned under an angle slightly less than 90 degrees with respect to the ultrasound beam. This was done to simplify removal of air bubbles and to reduce sound reflection of the polystyrene separation plate into the transducer.

When the pressure chamber was filled with water, the outlet was closed. Water was withdrawn from the pressure chamber using a spindle driven syringe. The resulting suction pressure lifted the skin through the aperture into the pressure chamber. The applied pressure was measured by a Kulite pressure sensor, which is located behind the water outlet (Kulite, XTC-190M-350 mbar VG, -350 to +350 mbar for -0.1 to +0.1 V). The pressure was set to zero when the skin surface is flat (zero suction state). Water was withdrawn in 4 steps such that the skin is uplifted approximately 0.6, 0.9, 1.2 and 1.5 mm.

Immediately after each step, the pressure was measured and simultaneously a 2D image of the deformed skin was made.

Measurements were performed on the left forearm of 10 subjects (male and female, aged 19 to 24 years old). All subjects were healthy and of Caucasian skin type. All volunteers gave informed consent. Measurements were carried out in climate controlled test rooms at 22°C and 50% relative humidity. The suction measurements were part of a larger investigation on skin properties and subjects were in the climate controlled test rooms at least one hour prior to the suction measurement. Subjects were seated upright and rested their arm on a table. To ensure a relaxed position, the arm was positioned on a cushion covered with towels (figure 2.3). The force of the suction chamber on the arm was minimized by mounting the ultrasound system on a cantilever with a counterweight (not visible in the picture).

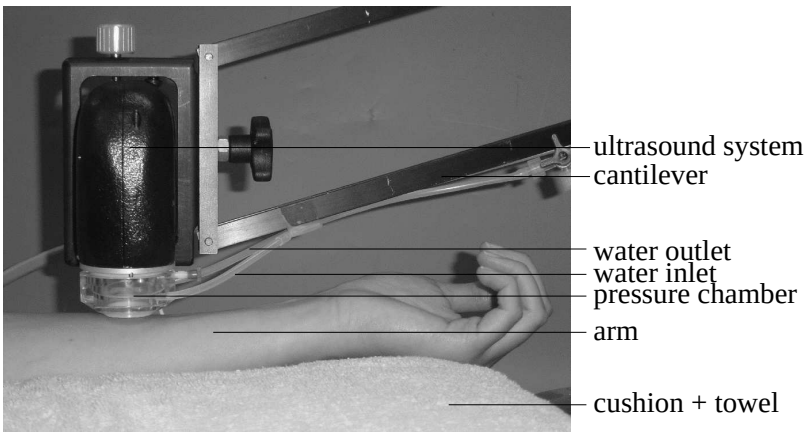

Figure 2.3: *Picture of the suction device coupled to the ultrasound system and attached to the volar forearm skin. The ultrasound system in mounted on a cantilever. The subject is seated upright with his arm in a relaxed state resting on a cushion.*

The thickness of the fat layer and the skin composite were calculated with the software that accompanies the ultrasound system using a sound velocity of v=1440 m/s and v=1580 m/s, respectively (Serup et al., 1995). The location of the suction device was used as a reference to calculate the displacement of the skin surface, using a sound velocity of v=1500 m/s for water.

2.2.2 Finite element model

The skin composite is not thin enough compared to the aperture size of the suction device to model it as a membrane. Therefore, the suction experiment was simulated using the finite element method (Hughes, 1987). One of the possible reasons for the difference in results of different types of experiments, as indicated in the introduction of this chapter, can be explained by the use of oversimplified models for geometry and boundary conditions.

A circle of skin with radius $r = 24$ mm (chosen such that at that point the effect of the surrounding tissue on the total response was negligible) was modelled using an

axisymmetric model. The thickness of the skin composite was obtained from the ultrasound images. For each subject a separate FE mesh (figure 2.4) was made, based on the dimensions obtained from the ultrasound images. All displacements of the skin surface glued to the pressure chamber were restrained. Displacements at the dermis-fat interface and the outside boundary were left free and displacements at the symmetric axis were restrained in the direction parallel to the skin surface to satisfy symmetry conditions. Pressure in the suction device was prescribed according to the pressure measured in the experiments.

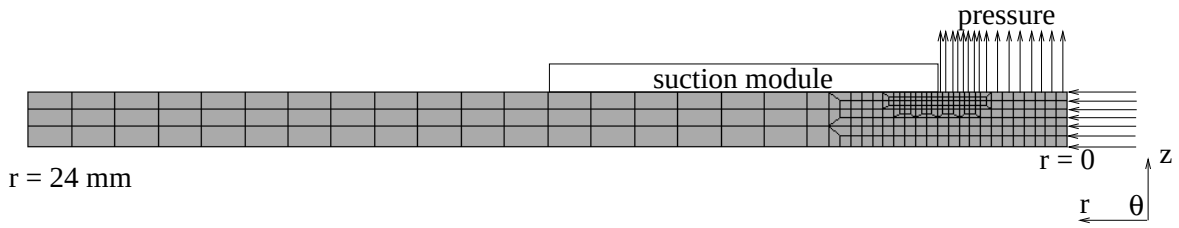

Figure 2.4: *Finite element mesh and boundary conditions of the suction experiment for subject 13.*

Since we are primarily interested in measuring the mechanical behaviour of the different skin layers, time-dependence was neglected. For quasi-static loading, the compressibility of the skin is negligible, and therefore the skin can be modelled as incompressible. Furthermore, the skin was assumed to be isotropic in the plane parallel to the skin surface.

For an elastic isotropic and incompressible solid the stress-strain relation can be given by

$$\sigma = -p\mathbf{I} + \alpha_1\mathbf{B} + \alpha_2\mathbf{B}^2 \tag{2.1}$$

where σ is the Cauchy stress tensor, p is an arbitrary hydrostatic pressure, $\mathbf{I}$ is the unity tensor, α_1 and α_2 are scalar functions and $\mathbf{B}$ is the left Cauchy-Green tensor defined by

$$\mathbf{B} = \mathbf{F} \cdot \mathbf{F}^c. \tag{2.2}$$

The deformation gradient tensor $\mathbf{F}$ is given by

$$\mathbf{F} = \frac{\partial \mathbf{x}}{\partial \mathbf{X}} \ , \tag{2.3}$$

where $\mathbf{x}$ is the vector describing the position of a material particle in a deformed state and $\mathbf{X}$ is the vector describing the position of a material particle in the initial state of zero strain and zero stress. For incompressible, elastic and isotropic materials the stress can be expressed in terms of a strain energy function $W = W(I_1, I_2)$, where I_1 and I_2 are the strain invariants of $\mathbf{B}$,

$$I_1 = tr\ \mathbf{B} \tag{2.4}$$

$$I_2 = \frac{1}{2}((tr\ \mathbf{B})^2 - tr\ \mathbf{B}^2). \tag{2.5}$$

The scalar functions α_1 and α_2 are defined as

$$\alpha_1 = 2(\frac{\partial W}{\partial \mathbf{I}_1} + \mathbf{I}_1 \frac{\partial W}{\partial \mathbf{I}_2}) \tag{2.6}$$

$$\alpha_2 = -2(\frac{\partial W}{\partial \mathbf{I}_2}). \tag{2.7}$$

It was chosen to use the strain energy function by James, Green and Simpson (MSC Software Corporation, 2000) to model the mechanical behaviour of the skin

$$W = C_{10}(\mathbf{I}_1 - 3) + C_{01}(\mathbf{I}_2 - 3) + C_{11}(\mathbf{I}_1 - 3)(\mathbf{I}_2 - 3) + C_{20}(\mathbf{I}_1 - 3)^2 + C_{30}(\mathbf{I}_1 - 3)^3. \tag{2.8}$$

This relation was previously used to model the non-linear behaviour of the skin (Douven, 1999). It was found that the use of merely the constants C_{10} and C_{11} is sufficient to model this behaviour. The strain energy density function is then reduced to

$$W = C_{10}(\mathbf{I}_1 - 3) + C_{11}(\mathbf{I}_1 - 3)(\mathbf{I}_2 - 3). \tag{2.9}$$

Substitution of 2.9 in 2.6 and 2.7 yields

$$\alpha_1 = 2[C_{10} + C_{11}(\mathbf{I}_1^2 - 3\mathbf{I}_1 + \mathbf{I}_2 - 3)] \tag{2.10}$$

$$\alpha_2 = -2C_{11}(\mathbf{I}_1 - 3). \tag{2.11}$$

Equation 2.1 combined with equations 2.10 and 2.11 describe the relation between the Cauchy stress tensor σ and the left Cauchy-Green strain tensor $\mathbf{B}$ and its invariants. This relation will be used to describe the different skin layers. The values of C_{10} and C_{11} are the material parameters that need to be identified.

The finite element (FE) package MSC.MARC (MSC Software Corporation, 2001) was used to solve the balance of momentum equations using the above given constitutive model.

To compare our results with that from the literature, the contribution of the second part of the equation can be neglected for small strains and then C_{10} can be converted into a Young's modulus using $E = 6\ C_{10}$.

In the appendix at the end of this chapter a pilot experiment is described which was performed to estimate the material properties of the fat and the skin composite. Estimations were performed with a two layer model with fat and skin composite as separate layers. It appeared that the stiffness of the fat layer is very small compared to the skin composite and hardly influences the result of the numerical analysis. Therefore the parameter estimation procedure was relatively insensitive to changes in the material properties of the fat and that made it difficult to estimate the fat properties by means of this experimental set-up. Furthermore, due to the large difference in stiffness of both layers, in some cases numerical convergence could not be obtained for large deformations. Therefore, it was chosen to model only the skin composite and to characterize the non-linear mechanical behaviour of this layer.

2.2.3 Parameter identification

The third part of the numerical-experimental method is the iterative procedure that is used to adjust the parameters of the material model. This procedure is performed in MATLAB (The MathWorks Inc, Magrab et al. (2000)). It adjusts the material parameters in the input file of the FE model, runs the FE simulation, extracts the relevant results from the simulation (skin surface displacements at various pressure levels), and compares the results from the simulation with the experimental results. The results are put in an objective function that needs to be minimized. The objective function is defined as:

$$O = \ln \sum_{i}^{n} \left(\frac{x_{i,num} - x_{i,exp}}{x_{i,exp}}\right)^2 \tag{2.12}$$

Where $x_{i,exp}$ is the experimentally obtained axial displacement of the skin surface in the centre of the aperture at observation i and $x_{i,num}$ is the numerically obtained displacement of the skin surface in the centre of the aperture at observation i. The number of observations is n. A standard constrained non-linear optimization function in MATLAB is used to minimize this objective function for the material parameters C_{10} and C_{11} (Coleman et al., 1999). The displacements of the skin surface in the centre of the aperture, x_i, at various pressures p_i, are the results that are used to identify the material parameters. The applied pressures p_i are used as input to the finite element model.

2.3 Results

2.3.1 Experiment

The upper part of figure 2.5 shows an ultrasound image of the volar forearm skin of a 21 year old male (subject 7) at zero suction state.

The figure reveals the entrance echo caused by the water-stratum corneum interface, the skin composite, the subcutaneous fat and the underlying muscle. The epidermis cannot be distinguished from the dermis due to the system's resolution of 79 μm.

The skin surface and the bottom of the aperture plate are not at the same level in the ultrasound image. This is caused by the different sound velocities of the aperture plate and the water. The software uses only one sound velocity to convert all detected time signals into depth information. The figure also shows that no clear signal is reflected to the transducer from the skin behind the aperture plate.

In the centre of the aperture, a thickness of 1.48 mm was estimated for the skin composite. The thickness of the subcutaneous fat was 0.81 mm. Application of 2.6 kPa (26 mbar) suction pressure (lower part of figure 2.5) caused an increase in the thickness of the fat layer with 0.60 mm to 1.41 mm. The thickness of the skin composite remained unchanged. The skin surface moved upward 0.55 mm. The fat-muscle interface did not move.

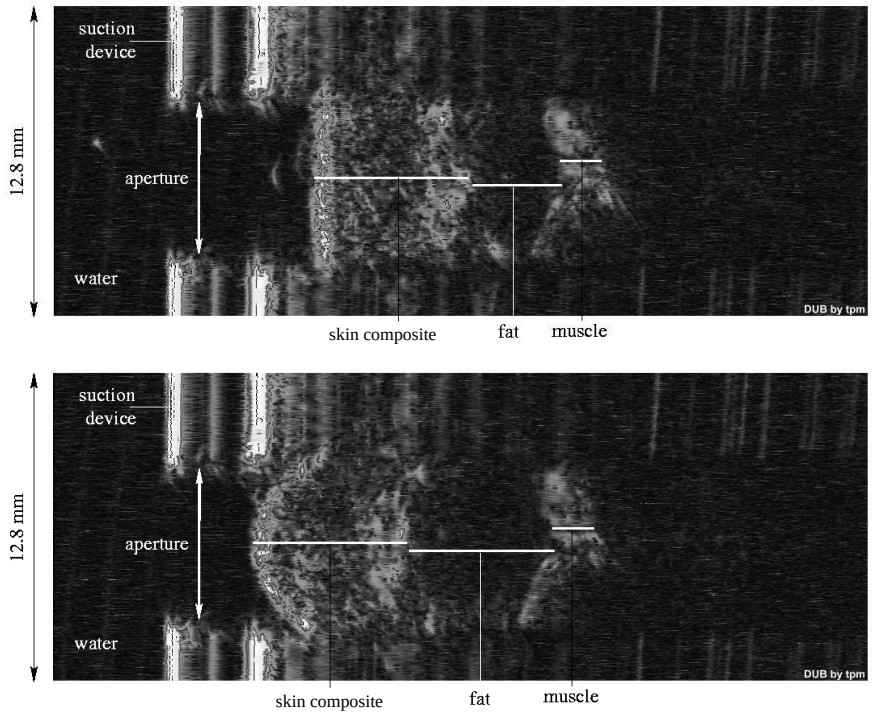

Figure 2.5: *Ultrasound image of forearm skin and fat at atmospheric pressure (upper) and at 2.6 kPa suction (lower). From left to right: water (black), entrance echo (bright), skin composite (grey and white), subcutaneous fat (black) and muscle (grey and white).*

Increasing the suction pressure led to an increasing uplift of the skin surface, an increasing fat thickness and a decreasing thickness of the skin composite. At 19.4 kPa suction pressure the skin surface uplift was 1.61 mm, the thickness of the fat layer was increased with 1.59 mm to 2.40 mm and the thickness of the skin composite was slightly decreased with 0.1 mm. The fat-muscle interface moved up 0.12 mm.

The suction also led to decreased signal intensity compared to the zero stress state, especially in the regions outside the centre of the aperture. This was caused by the orientation of dermal fibres. Because of the curvature of the skin, the dermal fibres are no longer oriented perpendicularly to the ultrasonic beam, resulting in a smaller amount of ultrasonic wave energy reflected to the transducer.

It was observed that for 6 of the 10 subjects the muscle could not be detected. Therefore it was not possible to measure the thickness of the fat layer for all subjects.

In figure 2.6 the measured pressure is plotted versus the skin surface displacement for 10 subjects. This figure illustrates that the pressure-displacement curve is non-linear and that the measured pressure at a certain displacement can vary up to a factor of 4 for the different subjects. Sex, age and thickness of the skin composite are given in table 2.1 for each subject. The average thickness of the skin composite found was 1.35 ± 0.10 mm.

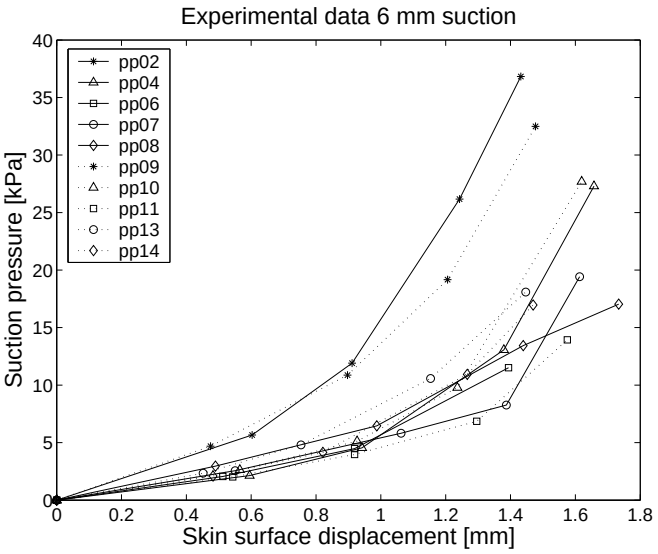

Figure 2.6: *Experimentally obtained pressure-displacement curves for 10 subjects using an aperture size of 6 mm.*

Table 2.1: *Sex, age, thickness of skin composite, C_{10}, C_{11} and value of the objective function O for each subject.*

Subject	sex	age	t_{skin} [mm]	C_{10} [kPa]	C_{11} [kPa]	O
2	m	24	1.34	10.8	231	-7.6
4	f	24	1.21	6.0	99	-7.0
6	f	19	1.23	8.9	52	-7.1
7	m	21	1.48	8.9	42	-4.9
8	m	23	1.44	10.8	23	-5.4
9	m	23	1.36	17.8	112	-7.5
10	f	22	1.51	4.8	65	-4.4
11	f	23	1.33	7.1	34	-5.6
13	f	21	1.28	10.5	89	-8.7
14	f	22	1.27	8.3	77	-6.1

2.3.2 Numerical model and parameter identification

Three typical pressure-displacement curves are presented for the experimental data and the prediction of the finite element model for three different subjects (figure 2.7). The lines represent the numerical results and the symbols represent the experimental data.

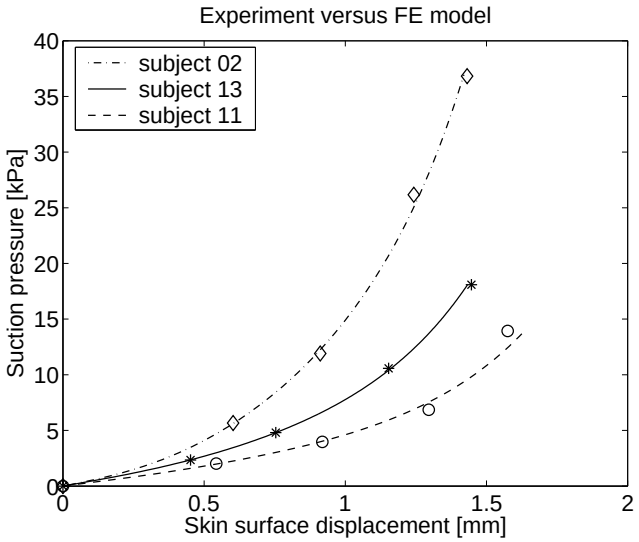

Subject	C_{10} [kPa]	C_{11} [kPa]
2	10.8	231
13	10.5	89
11	7.1	34

Figure 2.7: *Experimentally obtained and simulated pressure-displacement curves for 3 subjects. The lines represent the numerical results: dash-dotted line for subject 2, solid line for subject 13 and dashed line for subject 11. The symbols represent the experimental data: diamond for subject 2, star for subject 13 and circle for subject 11.*

This figure shows that the used finite element model exhibiting extended Mooney behaviour is able to describe the experimentally observed response. Table 2.1 also shows the estimated material parameters and the value of the minimized objective function O for this set of material parameters for all subjects. For the entire test group average values of $C_{10} = 9.4 \pm 3.6$ kPa and $C_{11} = 82 \pm 60$ kPa were found. The displacement field (in mm) in the skin for subject 13 predicted with the finite element model using the above mentioned material parameters is shown in figure 2.8.

The stability of the estimation procedure was evaluated by varying the initial estimates of the material parameters. This was done for all measurements. Variations up to a factor of 5 did not affect the value of the final estimation for the material parameters. Also the influence of the number of experimental observations on the estimated value of the material parameters was studied. It was found that reducing the number of observations caused large variations in the estimated values. Therefore, it is important to obtain enough experimental data to obtain reliable values for the material parameters.

The reproducibility of the method was studied by evaluating the influence of measurement errors such as deviations in thickness of the skin composite, measured pressure or displacements on the estimated material parameters.

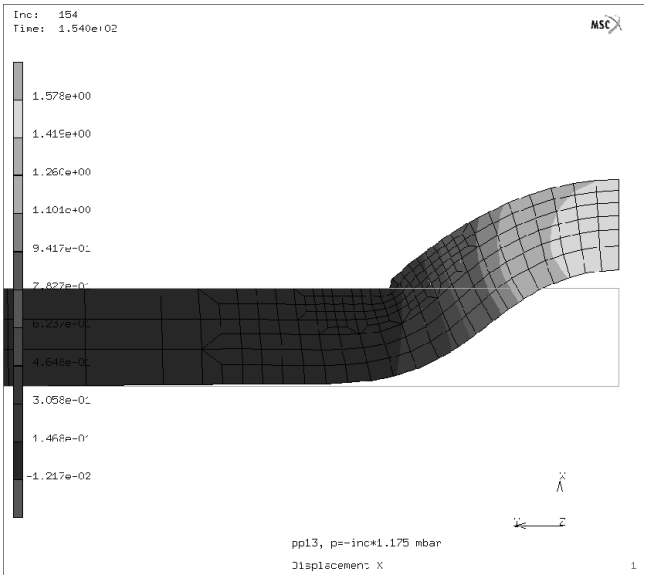

Figure 2.8: *Detail of result of finite element simulation showing displacements at 18 kPa suction for subject 13.*

The influence of the thickness of the skin composite was evaluated for subject 11. Increasing the thickness of the skin composite in the FE model with 2.3% (0.03 mm) caused a decrease of C_{10} and C_{11} with 4.3% and 1.4% respectively.

The influence of the measured displacements on the estimated material parameters was also evaluated for subject 11. Increasing all observed displacements of the skin surface with 5% (maximum increase is 0.08 mm) caused a decrease of C_{10} and C_{11} with 2.2% and 21% respectively. Increasing the observed displacements with 10% caused a decrease of C_{10} and C_{11} with 4.1% and 38% respectively. Decreasing the observed displacements with 5% caused a increase of C_{10} and C_{11} with 2.4% and 26% respectively. Those results show that especially C_{11} is largely affected by measurement errors in the skin surface displacement.

The necessity for the non-linear term in the constitutive equation that describes the material behaviour, C_{11}, is evaluated for subject 11 as well. Figure 2.9 shows the pressure-diplacement curves for the experimental data (stars) and for FE simulations with C_{10} and C_{11} as estimated with the numerical-experimental method (C_{10} = 7.1 kPa and C_{11} = 34 kPa, solid line); C_{10} = 7.1 kPa and C_{11} = 0 (dashed line) and C_{10} = 14.2 kPa and C_{11} = 0 (dotted line). The figure shows that Neo-Hookean material behaviour, W = C_{10} (I - 3), is not suitable to describe the non-linear behaviour of the skin composite.

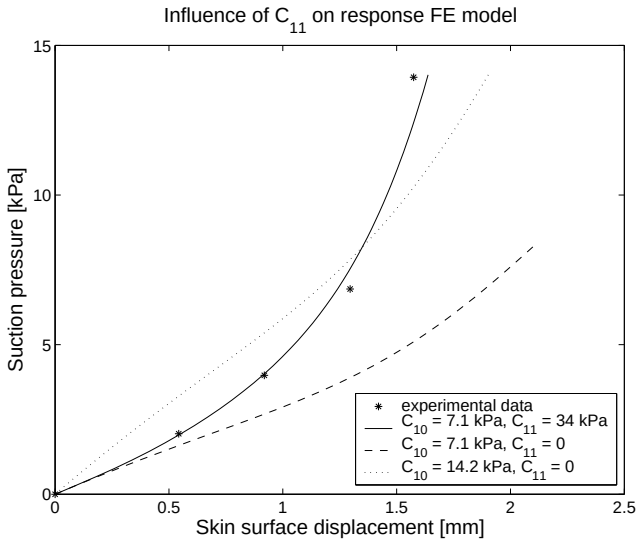

Figure 2.9: *Pressure-displacement curves for the experimental data (stars) and for FE simulations of subject 11 with C_{10} and C_{11} as estimated with the numerical-experimental method (C_{10} = 7.1 kPa and C_{11} = 34 kPa, solid line); C_{10} = 7.1 kPa and C_{11} = 0 (dashed line) and C_{10} = 14.2 kPa and C_{11} = 0 (dotted line).*

2.4 Discussion

The described experimental set-up enabled visualizing deformation of the skin composite, subcutaneous fat and in some cases the underlying muscle. Most deformation caused by suction was found in the fat layer, which agrees with observations by Diridollou et al. (1998).

Using a FE model of the skin composite and fat layer, a first rough estimate was found for the stiffness of the fat *in vivo* assuming Neo-Hookean material behaviour (C_{10} = 0.02 kPa). It was shown that the contribution of the fat layer to the mechanical response of the skin is negligible in suction experiments using an aperture size of 6 mm.

The employed numerical-experimental method was suitable to characterize the non-linear mechanical behaviour of the dermis *in vivo*. The resulting FE model using extended Mooney material behaviour was able to describe the experimentally obtained pressure-displacement curves for both small and large deformations. However, large variations were found for the skin response among the subjects, resulting in large variations for the material parameters. The advantage of this FE model over an analytical model such as described by Diridollou et al. (1998), is that the FE model is suitable to describe larger pressures and deformations. Moreover, the FE model can be used to describe suction experiments at smaller aperture sizes. In such an experiment, assuming the skin to be a (thick) membrane, is not allowed. Furthermore, the FE model exhibiting extended Mooney behaviour was able to describe the non-linear pressure-displacement curve of the skin composite without taking a prestress into account.

As non-linear material behaviour is modelled, the obtained material parameters (C_{10} = 9.4 kPa and C_{11} = 82 kPa) cannot be directly compared with results from the literature. Only by assuming small strains, C_{10} can be converted into a Young's modulus using the relation E = 6 C_{10}. This results in E = 56 kPa which is in the same order of magnitude as values found by Diridollou et al. (2000) (129 kPa) and Barel et al. (1995) (130-260 kPa). The slightly lower values resulting from this study can be explained by the contribution of C_{11}, as was shown in figure 2.9.
Evaluation of the method showed that the number of observations is important for the reproducibility of the calculated material parameters. To increase the number of observations, the set-up could be extended with a computer controlled pump to obtain a more continuous pressure-displacement curve.
The evaluation also showed that deviations of the thickness of the skin composite and measured displacements in the order of the system's resolution of 79 mm (approximately 5% deviation in thickness of the skin composite and measured displacements) may lead to large variations in the estimated material parameters. This problem can be solved by using a system with a better resolution and still enough penetration depth to visualize the entire skin composite, such as a higher frequency ultrasound system.
The experimentally obtained change in thickness of the skin composite is not used to test the performance of the constitutive model as the change of this thickness is in the order of the resolution of the system. With the numerical-experimental technique, enabling accurate modelling of the geometry and boundary conditions, it should be possible to compare the results from different kind of tests like suction, indentation and uni-axial test. These different test should provide the same material properties if an appropriate constitutive model is used. In the first experiments planned for this purpose different aperture sizes are used.

2.5 Appendix: Pilot experiment with two layer model

At first the model comprised of two layers: skin composite and fat. Both were assumed to be homogeneous. For each subject a FE mesh was made based on the thickness of the these layers obtained from the ultrasound images. The muscle-fat interface was forced to remain flat. Previous simulations showed that fixation in the plane parallel to the surface did not affect the total result.

To gain an initial guess for the stiffness of both layers, the skin was loaded with a small pressure to obtain small displacements and Neo-Hookean material behaviour was assumed ($C_{11,skin\ composite} = C_{11,fat} = 0$). $C_{10,skin\ composite}$ and $C_{10,fat}$ were estimated by comparing the computed displacement of the skin surface and the dermal-fat interface with experimental data. This experiment was performed on a 31 years old male, using an aperture size of 8 mm. Application of 3.7 kPa suction resulted in an increase of fat thickness from 1.15 to 1.58 mm. The thickness of the skin composite remained unchanged at 1.21 mm. The skin surface and the fat-muscle-interface were lifted 0.65 and 0.22 mm respectively. This resulted in $C_{10,skin\ composite}$ = 50 kPa and $C_{10,fat}$ = 0.02 kPa.

However, when larger deformations were applied to this model to identify C_{10} and C_{11} for both layers using parameter identification, a few problems were encountered. First of all, for larger deformations (skin uplift of 0.88 mm, corresponding to a maximum of 130% equivalent total strain in the fat layer), numerical convergence could not be obtained due to a combination of incompressibility and the large difference in stiffness of both layers. Secondly, the displacement of the skin surface was relatively insensitive to variations of C_{10}, fat, as long as its value stayed below a certain value (0.02 kPa). This may be caused by the combination of the aperture size of the experiment and the large difference in stiffness of both layers. Finally, only for subjects where the muscle can be identified with ultrasound, the thickness of the fat layer and its mechanical behaviour can be obtained.

For those reasons, the two-layer model was found to be inappropriate to characterize the mechanical properties of both skin composite and fat using the described experimental set-up.

The influence of the fat layer on the total response of the model was studied by comparing the pressure-displacement curves of the two-layer model (skin composite and fat) and a one-layer model (skin composite only). Removal of the fat layer from the FE model leads to a small increase (3%) in the displacement of the skin surface at 3.7 kPa suction (figure 2.10). This means that the fat layer hardly influences the response of the skin surface to the applied suction.

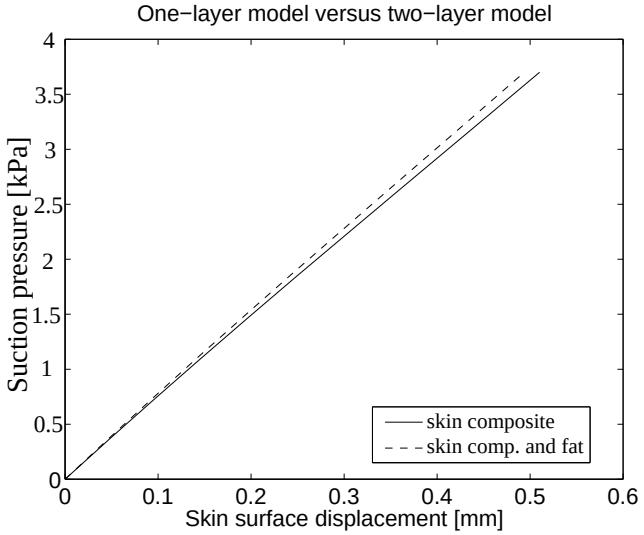

Figure 2.10: *Pressure-displacement curves for the skin surface predicted by the one-layer model (dermis) and the two-layer model (dermis and fat), assuming Neo-Hookean material behaviour.*

Chapter 3

Influence of hydration and experimental length scale on the mechanical response of human skin *in vivo*, using optical coherence tomography

The contents of this chapter are based on Hendriks et al. (2004a). **Influence of hydration and experimental length scale on the mechanical response of human skin *in vivo*, using optical coherence tomography.** *Skin Research and Technology, 10: 231-241, 2004.*

3.1 Introduction

The mechanical properties of skin have been studied for a long time. It was already recognized at an early stage that a full description of the mechanical behaviour of the skin requires an anisotropic, non-linear, visco-elastic model. A review of the models used so far was given in section 2.2.2.

Much research has focused on the mechanical behaviour of the skin, as reviewed in various publications by Marks (1991), Rodrigues and the EEMCO group (2001) and Diridollou et al. (2000). Common features of the studies is their assumption that the behaviour of the skin is dominated by the collagen-rich dermis. By contrast, the contribution of the epidermis, with its distinctive structural composition, is largely ignored. Indeed there is a paucity of studies in the literature which have examined the influence of the epidermis on the mechanical behaviour of the skin *in vivo*. Of the few, Rigal and Lévêque (1985) performed torsion tests with various annular sizes between the rotating disc and the guard ring on both normal and hydrated skin. They measured a larger increase in deformation due to hydration for decreasing annular size, indicating an increasing contribution of the uppermost skin layers to the mechanical response.

The mechanical behaviour of the epidermis is an important consideration in a number of cosmetic and clinical applications. In particular the barrier function of skin, which prevents excess evaporative fluid loss and protects the body from penetration of undesirable substances, is primarily fulfilled by the epidermis. In addition, it is the epidermis that interfaces with cosmetic products like creams or personal care devices such as shavers. Further clinical problems such as the development of pressure ulcers is a direct result of the breakdown at the interface between the skin and its external environment.

It is well established that the mechanical behaviour of the epidermis, which primarily consists of living cells, and its top layer, the stratum corneum, are strongly influenced by environmental conditions such as temperature and humidity. In an *in vivo* situation, the epidermis is also hydrated by the underlying dermis, motivating the need for an experimental system to measure the properties of the epidermis of the human skin in a non-invasive manner.

This chapter is aimed at developing such a non-invasive *in vivo* technique for determination of the mechanical properties of the epidermis. The methods for this are suction experiments, combined with ultrasound to visualize the skin composite and optical coherence tomography (OCT) to visualize the epidermis. The work was based on the hypothesis that measurements using aperture sizes with different diameters represent the mechanical behaviour of different skin layers. To put it differently, a large diameter of the suction aperture reflects the behaviour of mainly dermis, whereas a very small diameter reflects the behaviour of the top layers of the skin. This is in agreement with reports by Barel et al. (1995), Piérard et al. (1995), Agache et al. (1980) and Elsner et al. (1990). Barel et al. (1995) and Piérard et al. (1995) performed suction measurements with various aperture diameters on the skin. Both studies suggested that with large aperture diameters the response is largely determined by the behaviour of the dermis and underlying tissues,

whereas the response of small aperture suction experiments is dominated by epidermal behaviour. Agache et al. (1980) performed torsion measurements with various annular sizes and reported a similar finding.
Although in each of these studies the influence of the top layers is measured, the mechanical behaviour of these layers is not fully characterized.
If the above mentioned hypothesis is valid, different aperture sizes will lead to different mechanical properties in a parameter estimation procedure with a single layer finite element model.

Ultrasound needs water as a coupling liquid. This means that when this technique is used the skin is hydrated. As OCT needs no specific coupling liquid, it can be used to study the influence of water on the mechanical properties of the skin, by comparing suction measurements on both hydrated and non-hydrated skin.
It is hypothesized that the amount of water in the stratum corneum influences its mechanical response. This is based on earlier work showing less stiff material behaviour for *in vitro* (Wildnauer et al., 1971; Park and Baddiel, 1972) and *in vivo* (Rigal and Lévêque, 1985) hydrated stratum corneum. Combined with the first hypothesis (small aperture suction measures mechanical response of more superficial layers) this means that the effect of hydration on the mechanical response is expected to increase with decreasing aperture diameter, as was also found by Rigal and Lévêque (1985).

3.2 Materials and methods

Suction measurements in combination with OCT were performed on hydrated and untreated (dry) skin, using aperture diameters of 1, 2 and 6 mm. Skin elevation and thickness of the epidermis were obtained from the OCT images using MATLAB (The Mathworks Inc.). To determine thickness of the skin composite, which was needed for the finite element models, ultrasound measurements were performed on all measurement sites. Reproducibility between measurements using ultrasound or OCT as imaging method was evaluated by comparing results of both measurements using 6 mm aperture diameter.

3.2.1 Experimental set-up: optical coherence tomography

OCT is an interferometric technique using a low coherent light source. It is based on the principle of the Michelson interferometer. Low coherent light is coupled into a single-mode fibreoptic interferometer and divided into a reference arm and a sample arm. The reference signal is reflected from a scanning mirror system, which determines the scan position. The light in the sample arm is focused on the tissue, backscattered and recombined with the reflected light from the reference arm. Interference only occurs if the path length between the arms is matched to within the coherence length of the light source. Huang et al. (1991) and Schmitt et al. (1995) have provided an extensive description of OCT. It has been extensively used to study the human skin (Welzel et al., 1998; Gladkova et al., 2000;

Neerken et al., 2003). Our custom made OCT system is a fibre-optic based interferometer (Lenderink et al., 2002) with a central wavelength of 1310 nm and a spectral width of 50 nm. The axial resolution of the system is 14 μm and the penetration depth into the skin is approximately 1 mm. The OCT system acquires slices perpendicular to the skin of 2 $\times$ 2 mm^2 (lateral $\times$ axial dimension) in 1 second. One measurement consisted of 10 slices at 11.7 μm intervals.
The suction device that was coupled to the OCT system was similar to that used previously for ultrasound measurements described in the previous chapter. A schematic representation and a picture of the suction device attached to the OCT system show the air-filled pressure chamber which was attached to the skin with double adhesive tape, and consisted of a unit which could be detached to vary the aperture diameter (figures 3.1 and 3.2). Three different aperture diameters were used: 1, 2 and 6 mm. OCT measurements using all aperture sizes were carried out on both dry (normal) and hydrated skin to study the effect of hydration on the mechanical behaviour. To limit evaporation of water from hydrated skin, a small drop of water was placed on the skin during the measurement.

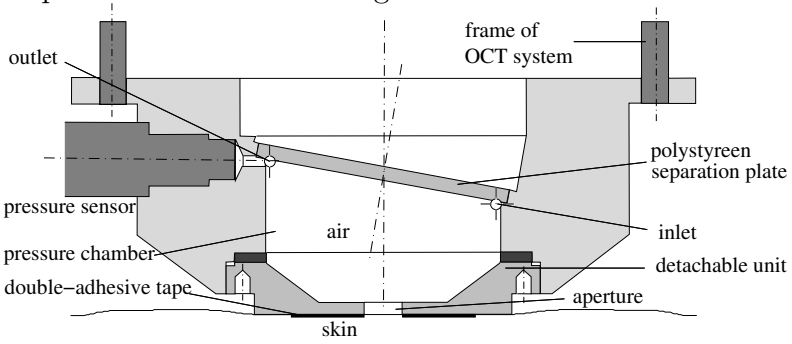

Figure 3.1: *Schematic representation of the suction device attached to the OCT system. The device consists of a pressure chamber that can be closed to load the skin through the aperture and of a water filled part which connects the pressure chamber to the ultrasound system. The detachable unit enables use of various aperture sizes.*

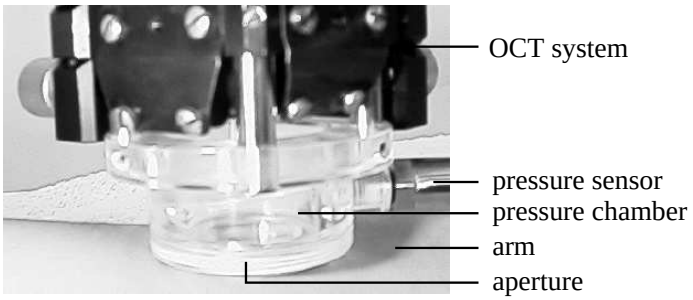

Figure 3.2: *Picture of the suction device attached to the OCT system.*

Air was withdrawn in 7 steps such that the skin was loaded with a maximum pressure of 20 kPa (200 mbar) in the 6 mm aperture measurements and with a maximum pressure of 35 kPa (350 mbar) in the 1 and 2 mm aperture measurements. After each step the pressure was measured and simultaneously a 3D image of the deformed skin was made.

Data analysis OCT

For the calculation of the skin surface displacement, in each image the location of maximum intensity for each vertical line was found. This location represents the skin surface. The skin surface displacement could then be obtained by comparing the images of each load step with the image of undeformed skin. For each load step, the location of the skin surface was averaged over the 10 slices.
To determine the thickness of the epidermis, the skin surface was transformed to a flat surface (figure 3.3, left) such that the maximum intensity (caused by the reflection at the skin surface) was located at a fixed depth, set to 0 (Neerken et al., 2003). For all ten images of each single measurement an intensity profile and the epidermal thickness were determined (figure 3.3, right).

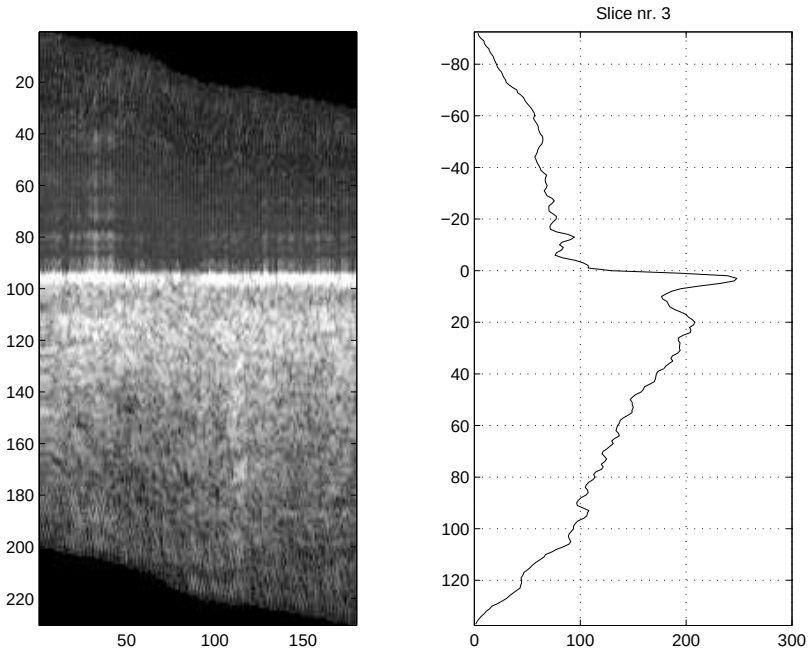

Figure 3.3: *Left: OCT image with flattened skin surface (depth × width, values in pixels). Right: intensity profile of the OCT image (depth in pixels versus signal intensity in arbitrary units).*

The intensity profile was calculated from integration of the signal along the lateral position as a function of depth in each image. An intensity profile of the forearm shows two peaks, caused by the two bright reflecting bands. The first peak is caused by the skin surface. The skin surface is defined at the depth at which the intensity of the first peak has reached half of its maximum (corresponding to 0 at the vertical axis). The second peak is caused by the reflection of dermal fibres. The location of the fibres was determined relative to the skin surface by calculating the position at which the second peak has reached half of its maximum intensity on the ascending slope. The layer between the first and second peak corresponds with the epidermis and the papillar dermis together (Neerken et al., 2003).

In the following this layer will be referred to as the upper layer. The measured optical thickness of this layer, t'_{ul}, was corrected for the refractive index to obtain the real physical thickness t_{ul}:

$$t'_{ul} = \frac{t_{ul}}{n} \tag{3.1}$$

where n is the refractive index of the tissue, which was assumed to be constant at 1.4 for all skin layers (Tearney et al., 1995).
For each load step the thickness of the upper layer was averaged over the 10 images. To reduce the effect of varying thickness across the aperture due to suction, the thickness of the upper layer was calculated for only part of the image.

3.2.2 Experimental set-up: ultrasound

The experimental set-up was described in the previous chapter and will be summarized. 20 MHz ultrasound was employed during the suction experiment to measure the deformation of the skin. A commercially available ultrasound system was used: DUB 20 (Taberna Pro Medicum, Germany). The obtained axial resolution was 79 μm. The pressure chamber was attached to the skin with double-sided adhesive tape. The aperture diameter was 6 mm. Distilled water was added to the pressure chamber to serve as coupling liquid for the ultrasound. Water was withdrawn in several steps such that the skin was uplifted approximately 1.2 mm or that the maximum pressure was approximately 35 kPa. Immediately after each step, the pressure was measured with a Kulite pressure sensor and simultaneously a 2D image of the deformed skin was made.

Data analysis ultrasound

For the calculation of the skin surface displacement and the thickness of the skin composite from the ultrasound images, the same method was used as for the OCT images. No averaging was needed as one ultrasound image consisted of merely 1 slice, whereas the OCT images consiseted of 10 slices. The intensity profile of the ultrasound images shows two peaks. The thickness of the skin composite was defined as the distance between the first (skin surface) and the last peak (dermis-fat interface) and was calculated using a sound velocity of 1580 m/s (Serup et al., 1995).

3.2.3 Experimental protocol

Subjects: Measurements were performed on 13 male subjects aged 29-47 years old. All subjects were healthy and of Caucasian skin type. All volunteers gave informed consent. Measurements were carried out in climate controlled test rooms at 22 °C and 50 % relative humidity after 15 minutes acclimatization. Subjects were seated upright with their arm resting on towels or a cushion in a relaxed position (figure 2.2).

Measurement area: Measurements were performed on 3 sites (a, b and c) located 4, 7 and 10 cm from the elbow on the volar site of both arms. This site was chosen since it is easily accessible and relatively flat. On one arm measurements were performed on hydrated skin, on the other arm measurements were performed on dry skin. To ensure a maximum hydrated stratum corneum, the skin was hydrated at least 40 minutes (Hendriks and Lucassen, 2001). Prior to the measurement, the level of hydration was checked with a Corneometer CM 825 (Courage & Khazaka Electronic GmbH, Germany). To ensure that only the effect of varying aperture size and hydration was measured, and not the influence of the different test site, the measurement site was randomized for aperture diameter, and left and right arm were varied for dry and hydrated skin, as described in appendix 3.5. The thickness of the skin composite was measured for each test site using ultrasound. The ultrasound suction measurement was applied on the same test site as where the 6 mm aperture OCT suction experiment was applied on dry skin, after the skin was allowed to relax for at least one hour.
Suction measurement: In the 6 mm aperture measurements, the skin was loaded with 0, 2.5, 5.0, 7.5, 10, 12.5, 15 and 20 kPa suction pressure. In the 2 and 1 mm aperture measurements, the skin was loaded with 0, 5.0, 10, 15, 20, 25, 30 and 35 kPa suction pressure. To obtain reproducible results in an acceptable time period for the subjects (one of the test sites is measured twice), it was chosen to precondition the skin by loading it 5 times until maximum pressure was reached (i.e. 20 kPa for 6 mm aperture and 35 kPa for 1 and 2 mm aperture).

3.2.4 Finite element model

An axi-symmetric finite element model was developed in MSC.MARC (MSC Software Corporation, 2001). For 4 subjects, for each aperture size and measurement site a dedicated FE mesh was made, based on the thickness of the upper layer and the skin composite obtained from the OCT and ultrasound images at that site (figure 3.4).

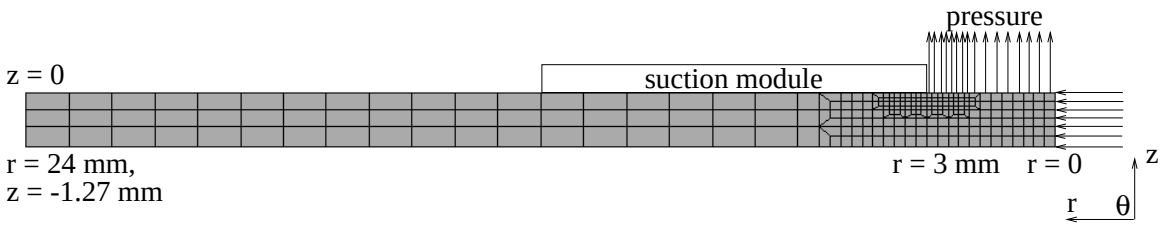

Figure 3.4: *FE mesh and boundary conditions for 6 mm aperture OCT measurement on dry skin for subject 5.*

The skin surface under the aperture plate of the suction module was fully restrained. The dermis-fat interface was left free, as removal of the fat layer from the simulations did not affect the overall mechanical response due to its low stiffness as was detailed in the appendix of the previous chapter.

The skin was assumed to be isotropic and incompressible. By allowing the skin to relax before measuring, time-dependent behaviour can be ignored. Extended Mooney material behaviour was modelled to account for the non-linear stress-strain relationship of the skin. The following strain energy function was used

$$W = C_{10}(I_1 - 3) + C_{11}(I_1 - 3)(I_2 - 3) \tag{3.2}$$

and is based on the strain energy function by James, Green and Simpson (MSC Software Corporation, 2001, 2000), where I_1 and I_2 are the first and second invariants of the Finger strain tensor $\mathbf{B}$. For small strains the contribution of the second part of the equation is negligible and C_{10} can be converted into a Young's modulus using $E = 6\ C_{10}$.

3.2.5 Parameter identification

An iterative procedure was used to adjust the parameters of the material model. This procedure was performed in MATLAB (The MathWorks Inc, Magrab et al. (2000)). It adjusts the material parameters in the input file of the FE model, runs the FE simulation, extracts the relevant results from the simulation (skin surface displacements at various pressure levels), and compares the results from the simulation with the experimental results. The results were used to evaluate an objective function O that needs to be minimized:

$$O = \ln \sum_{i}^{n} \left(\frac{x_{i,num} - x_{i,exp}}{x_{i,exp}}\right)^2, \tag{3.3}$$

where $x_{i,exp}$ is the experimentally obtained displacement of the skin surface at observation i and $x_{i,num}$ is the numerically obtained displacement of the skin surface at observation i. The number of observations is n.
A standard constrained non-linear optimization function in MATLAB was used to minimize this objective function for the material parameters C_{10} and C_{11} (Coleman et al., 1999). The displacements of the skin surface, x_i, at various pressures p_i, are the results that were used to identify the material parameters. The applied pressures p_i were used as an input to the finite element model.

3.2.6 Verification of the method

To verify the method, and to characterize the mechanical behaviour of the tape that was used, the tape was tested using a uniaxial tension machine and the OCT set-up using 6 mm aperture diameter. The results from the suction experiment and the tension test were in good agreement. For the tape $C_{10} = 8$ MPa and $C_{11} = 18$ GPa was found. Therefore, the tape can be assumed to be rigid compared to the skin and was integrated in the suction module in the finite element models.

3.3 Results

3.3.1 Experiments: optical coherence tomography

Figure 3.5 shows a typical OCT image of the volar forearm skin at zero suction state and at 35 kPa suction (subject 5, hydrated skin). The aperture size is 2 mm. The figure reveals the entrance echo caused by the water-stratum corneum interface (skin surface), the epidermis and papillar dermis (ED+PD) and the reticular dermis (RD). The stratum corneum cannot be distinguished from the living epidermis due to the system's resolution of 14 μm. In the centre of the aperture, a thickness of 144 μm was found for the upper layer. After preconditioning, its thickness was 156 μm. This increase falls within the system's resolution of 14 μm. Application of 35 kPa suction caused the thickness of the upper layer to decrease to 128 μm. The skin surface moved upward 0.49 mm.

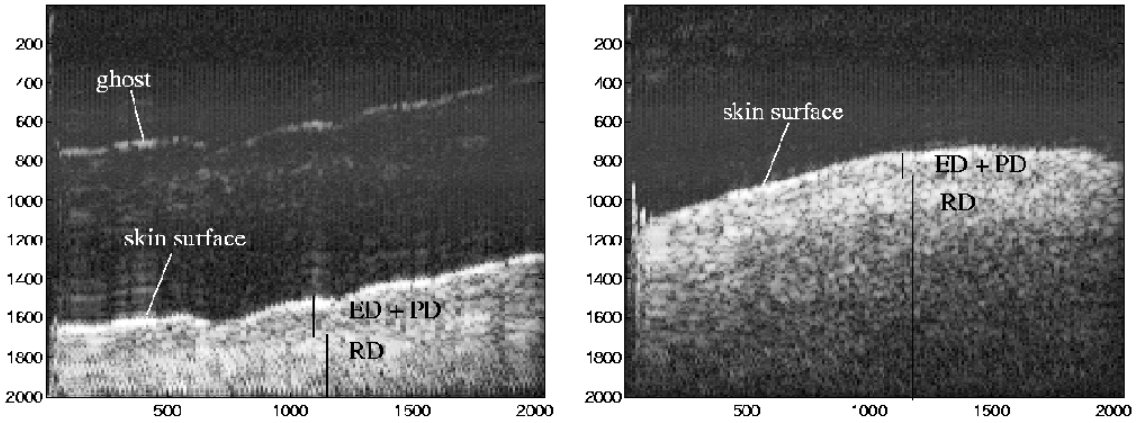

Figure 3.5: *OCT image (1 of 10 slices) of forearm skin at atmospheric pressure (left) and at 35 kPa suction (right). From top to bottom: air (black), entrance echo (bright) representing the skin surface, epidermis and papillar dermis (grey), fibres in reticular dermis (second bright band) and reticular dermis (grey and fading). Reflections in the separation plate cause a ghost. The edges of the aperture (2 mm) are just outside of the image. The skin surface at these edges appear not at equal x-position, this is an artefact which is corrected for in the image analysis. Numbers at the axes are in micrometers and are not corrected for refractive index of the skin (n=1.4).*

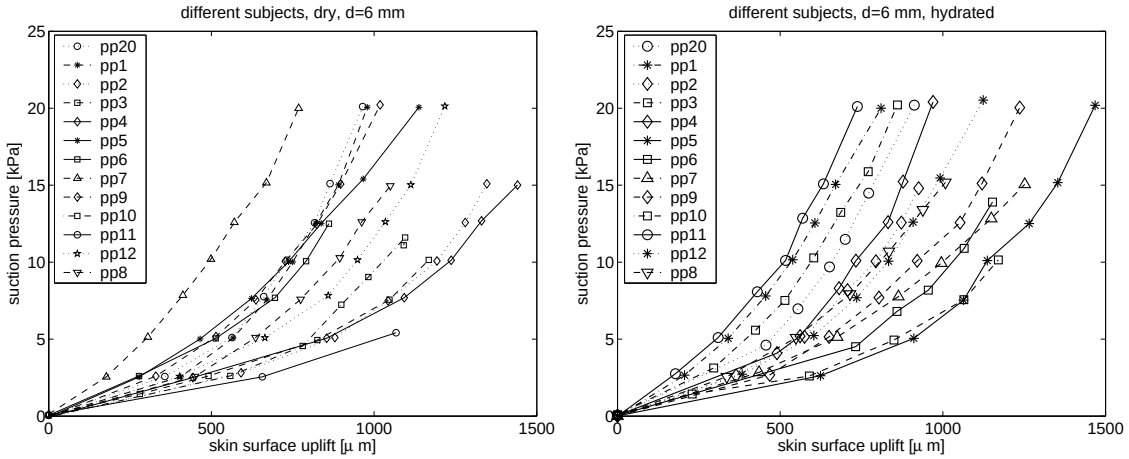

Figure 3.6: *Experimentally obtained pressure-displacement curves for all subjects, measured with 6 mm aperture OCT set-up on dry (left) and hydrated skin (right).*

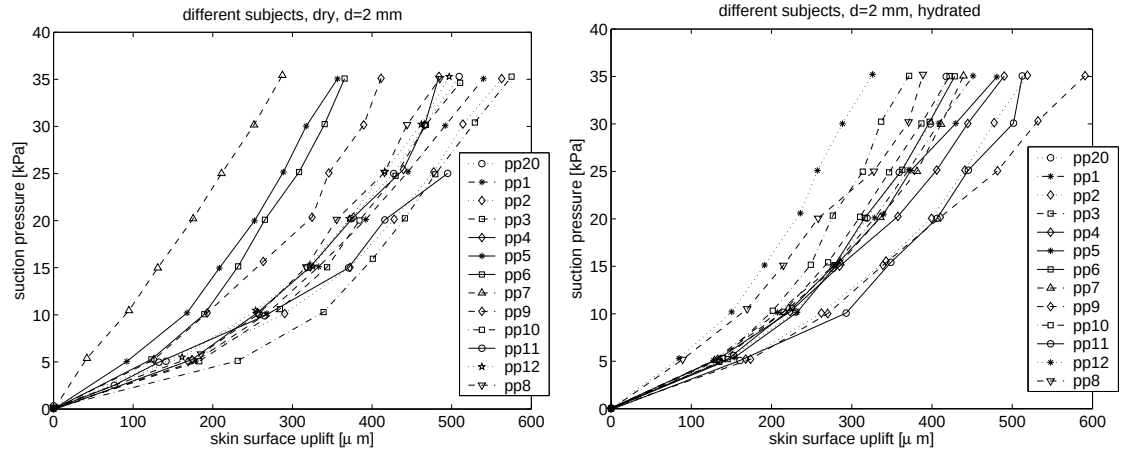

Figure 3.7: *Experimentally obtained pressure-displacement curves for all subjects, measured with 2 mm aperture OCT set-up on dry (left) and hydrated skin (right).*

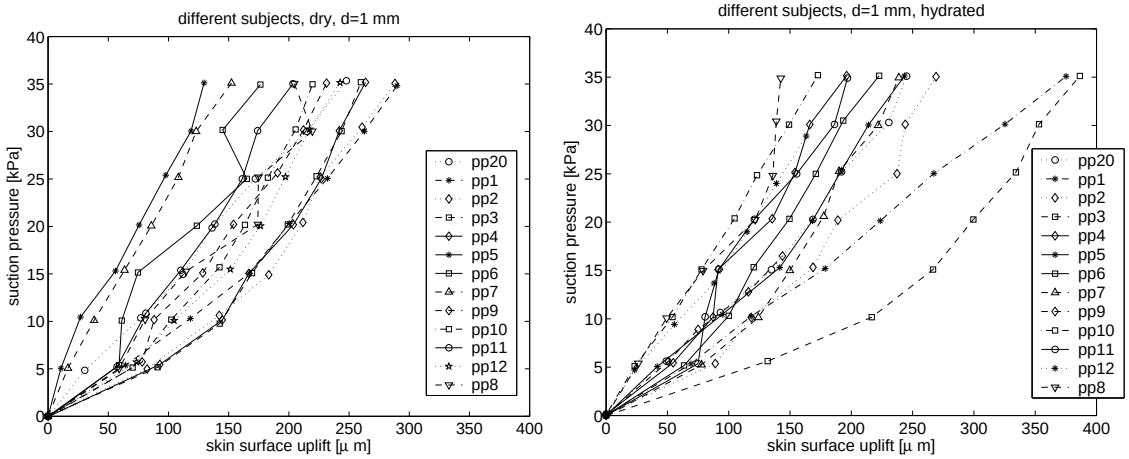

Figure 3.8: *Experimentally obtained pressure-displacement curves for all subjects, measured with 1 mm aperture OCT set-up on dry (left) and hydrated skin (right).*

Figure 3.6 shows the measured pressure-skin surface displacement on dry and hydrated skin for all subjects for 6 mm aperture. The curves are clearly non-linear. Large variations between the subjects can be seen: up to a factor of 4 for the measured displacements. Similar curves, but with smaller displacements are found for 1 and 2 mm aperture (figures 3.7 and 3.8). Note that the scales along the x-axes are different.

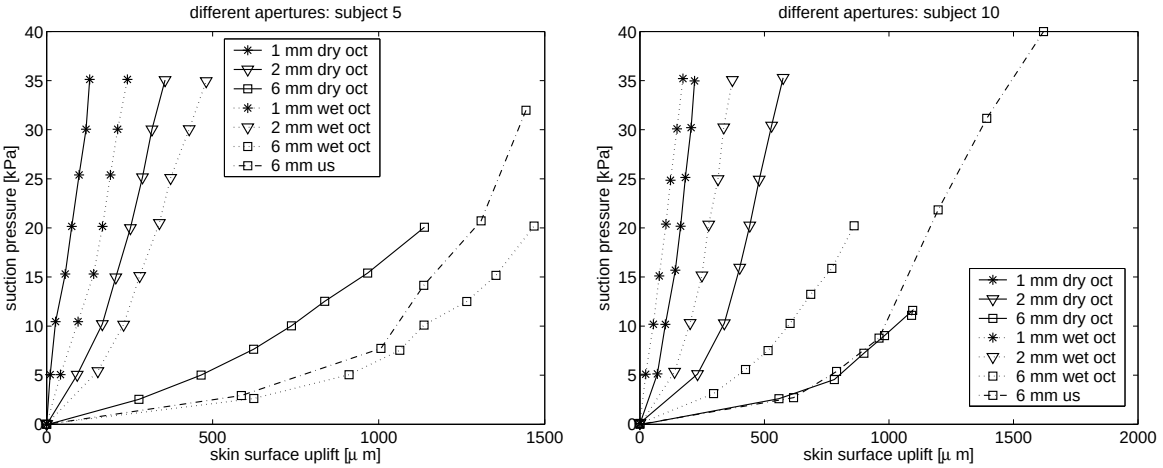

Figure 3.9: *Experimentally obtained pressure-displacement curves for subject 5 (left) and subject 10 (right), showing OCT measurements with three aperture sizes on hydrated and dry skin and 6 mm aperture ultrasound measurement (on wet skin).*

Figure 3.9 shows typical pressure-skin surface displacement curves for measurements with all aperture sizes on hydrated and dry skin on one subject (subject 5 and subject 10, respectively). Also the pressure-displacement curve measured with the US set-up is shown. The figures clearly show that increasing the aperture diameter leads to larger skin uplifts. This was found for all subjects. Secondly, they show reasonable correlation between ultrasound and 6 mm aperture OCT measurements on hydrated skin. Finally, the figure for subject 5 shows an increasing elevation for hydrated skin. This effect was found in 4 subjects. However, for subject 10 a decreased elevation was found for hydrated skin. This effect was found in 8 subjects. In one subject, no effect due to hydration was found. This can also be seen from table 3.1 which shows the increase in skin elevation in percentage due to hydration (relative to dry skin) for all aperture sizes and subjects.

Table 3.1: *Increase in skin uplift (in percentages) due to stratum corneum hydration for all subjects for various aperture diameters (in mm).*

	p20	p1	p2	p3	p4	p5	p6	p7	p9	p10	p11	p12	p8	mean ± std
⊘ 1	10	10	-9	50	-40	80	46	70	0	-35	0	-29	-30	10.3 ± 42
⊘ 2	-15	-18	-9	-21	-11	35	20	60	35	-32	0	-34	-27	-1.3 ± 30
⊘ 6	-11	-25	-30	0	-40	40	30	100	10	-40	-71	-13	-9	-4.4 ± 43

Thickness of the upper layer at atmospheric pressure is presented in table 3.2 for all measurement sites in each subject (*la* means left arm, site *a*; *rb* right arm, site *b*). The table also shows the average and standard deviation per subject (between measurement sites) and per measurement site (between subjects) and which arm was hydrated. The variation per subject and per measurement site for all subjects were in the same order of magnitude and were twice the system's resolution. The average thickness of the upper layer for all subjects and all measurement sites was 143 ± 20 μm. The changes in the thickness of the upper layer due to loading and hydration fell within the resolution of the measurement system (not shown here).

Table 3.2: *Thickness of the upper layer (in μm) measured with OCT for all measurement sites and all subjects.*

	p20	p1	p2	p3	p4	p5	p6	p7	p9	p10	p11	p12	p8	av.	std
left	dry	wet	dry	wet	dry	wet	dry	wet	wet	dry	wet	dry	dry		
la	125	151	155	162	132	150	208	150	157	107	166	–	143	151	2.5
lb	129	121	151	162	138	156	150	146	138	125	154	137	119	140	14
lc	114	118	155	143	115	143	168	146	140	130	139	110	107	133	19
ra	151	150	151	150	107	136	196	153	129	133	178	130	166	148	23
rb	113	143	156	176	143	135	128	132	124	172	187	127	142	144	22
rc	143	133	180	154	172	136	168	130	115	124	156	113	134	143	21
right	wet	dry	wet	dry	wet	dry	wet	dry	dry	wet	dry	wet	wet		
av.	129	136	158	158	135	143	170	143	134	132	163	123	135		
std	15	14	11	12	23	8.7	29	9.6	15	22	17	12	21		

3.3.2 Experiments: ultrasound

Figure 3.10 shows the pressure-skin surface displacement for all subjects measured with ultrasound. It shows variations up to a factor of 5 between subjects for the measured displacement at a certain pressure. During the test on subject 1, the ultrasound set-up failed. Therefore, no ultrasound results are available for this subject. Thickness of the skin composite at atmospheric pressure is presented in table 3.3 for all measurement sites and subjects. The average thickness of the skin composite for all subjects and all sites is 1.08 ± 0.16 mm.

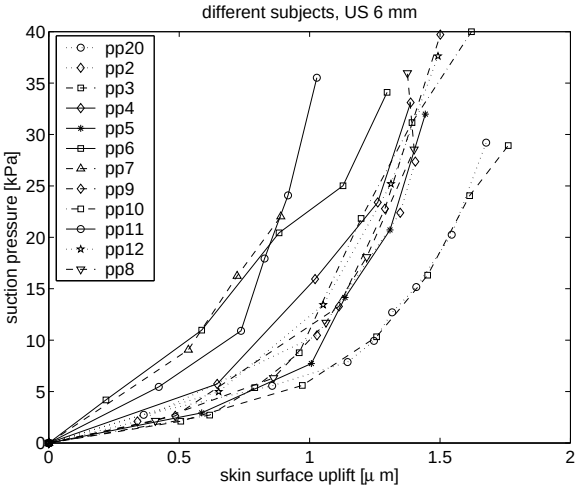

Figure 3.10: *Experimentally obtained pressure-displacement curves for 12 subjects, measured with 6 mm aperture US set-up on wet skin.*

Table 3.3: *Thickness of the skin composite (in mm) at different sites for all subjects from 6 mm US measurements.*

	p20	p2	p3	p4	p5	p6	p7	p9	p10	p11	p12	p8	av.	std
la	1.00	0.85	1.06	1.17	1.01	0.98	1.08	1.00	1.01	0.97	1.16	1.19	1.04	0.10
lb	0.90	0.90	0.93	0.68	1.44	1.12	1.12	1.06	1.19	1.09	1.11	1.19	1.06	0.19
lc	1.09	0.85	0.95	0.93	1.19	0.98	1.20	1.03	1.12	1.34	1.16	1.53	1.12	0.19
ra	1.06	0.85	1.01	0.85	1.27	1.11	0.97	0.98	0.97	1.01	1.30	1.06	1.04	0.14
rb	1.00	0.93	1.01	0.93	1.50	1.19	1.30	0.97	0.97	1.16	1.33	1.22	1.12	0.19
rc	1.16	0.87	1.01	0.84	1.12	1.28	1.19	0.92	1.17	1.20	1.33	1.27	1.11	0.17
av.	1.03	0.88	1.00	0.90	1.26	1.11	1.14	0.99	1.07	1.13	1.23	1.24		
std	0.09	0.03	0.05	0.16	0.19	0.12	0.12	0.05	0.10	0.14	0.10	0.16		

3.3.3 Numerical model and parameter identification

Pressure-displacement curves for the experimental data and the prediction of the finite element model for three aperture sizes on dry skin show good correlation (figure 3.11 shows the curves for subject 12). The corresponding estimated material parameters (table 3.4) show increasing values with increasing aperture size for all subjects. The figure and the table show that the used finite element model exhibiting extended Mooney behaviour was able to describe the experimentally observed response. Except for one case, where the model was not able to describe the experimental results correctly, as the data were very scattered. However, the table also shows that the model was not able to describe the responses for all three aperture diameters with the same material parameters. A larger aperture diameter led to increased values for the material parameters, although the same material (the skin of one subject) was modelled.

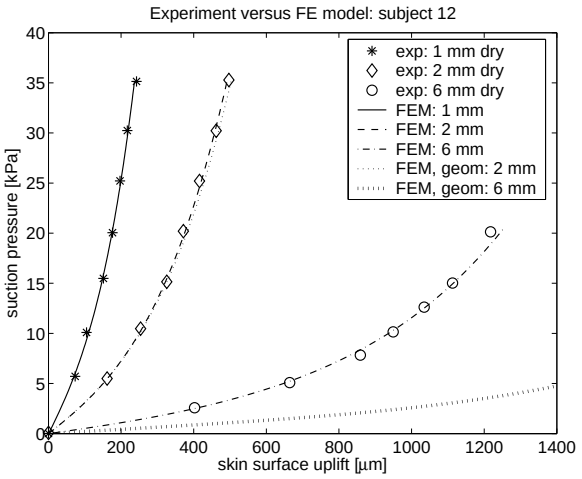

Figure 3.11: *Experimentally obtained and simulated pressure-displacement curves for subject 12, measured with 1, 2 and 6 mm aperture OCT set-up on dry skin. Dotted lines represent FEM simulations for 2 (FEM, geom: 2 mm) and 6 mm aperture (FEM, geom: 6 mm) with the material parameters as calculated for the 1 mm aperture.*

Table 3.4: *Estimated material parameters (C_{10} and C_{11} in kPa) for suction on dry skin with 1, 2 and 6 mm aperture for 4 subjects.*

	⊘ 6 mm		⊘ 2 mm		⊘ 1 mm	
	C_{10} [kPa]	C_{11} [kPa]	C_{10} [kPa]	C_{11} [kPa]	C_{10} [kPa]	C_{11} [kPa]
p3 (weak)	18.9	125	5.22	20.2	4.17	14.7
p5 (average)	22.7	222	9.91	34.4	-	-
p7 (stiff)	60.9	1412	24.2	4.11	21.7	0.50
p12 (average)	15.8	216	6.52	14.4	6.63	12.7
mean	29.6	494	11.5	18.3	10.8	9.3
stdev	21.1	614	8.7	12.6	9.5	7.7

3.4 Discussion

Two experimental set-ups were employed. The set-up using OCT was successfully used to determine the thickness of the upper layer (epidermis + papillar dermis) and skin surface displacements caused by suction. With the set-up using US, skin surface displacement and thickness of the skin composite were obtained. Both 6 mm aperture suction measurements using US and OCT led to the corresponding pressure-displacement curves. The curves resulting from the current US suction experiment (displacements of 0.8 - 1.55 mm at 20 kPa suction) agree with the results from the previous chapter (displacements of 1.1 - 1.8 mm at 20 kPa suction) and are also in agreement with that of Diridollou et al. (1998), who found a skin elevation of approximately 1.05 mm for 20 kPa suction. The thickness of the skin composite measured in the previous chapter(1.35 ± 0.1 mm) was slightly larger than that in this chapter (1.08 ± 0.16). This can be caused by a higher age of the subjects in this study, although both values agree with values from the literature.
The values for the material parameters ($C_{10} = 29.6 \pm 21.1$ kPa and $C_{11} = 493 \pm 613$ kPa for 6 mm aperture diameter) were much higher than those found in the previous experiment ($C_{10} = 9.64 \pm 3.6$ kPa and $C_{11} = 82 \pm 60$ kPa, Hendriks et al. (2003)). This difference is larger than expected on the small difference in the pressure-displacement curves alone, and it shows that skin thickness has to be included in the model to find reliable material properties from suction experiments. One explanation for the increased stiffness may be the higher age of the subjects in this study. A second explanation may be the preconditioning of the skin in this study. In the previous chapter the skin was not preconditioned. From preliminary studies it appeared that preconditioning caused a decrease in maximum skin elevation of approximately 30% for the 6 mm aperture.

Results of 2 mm suction measurements by Barel et al. (1995) who measured skin elevations of approximately 0.10, 0.20 and 0.35 mm for 15, 25 and 35 kPa, respectively, fall within the range of our pressure-displacement curves for the 2 mm suction experiments. Barel calculated a Young's modulus of 0.13 - 0.26 MPa, which is higher than the value presented in this chapter ($E \approx 0.069 \pm 0.05$ MPa with $C_{10} = 11.5 \pm 8.7$ kPa). The explanation for this difference is that Barel calculated the Young's modulus in the second part of the stress-strain curve, whereas C_{10} represents the first part of this curve.

The pressure-displacement curves for one subject and varying aperture diameter (figure 3.9) show that displacement increases with increasing aperture diameters. This effect was not only caused by the changing aperture geometry. Comparison with numerically obtained pressure-displacement curves for different aperture sizes on skin with one set of material parameters (figure 3.11, dotted lines) showed that for larger aperture sizes a larger displacement is obtained than is seen in the experimentally obtained pressure-displacement curves. This effect was small for the 2 mm, but large for the 6 mm aperture diameter experiment. This means that for larger aperture sizes a stiffer material behaviour is measured, which results in increasing values for the material parameters with increasing aperture size (table 3.4). Or, to put it differently, with a larger aperture diameter stiffer behaviour is measured. This verifies our first hypothesis that measurements with different aperture diameters represent the mechanical behaviour of different skin layers. But it

also suggests that a finite element model consisting of one material layer is not sufficient to describe the mechanical response of the skin. Therefore, future research will focus on the development of a new finite element model, consisting of at least two material layers (reticular dermis and upper layer), to describe the total mechanical response of the skin for various aperture sizes. This model will then be used to identify the mechanical behaviour of these layers.

Hydration caused stiffer material behaviour in 8 of 13 cases, whereas it caused a less stiff material behaviour in 4 of 13 cases. In one case, no clear effect was found. So it seems that hydration indeed influences the mechanical properties, but the effect is different for different subjects. This means that the second hypothesis cannot be verified. The effect of hydration was measured by comparing left and right arms one of which was hydrated. From a preliminary study (performed on one female) it appeared that the variance in measured pressure-displacement curves between both arms is approximately 15%. Table 3.1 shows that part of the measurements on hydration lies within this range. Jemec and Serup (1990) showed, using the Dermaflex A (10 mm aperture diameter), that direct comparison of symmetrical regions on the arms is allowed, as no significant differences were found between the arms.

Our results agree with those by Murray and Wickett (1996), who hydrated forearm skin *in vivo* and measured its effect on the skin elevation caused by 10, 20, 35 and 50 kPa suction pressure with a Cutometer (2 mm aperture). In some cases they measured a (non-significant) increase of elevation, in other cases a (non-significant) decrease. Only for 20 kPa suction pressure they measured a significant increase in skin elevation.

Jemec *et al.* reported two *in vivo* experiments using the Dermaflex (Jemec et al., 1990, 1996). In one experiment they measured a slight increase in skin elevation after 20 minutes hydration of the skin with water. In the other experiment, with the same duration of hydration, they measured no effect on the skin elevation.

Auriol et al. (1993) performed suction experiments on 29 subjects using a Cutometer with 2 mm aperture diameter and 45 kPa suction. He measured an increase in skin elevation due to skin hydration up to 14%, depending on hydration time. He also split the results for male and female subjects. This resulted in a significant increase in elevation of 21% for women. However, for men, there appeared to be no significant change in skin elevation due to hydration. This observation was explained by the fact that women had a thinner dermis than men. Before hydration, the stiff stratum corneum plays an important role in the total skin response. After hydration, stiffness of the stratum corneum is decreased to the magnitude of dermal stiffness and the difference in dermal thickness becomes important.

In conclusion: measurements with different aperture diameters show the mechanical behaviour of different skin layers. To learn more about the effect of hydration, a closer look should be taken at the variance in mechanical response between left and right arm for the various aperture sizes. Another possibility is to measure hydrated and dry skin on the same site, but caution should be exercised to eliminate the effect of prior loading and removal of the loading device between measurements.

3.5 Appendix: Experimental protocol

For each subject the following steps were performed:

- Hydrate measurement sites of one arm.
- Perform suction measurement with 6 mm aperture diameter and OCT system at desired location of untreated arm.
- Hydrate this measurement site.
- Perform suction measurement with 2 mm aperture diameter and OCT system at desired location of untreated arm.
- Perform suction measurement with 1 mm aperture diameter and OCT system at desired location of untreated arm.
- Perform suction measurement with 6 mm aperture diameter and OCT system at desired location of hydrated arm and rehydrate this measurement site.
- Perform suction measurement with 2 mm aperture diameter and OCT system at desired location of hydrated arm and rehydrate this measurement site.
- Perform suction measurement with 1 mm aperture diameter and OCT system at desired location of hydrated arm and rehydrate this measurement site.
- Measure dermal thickness with ultrasound set-up at last five measurement sites.
- Perform suction measurement with 6 mm aperture diameter and US system at first measurement site.

Table 3.5: *Age and measurement site for each subject.*

		OCT on dry skin			OCT on hydrated skin			US
subject	age	⊘ 6 mm	⊘ 2 mm	⊘ 1 mm	⊘ 6 mm	⊘ 2 mm	⊘ 1 mm	⊘ 6 mm
p20	35	*lc*	*lb*	*la*	*rc*	*rb*	*ra*	*lc*
p1	35	*rc*	*rb*	*ra*	*lc*	*lb*	*la*	*rc*
p2	29	*lc*	*lb*	*la*	*rc*	*rb*	*ra*	*lc*
p3	29	*rb*	*rc*	*ra*	*lb*	*lc*	*la*	*rb*
p4	33	*lb*	*la*	*lc*	*rb*	*ra*	*rc*	*lb*
p5	34	*ra*	*rb*	*rc*	*la*	*lb*	*lc*	*ra*
p6	47	*la*	*lb*	*lc*	*ra*	*rb*	*rc*	*la*
p7	38	*ra*	*rc*	*rb*	*la*	*lc*	*lb*	*ra*
p9	33	*rc*	*ra*	*rb*	*lc*	*la*	*lb*	*rc*
p10	40	*lc*	*la*	*lb*	*rc*	*ra*	*rb*	*lc*
p11	31	*rb*	*ra*	*rc*	*lb*	*la*	*lc*	*rb*
p12	30	*lb*	*lc*	*la*	*rb*	*rc*	*ra*	*lb*
p8	33	*la*	*lb*	*lc*	*ra*	*rb*	*rc*	*la*

Chapter 4

A two-layer finite element model to study the relative contributions of the different skin layers to the mechanical behaviour of human skin

The contents of this chapter are based on Hendriks et al. (2004b). **The relative contributions of the different skin layers to the mechanical behaviour of human skin *in vivo* using suction experiments.** *Medical Engineering and Physics*, submitted.

4.1 Introduction

The previous chapter showed that with suction measurements at 1, 2 and 6 mm aperture diameter increasing displacements were measured with increasing aperture diameter. Parameter estimation with a single layer finite element model resulted in increasing values of material parameters with increasing aperture diameter. This verified the hypothesis that with the use of experiments at different aperture diameters, the mechanical response of different skin layers could be evaluated. It also suggested that a finite element model consisting of one material layer, is not sufficient to describe the mechanical response of the skin to experiments at different aperture diameters. Therefore, the objective of the work described in this chapter, was to develop a two-layer finite element model to simulate the suction experiments at 1, 2 and 6 mm aperture diameter, as described in the previous chapter, with one set of material parameters. The finite element model comprised two layers, the reticular dermis and the upper layer, defined as the combined epidermis and papillar dermis. By comparing the initial part of the experimental data and the numerical results, the material parameters of these layers were estimated.

4.2 Materials and methods

4.2.1 Finite element model

To determine the mechanical properties of the upper layer and the reticular dermis, a two-layer model was developed. This involved an axi-symmetric finite element model developed using commercial software (MSC.MARC, MSC.Software Corporation, 2003). Three specific models were made for the measurements at 1, 2 and 6 mm aperture diameter for one subject (subject 7, untreated skin of the group mentioned in the previous chapter, refer to figures 3.6 - 3.8), based on the appropriate thicknesses of the upper layer and the reticular dermis obtained from the OCT and ultrasound images (figure 4.1: mesh for 1 mm aperture diameter).
The skin surface under the aperture plate of the suction module was fully restrained. The dermis-fat interface was left free, as removal of the fat layer from the simulations did not affect the overall mechanical response due to its low stiffness as was detailed in chapter 2.

Like in the previous chapters, the skin was assumed to be incompressible, isotropic in the plane parallel to the skin surface and independent of time-dependent behaviour. In the previous chapter, a single layer model was developed using Mooney material behaviour to account for the non-linear stress-strain relationship of the skin. The following strain energy function, based on that by James, Green and Simpson (MSC Software Corporation, 2001, 2000) was used,

$$W = C_{10}(\mathbf{I}_1 - 3) + C_{11}(\mathbf{I}_1 - 3)(\mathbf{I}_2 - 3). \tag{4.1}$$

where I_1 and I_2 are the first and second invariants of the Finger strain tensor $\mathbf{B}$, and C_{10} and C_{11} are material parameters.

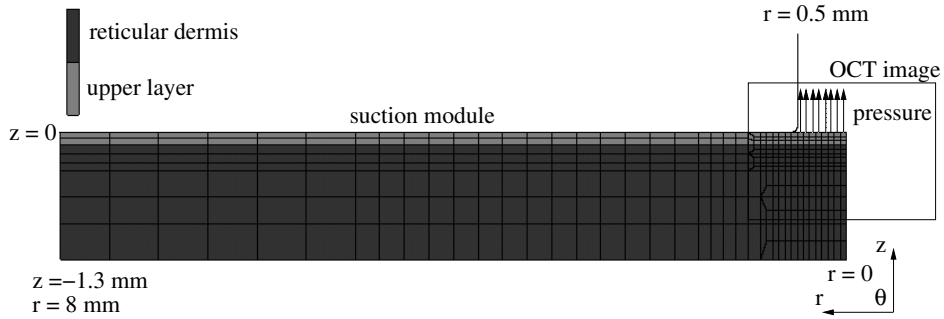

Figure 4.1: *Two-layer finite element mesh for 1 mm aperture OCT measurement showing the upper layer, reticular dermis, applied pressure, suction device and the area which was imaged by the OCT system. The skin surface under aperture plate of the suction module was fully restrained. The dermis-fat interface was left free. The radius of the edge of the aperture was 0.2 mm.*

The focus of the present chapter was to determine the material parameters of the upper layer and the reticular dermis separately. Therefore, the model simulated only small displacements, produced by pressures up to 10% of the experimentally applied pressure. The strain energy function then reduces to

$$W = C_{10}(\mathbf{I}_1 - 3) \tag{4.2}$$

and only two material parameters need to be identified: $C_{10,ul}$ for the upper layer and $C_{10,rd}$ for the reticular dermis.

4.2.2 Parameter identification

An iterative procedure similar to that described in the previous chapters, was used to adjust the parameters of the material model, $C_{10,ul}$ and $C_{10,rd}$, based on MATLAB (The MathWorks Inc, Magrab et al. (2000)). The measured pressure-displacement curves at small displacements were smoothed by using the single layer model results. A best fit, representing minimal difference between the experimental and numerical results, was found by minimizing the objective function O defined as

$$O = \ln \sum_{j}^{3} \frac{1}{n} \sum_{i}^{n} \left(\frac{x_{i,j,num} - x_{i,j,exp}}{x_{i,j,exp}}\right)^2 , \tag{4.3}$$

where $x_{i,j,exp}$ is the experimentally obtained axial displacement of the skin surface in the centre of the aperture at observation i for experiment j with aperture diameter 1, 2 or 6 mm. $x_{i,j,num}$ is the numerically obtained axial displacement of the skin surface in the centre of the aperture at observation i in experiment j. The number of observations in one experiment is n. A standard constrained non-linear optimization function in MATLAB was used to minimize the objective function for the material parameters $C_{10,ul}$ and $C_{10,rd}$ (Coleman et al., 1999).

4.3 Results

4.3.1 Two-layer finite element model

A sensitivity study was performed to obtain initial estimates for the parameter estimation procedure. The value of the objective function O (equation 4.3) indicating the difference between the numerical and the experimental results, was calculated by forward analyses for various combinations of discrete values of the material parameters of both layers, and a contour plot was produced (figure 4.2). It shows a minimum value for the objective function at approximately $C_{10,rd} = 0.17$ MPa and $C_{10,ul} = 0.1$ kPa.

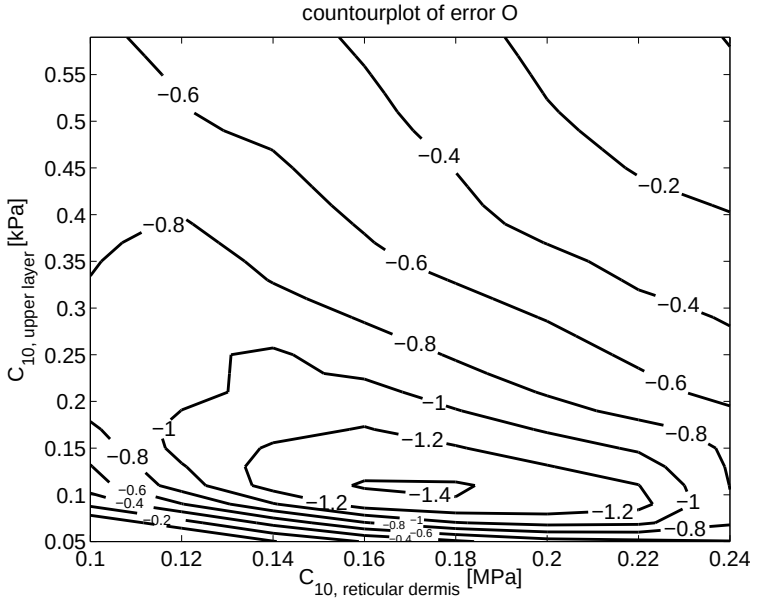

Figure 4.2: *Contour plot of the value for the objective function O for various combinations of stiffness of the upper layer and the reticular dermis. The minimum value of O indicates the smallest difference between the experimental and numerical results for the experiments of subject 7 at all 3 aperture diameters and small displacements. Note the different scales along the axes.*

When those values were used as initial estimate in the automatic parameter fit procedure, values of $C_{10,rd}$ and $C_{10,ul}$ were found to be 0.16 MPa and 0.11 kPa, respectively. It is evident that the upper layer has a much lower stiffness than the reticular dermis.

Experimental data for small displacements using the three apertures, on which have been superimposed curves representing the simulations with the two-layer model (figure 4.3) show that that the simulations were able to model the experimental data associated with the aperture diameters of 1 mm and 6 mm. However, the two-layer model was not able to predict the experimental data associated with the 2 mm aperture and the selected material parameters, yielding a curve which more closely modelled the 1 mm data.

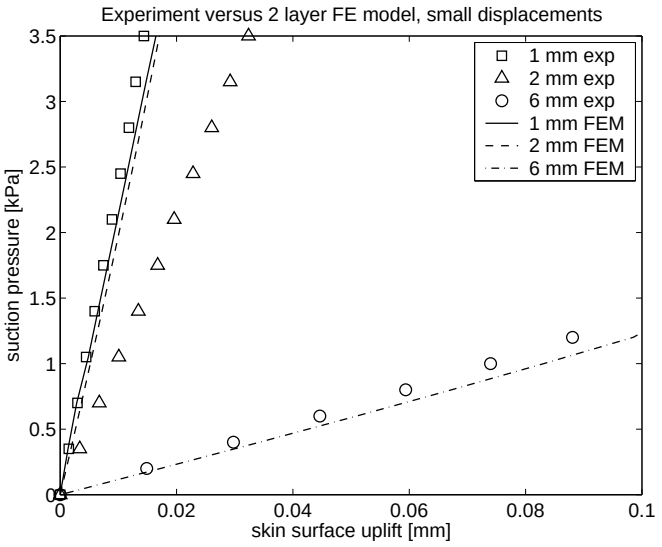

Figure 4.3: *Pressure-displacement curves for 1, 2 and 6 mm aperture diameter and small displacements (subject 7, untreated skin). Symbols represent the experiment (smoothed with the single layer model); lines represent the simulations with the two-layer models with* $C_{10,rd} = 0.16$ *MPa and* $C_{10,ul} = 0.11$ *kPa.*

These anomalies with aperture diameter were examined at constant values of both layer thicknesses (1.19 mm for total skin and 130 μm for the upper layer) and material parameters ($C_{10,rd} = 0.2$ MPa and $C_{10,ul} = 0.1$ kPa) were kept constant. For a single layer model, uplift decreases with decreasing aperture diameter at constant pressure. For the two-layer model, the uplift also decreased with reduction in aperture diameter from 6 to 1.5 mm. However, at diameters decreasing from 1.5 to 0.3 mm, the uplift increased (figure 4.4, solid line). This suggests that at diameters smaller than 1.5 mm, the influence of the upper layer becomes more influential in the total mechanical response. However, in the present experiments, this threshold point defined as the minimum in the curve, at 1.5 mm aperture diameter was not apparent over the range of aperture diameters from 1 to 6 mm.

Uplift versus aperture diameter curves for various ratios of stiffness for the reticular dermis and upper layer (figure 4.4) show that the aperture diameter at the threshold point decreases with reduction in stiffness ratio. All pressures were normalized, such that the minimum uplift was the same for all aperture diameters.

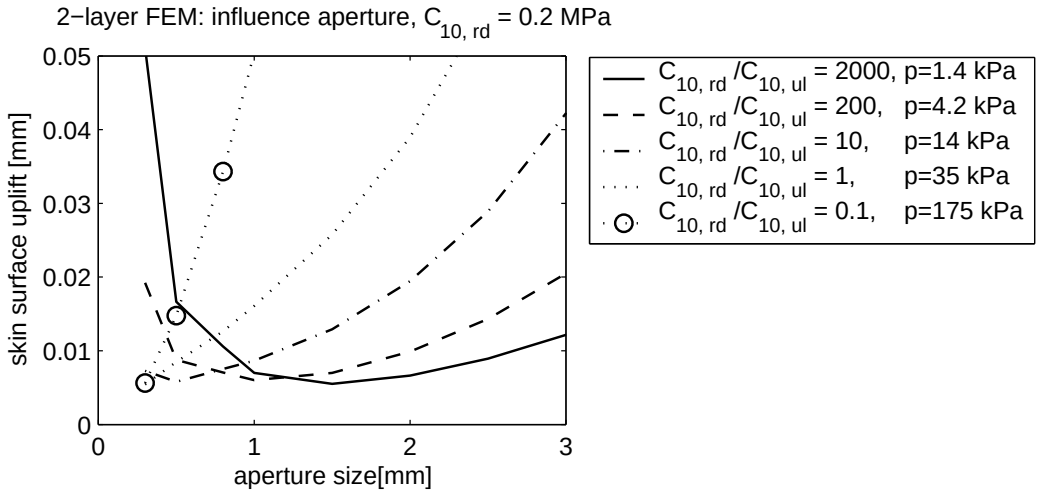

Figure 4.4: *Skin surface uplift versus aperture diameter for two-layer FE simulations with various stiffness ratios.*

It is also worthy of note that with a large stiffness ratio, there is a distinct change in deformation mode (figure 4.5). Simulations of the deformed skin at 0.3, 0.5, 1.5 and 6 mm aperture diameter and $C_{10,rd} = 0.2$ MPa and $C_{10,ul} = 0.1$ kPa show that at the smallest aperture diameter, the soft upper layer is drawn into the aperture, whereas the relatively stiff dermis is negligibly affected. With increasing aperture size, the upper layer close to the wall of the aperture is highly deformed and drawn into the aperture, whereas in the centre of the aperture, both upper layer and reticular dermis are drawn into the aperture. With decreasing stiffness ratio this change in deformation mode becomes less pronounced for aperture diameters ranging from 0.3 to 6 mm.

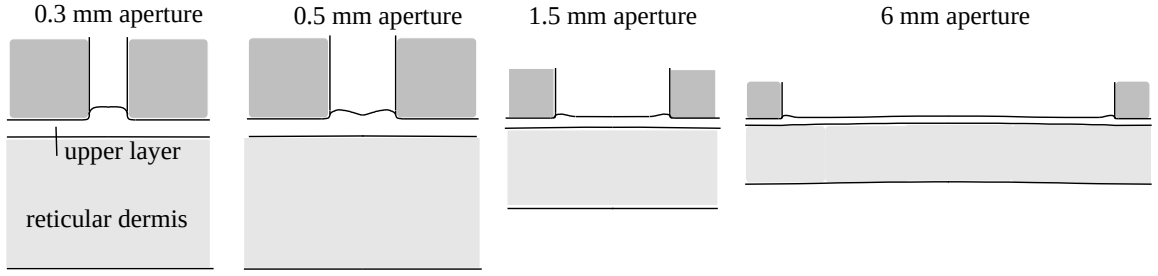

Figure 4.5: *Deformation modes of two-layer FE models with various aperture diameters. $C_{10,rd} = 0.2$ MPa and $C_{10,ul} = 0.1$ kPa (stiffness ratio = 2000). Note that the images are not equally scaled.*

4.4 Discussion

The objective of the current chapter was to present a two-layer finite element model to simulate the suction experiments at 1, 2 and 6 mm aperture diameter, as described in the previous chapter, with one set of material parameters in order to determine the mechanical properties of the upper layer and the reticular dermis of the skin. The basic hypothesis was that by combining suction experiments with different apertures of 1, 2 and 6 mm it should be possible to separate the behaviour of the distinct layers. It was shown that by combining these experiments and simulating them with a two-layer model it is indeed possible to separate the properties of the top-layers.

However, close examination of the data revealed that the two-layer model was not able to simulate the experimental data for all individual subjects. In particular, due to the large difference in stiffness the existing software supporting the two-layer model could not account for large displacements. Therefore, the model was used to simulate the initial part of the experimental data of merely one subject, namely that showing the smallest displacements. Furthermore, it is expected that the upper layer exhibits linear stress-strain behaviour due to the absence of a highly organized fibre network.
The two-layer model performed better in describing the experiments of various aperture diameters with one set of parameters than the single layer model. The estimation procedure resulted in $C_{10,rd} = 0.16$ MPa and $C_{10,ul} = 0.11$ kPa. This large difference in stiffness has to our knowledge not been previously reported. The stiffness for the upper layer as presented in this chapter is much smaller than that of the stratum corneum which ranges from 2000 to 6 MPa for relative humidity increasing from 30% to 100% (Park and Baddiel, 1972). This indicates that in suction experiments with small displacements and at aperture sizes of 1-6 mm as described in this study, the influence of the stiff stratum corneum on the overall mechanical response is negligible.

It appeared that the two-layer model predictions were more accurate for the experiment with the 1 and 6 mm aperture diameter, than for the experiment with 2 mm aperture diameter. To explain this phenomenon and to study the threshold point in the experiments, suction experiments with smaller aperture sizes should be performed. However, at the present time, it is not possible to perform such measurements with the described experimental set-ups due to the limited resolution of the imaging systems. This may be solved by using confocal microscopy, which has the ability to resolve the uppermost layers of the skin. This technique would necessarily involve a reduced aperture diameter and thus the enhanced influence of the stratum corneum would have to be accommodated in a more complex model. Furthermore, the water which is needed as coupling liquid would inevitably hydrate the stratum corneum. This may influence its mechanical response, as the value of the Young's modulus decreases with increase in relative humidity as mentioned above.

In a recent study, Alexopoulos et al. (2003) developed a semi-analytical two-layer model to describe pipette aspiration experiments. The model consisted of an elastic layer of finite thickness h overlying and elastic half-space foundation. The stiffness of the upper layer was calculated with the following equation

$$E_{layer} = C^* \cdot r_i \cdot \frac{\Delta p}{L} \ , \tag{4.4}$$

where Δp is the applied pressure, L is the uplift of the surface and C^* is a constant whose value depends on the stiffness ratio, the dimensionless thickness of the layer h^* (h/r_i) and the pipette wall geometry (ratio of inner and outer diameter r_i/r_o).

The influence of stiffness ratio and dimensionless thickness of the upper layer on the dimensionless stiffness C^* was compared for the two layer FE model (figure 4.6 solid lines) and for Alexopoulos' analytical model assuming incompressibility and $r_i/r_o = 1.5$ (figure 4.6 dashed lines, kindly provided by Alexopoulos). It shows good agreement for small difference in material parameters and large h^*. However, with decreasing h^* (increasing aperture diameter) there is increasing divergence between the model by Alexopoulos, which assumes infinite thickness of the layer beneath the upper layer and the present FE model which has a finite thickness for the reticular dermis. Also for large stiffness ratios a difference was observed.

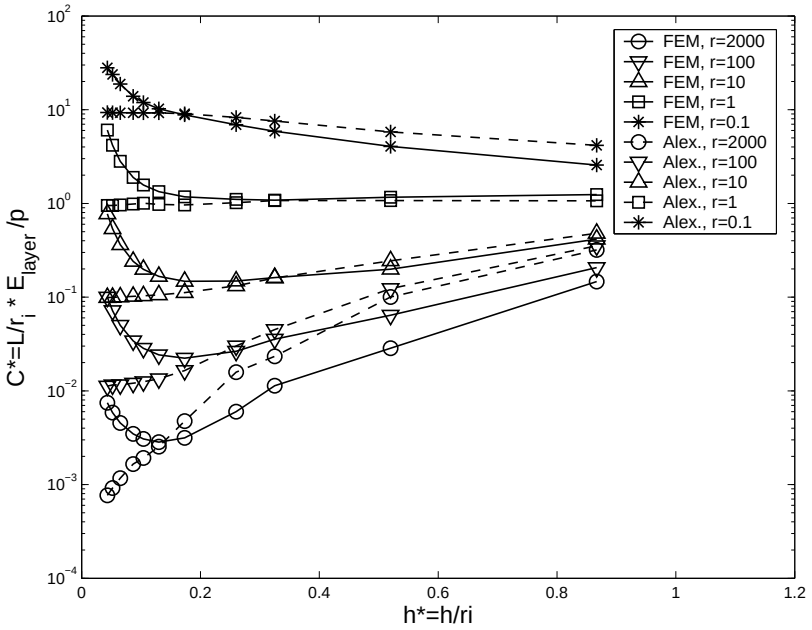

Figure 4.6: *Influence of stiffness ratio ($r = C_{10,rd}/C_{10,ul}$) and dimensionless thickness of the top layer (h^* = thickness upper layer / aperture radius) on the dimensionless stiffness C^* for our model (solid lines) and Alexopoulos' model assuming incompressibility and $r_i/r_o = 1.5$ (dashed lines).*

Thus it appears that for small difference in material parameters and for small aperture sizes Alexopoulos' model is suitable to model the initial part of the experimental data as presented in chapter 3. However, for large aperture diameters the half space assumption as used by Alexopoulos et al. (2003) can no longer be used to model these experiments. Also for large stiffness ratios the analytical model is not suitable to model the present experimental data, probably because the analytical model is not able to describe the large deformations near the aperture wall. Furthermore, the FEM model is capable of describing different boundary conditions, therefore being suitable for a wider range of experiments.

In conclusion it was shown that by combining experiments with different length scales it indeed is possible to separate the mechanical behaviour of distinct layers in the skin. The two-layer model was successful in predicting behaviour in the 1 and 6 mm, but less so for the 2 mm aperture diameter experiments and the material parameter of the reticular dermis was found to be much higher than that of the upper layer.

Chapter 5

In vivo measurement of displacement and strain fields in human epidermis

5.1 Introduction

In the previous chapters, it became clear that the mechanical behaviour of the upper layer of the skin and the deeper reticular dermis are different. The upper layer exhibits a much lower stiffness than the reticular dermis. However, for a number of applications it is important to examine in even more detail when studying the top layers of the skin. For example, in various personal care products the interaction with the 10-20 μm thick stratum corneum is an important consideration. It is well established that the properties of the stratum corneum vary considerably with changes in environmental conditions like humidity and temperature (Park and Baddiel, 1972). However, to be able to measure *in vivo* mechanical properties of the epidermis and the stratum corneum, in particular, an extension of the measurement to a smaller scale is necessary. Unfortunately, OCT and ultrasound do not have sufficient resolution to visualize these layers. Consequently, another imaging technique that allows the visualization of these layers must be incorporated into experiments at smaller scales to evaluate their relative contribution to the total mechanical response. The use of smaller scale experiments increases the influence of the stratum corneum which then requires its accommodation in a more complex model. Accordingly, more information on the displacement and strain fields within the skin layers are also needed.

Confocal laser scanning microscopy enables detailed visualization of the upper layers of the skin as described in chapter 1. It allows the skin to be imaged with approximately 2 μm vertical and 1 μm lateral resolution up to depths of 250 μm.

Displacement and strain fields can be extracted from the resulting digital images by digital image correlation (DIC). Marcellier et al. (2001) applied this technique on two-dimensional images of the skin surface to compute displacement and strain fields. Results demonstrated differences in deformation fields in areas exhibiting stretch marks or scars compared to areas of healthy skin. However, as the skin with its wavy layers is a three-dimensional structure, also three-dimensional image correlation is needed.

The objective of the work described in this chapter was to develop a technique which can be used to quantitatively measure *in vivo* sub-surface deformations in human epidermis subjected to loading. The skin was visualized with three-dimensional confocal images while displacements were applied to the skin surface. In suction experiments, large displacements perpendicular to the skin surface occur. This causes the skin to move out of focus when combined with confocal microscopy. Hence, tension was preferred over suction.
A small tensile device was developed to apply uniaxial tension to the skin and simultaneously measure the resulting forces. The device was coupled to a confocal laser scanning microscope (CLSM) to visualize the skin during the tensile experiment. The three-dimensional reconstructed images of the skin were evaluated with three-dimensional digital image correlation to determine the displacements in the skin. From these displacements a deformation tensor was computed to obtain Green-Lagrange strains. The experimental results were interpreted with a finite element model consisting of the reticular dermis, the combined papillar dermis and living epidermis, and the stratum corneum.

5.2 Subsurface deformation measurements

5.2.1 Materials and methods

A loading device was developed to load the skin surface with tension and measure the applied loads. Digital image correlation was applied to the three-dimensional images of the skin to obtain a three-dimensional displacement field. A gradient deformation formulation was used to compute a strain field from the displacement field.

Experimental Set-up

High-resolution confocal imaging is based on the detection of singly backscattered light from tissue. Image contrast in the skin is mainly due to refractive index variations of tissue structural features and melanin. A modified confocal laser scanning reflectance microscope (VivaScope 1000, Lucid Inc, Henrietta, NY) was used to visualize different skin layers. The microscope was equipped with a piezo focussing unit (PIFOC, Physik Instrumente, Walgborg, Germany) on the objective assembly (figure 5.1), to allow rapid depth scans (Hendriks and Lucassen, 2001).

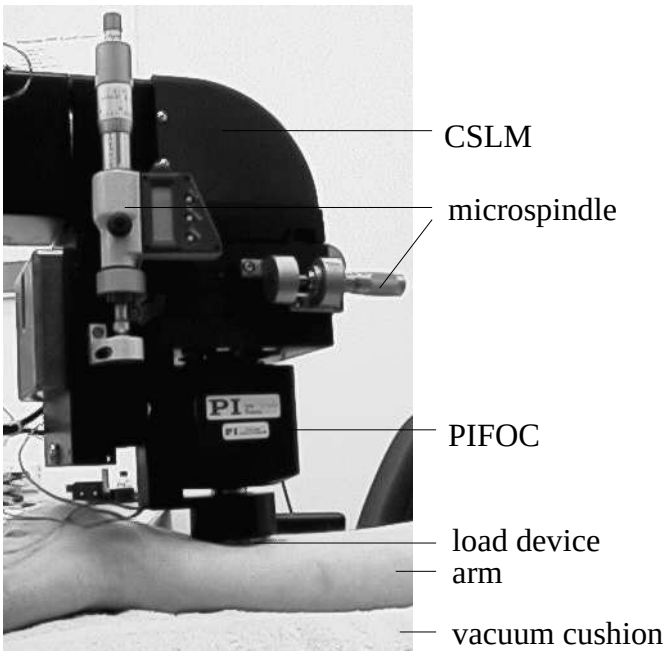

Figure 5.1: *Picture of the load device coupled to the confocal microscope and attached to the volar forearm. Note that arm is not (yet) restrained by the cushion.*

A Leica (Wetzlar, Germany) 20X / 0.5 NA water immersion objective with 3.5 mm working distance was used. Using an illumination wavelength of 834 nm the system achieved 1.5 μm lateral resolution (set by the pixel dimensions), 7 μm axial resolution

(defined by $1.5n\lambda/NA^2$) and approximately 300 μm penetration depth. The system was controlled with LabVIEW software (National Instruments, USA).

A special device that could be coupled to the confocal microscope was developed to apply tension to the skin surface. Figure 5.2 shows the complete tensile device and an enlargement of the confocal ring, which was connected to the confocal microscope. The confocal ring consisted of load pads which could be moved via a cantilever. The frame of the confocal ring was attached to the skin surface with double sided adhesive tape (Lucid adhesive ring). It isolates, limits and levels the area of deformed skin under investigation. The pads were glued to the skin with Loctite 4013 (medical grade, Henkel Technologies, Nieuwegein, the Netherlands) and miniature strain gages (Kyowa KFG-1N-120-C1-11N30C2, Japan) were attached to double leaf springs on both pads (figure 5.3, left) and connected to an amplifier (HBM AB22, Hottinger Baldwin Messtechnik Gmbh, Darmstadt, Germany) to measure forces. The amplifier was connected to a personal computer which used LabVIEW to record the forces.

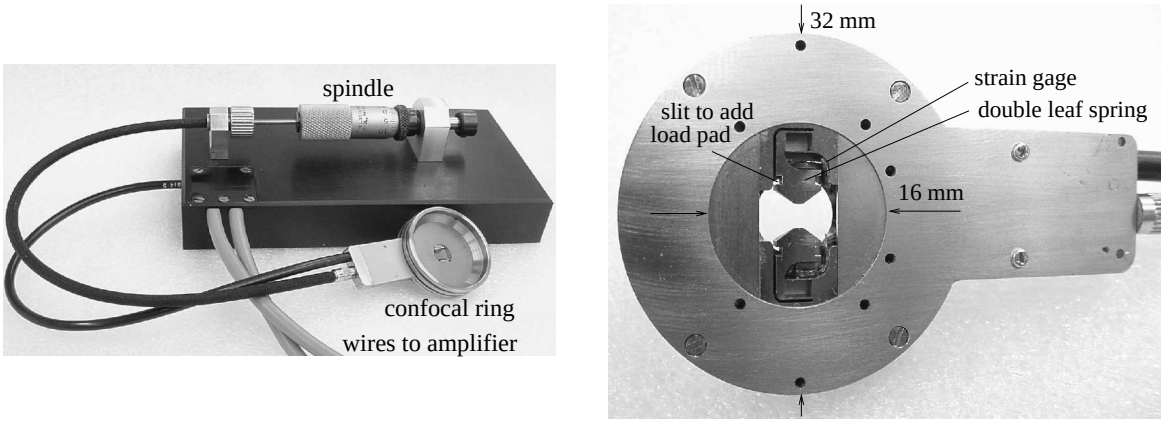

Figure 5.2: *Picture of the tensile device with screw spindle and confocal ring (left) and bottom view of the confocal ring (right). Load pads are not shown in this figure.*

The pads, 3×4 mm^2 in dimensions, were driven in opposite directions by a hand driven screw spindle. The initial distance between the two pads was 2 mm and both pads had a maximum displacement of 0.5 mm. The tensile device was coupled to the microscope and the field of view was located such that in the initial position one of the pads covered approximately one third of the field of view (figure 5.3, right).

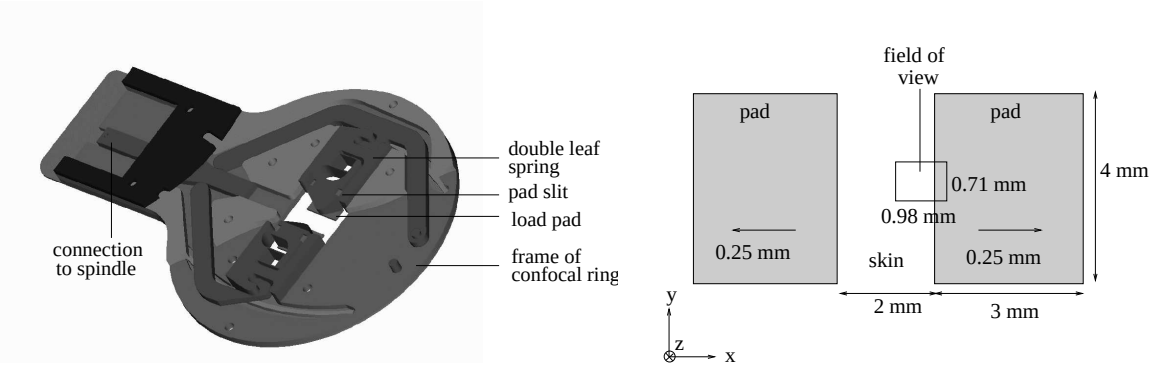

Figure 5.3: *Schematic view of the load mechanism of the confocal ring (left) and dimensions of the load pads and field of view of the microscope (right).*

Calibration of Strain Gages

To calibrate the strain gages, the confocal ring was attached in a handscrew (figure 5.4). A wedge was vertically placed into a slit for the pad on one end, and on the other end a weight was attached. The force was zeroed with no weight attached to the wedge and the strain gage was calibrated with a 20 and a 50 g weight.

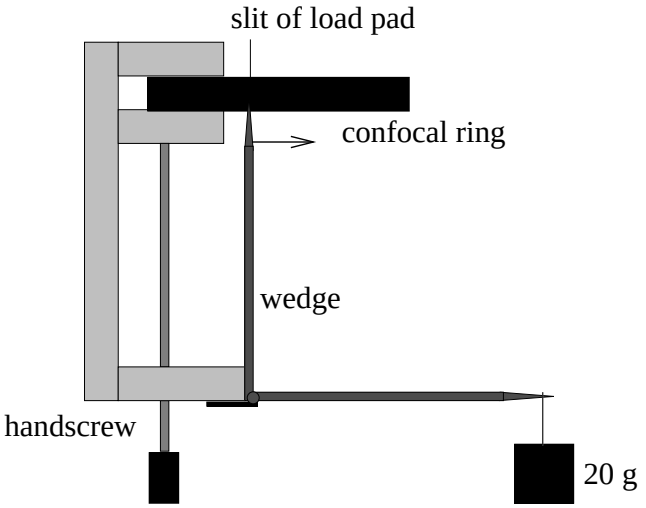

Figure 5.4: *Schematic representation of the calibration of the strain gages. Both arms of the wedge have the same dimensions.*

Experimental Protocol

A tension test was performed on the volar aspect of the left forearm of a 26 year old female. The subject was healthy and seated in an upright position. To limit the movement of the

area under investigation, the arm was positioned within a vacuum cushion covered with a towel to increase comfort and ensure a relaxed unrestrained arm (figure 5.1).

Water is needed as an optical coupling liquid for confocal microscopy. According to Hendriks and Lucassen (2001) swelling due to hydration is complete after 90 minutes and stratum corneum thickness is doubled. To avoid stratum corneum swelling during the experiment due to hydration, skin hydration was limited to one hour prior to testing. Immediately after hydration, the tensile device was attached to the skin, filled with water and coupled to the microscope.

To find the skin surface, the piezo focusser was held at 0 μm, while the stratum corneum was visualized by manually adjusting the position of the lens with a microspindle. First, a three-dimensional image of the initial state of the skin was recorded. Then both pads were moved 0.25 mm in steps of 0.01 mm. After each step, a three-dimensional scan was made, consisting of a stack of 96 two-dimensional images from 10 to 200 μm depth (z) in steps of 2 μm. The point $z = 0$ corresponded with the uppermost surface of the skin, which was visible in the confocal image of the skin in initial state. The two-dimensional images were stored as 636 $\times$ 480 sets of 8 bit numbers corresponding to a field of view of 0.98 mm x 0.71 mm (pixel size was approximately 1.5 $\times$ 1.5 μm^2). During an axial scan of 30 seconds duration, the applied laser power was adjusted for optimum brightness. Near the surface approximately 3% of the maximum laser power of 15 mW was used, whereas 20% of the maximum power was used for the deepest layers. To limit movement of the skin during imaging, the scan was made 30 seconds after load application.

Digital Image Correlation

Digital image correlation is a technique to measure displacement fields by comparing two digitized images and was developed at the University of South Carolina (Sutton et al., 1983). As the technique does not require physical markers on the surface, it is also suitable to calculate displacement fields from images made under a material surface, such as in the skin, where no markers can be placed.

The technique uses the contrast distribution (gray values of pixels) to correlate points between two images and reconstruct the displacement field. Because of large deformations in the experiment, the contrast distribution in the images changes rapidly and only small deformation steps can be accommodated by the correlation technique. Therefore, subsequent images are taken to cover the whole range of displacements in an experiment. The calculated incremental displacements are summed to acquire the total displacements.

The method can be briefly reviewed for the two-dimensional case in figure 5.5, showing an image of the skin in initial position (left) and an image of the same part of the skin after deformation (right). A set of points is chosen for which displacements may be calculated. A window A is defined for each point. A search area S is defined in the deformed situation in which window B, which is related to window A, has to be identified. Window B is found by comparing the contrast distribution for all possible window positions in the search area and finding maximum correlation.

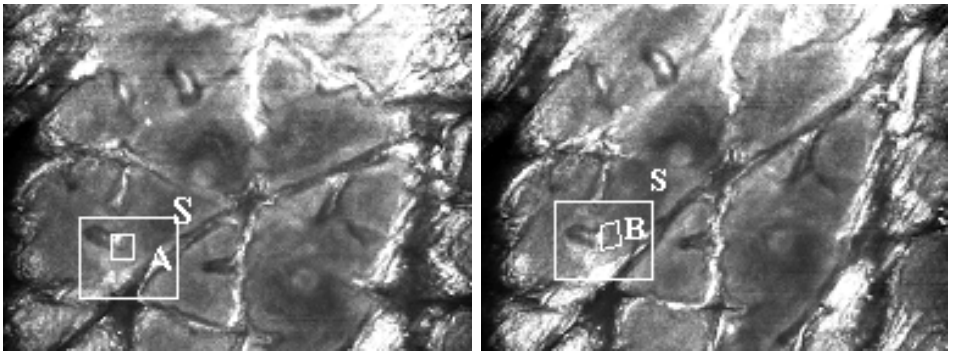

Figure 5.5: *Confocal image of the skin in initial position (left) showing subset A and search area S and after tensile loading (right) showing subset B and search area S.*

Figure 5.6 shows a two-dimensional representation of the deformation of window A from the first to the second image. Let (x', y') denote the position of an arbitrary material point in the second image (deformed situation), which was originally at position (x, y) in the first image (reference position). A window or subset A is defined around (x, y) in the first image where $A(x_i, y_j)$ represents the gray level value in (x_i, y_j). For convenience, this window is chosen to cover a rectangular domain. After deformation, the window is mapped onto a window or subset B in the second image with gray level values $B(x'_i, y'_j)$. The deformation of window A is modelled using the first term of a Taylor expansion:

$$x'_i = x_i + u + \frac{\partial u}{\partial x}\Delta x + \frac{\partial u}{\partial y}\Delta y \ , \tag{5.1}$$

$$y'_j = y_j + v + \frac{\partial v}{\partial x}\Delta x + \frac{\partial v}{\partial y}\Delta y \ , \tag{5.2}$$

where u and v are the displacements in x- and y-direction at (x, y) and $\frac{\partial u}{\partial x}$, $\frac{\partial u}{\partial y}$, $\frac{\partial v}{\partial x}$ and $\frac{\partial v}{\partial y}$ are the displacement gradients at (x, y). The distances Δx and Δy are defined as

$$\Delta x = x_i - x, \tag{5.3}$$

$$\Delta y = y_j - y. \tag{5.4}$$

The position for window B which correlates optimally to window A, is calculated. A correlation function R shows how closely $A(x_i, y_j)$ and $B(x'_i, y'_j)$ are related. For perfect correlation $R = 1$. To find maximum correlation, R' defined as $R' = 1 - R$, is minimized. The discrete form of R' can be written as

$$R' = 1 - R = 1 - \frac{\sum_{i=1}^{N_i}\sum_{j=1}^{N_j} A(x_i, y_j)B(x'_i, y'_j)}{\left[\sum_{i=1}^{N_i}\sum_{j=1}^{N_j} A(x_i, y_j)^2 \sum_{i=1}^{N_i}\sum_{j=1}^{N_j} B(x'_i, y'_j)^2\right]^{\frac{1}{2}}} \ . \tag{5.5}$$

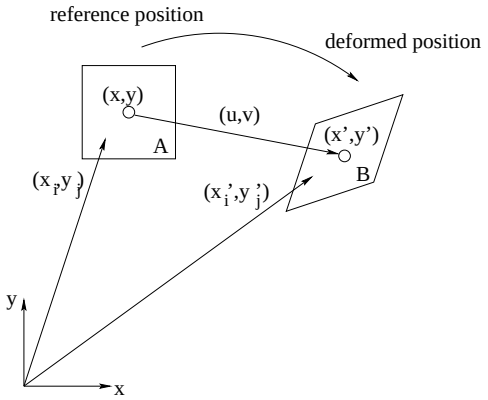

Figure 5.6: *Two-dimensional representation of the deformation of a subset.*

Verhulp et al. (2004) extended the image correlation technique from two dimensions to three dimensions for strain measurements in micro structures such as trabecular bone. For three-dimensional DIC equations 5.1 and 5.2 are substituted by

$$x_i' = x_i + u + \frac{\partial u}{\partial x}\Delta x + \frac{\partial u}{\partial y}\Delta y + \frac{\partial u}{\partial z}\Delta z \tag{5.6}$$

$$y_j' = y_j + v + \frac{\partial v}{\partial x}\Delta x + \frac{\partial v}{\partial y}\Delta y + \frac{\partial v}{\partial z}\Delta z \tag{5.7}$$

$$z_k' = z_k + w + \frac{\partial w}{\partial x}\Delta x + \frac{\partial w}{\partial y}\Delta y + \frac{\partial w}{\partial z}\Delta z \tag{5.8}$$

and the correlation function that needs to be minimized is

$$R' = 1 - R = 1 - \frac{\sum_{i=1}^{N_i}\sum_{j=1}^{N_j}\sum_{k=1}^{N_k} A(x_i, y_j, z_k)B(x_i', y_j', z_k')}{\left[\sum_{i=1}^{N_i}\sum_{j=1}^{N_j}\sum_{k=1}^{N_k} A(x_i, y_j, z_k)^2 \sum_{i=1}^{N_i}\sum_{j=1}^{N_j}\sum_{k=1}^{N_k} B(x_i', y_j', z_k')^2\right]^{\frac{1}{2}}}. \tag{5.9}$$

So R' is a function of twelve variables given by

$$W_{3D} = (u, v, w, \frac{\partial u}{\partial x}, \frac{\partial u}{\partial y}, \frac{\partial u}{\partial z}, \frac{\partial v}{\partial x}, \frac{\partial v}{\partial y}, \frac{\partial v}{\partial z}, \frac{\partial w}{\partial x}, \frac{\partial w}{\partial y}, \frac{\partial w}{\partial z}). \tag{5.10}$$

Image correlation is performed by determining the values of these twelve variables for which the correlation function R' is minimized. To determine R' the gray level values B must be available at positions (x_i', y_j', z_k'). Since the displacements u, v and w and the displacement gradients need not to be integer values, the positions (x_i', y_j', z_k') will generally not coincide with one of the integer values at which the second image is sampled. The gray level values at non-integer values are therefore approximated using bicubic spline interpolation.

The minimum of function R' is determined in two steps. In the first step, the window is assumed to translate without deformation or rotation. Therefore, the displacement gradients are set to zero. A Fast Fourier Transformation (FFT) calculation is used to

determine the correlation functions for all possible window positions in the search area. The minimum is determined which leads to a maximum correlation position with correlation variables u, w and z in pixel resolution.

In the second step, the location of maximum correlation is determined more accurately using an iterative search algorithm. The maximum correlation position at a pixel-level is used as an initial estimate in the BFGS (Broyden-Fletcher-Goldfarb-Shanno) algorithm (Gill et al., 1981) to minimize the correlation function R' at a sub-pixel level. In this calculation the window is allowed to deform linearly and the gray levels are interpolated with bicubic splines to obtain sub-pixel information and determine the displacement gradients.

To find the sub-surface displacements in the skin, digital image correlation was applied to 350 points which were located in the skin. The points were distributed $5 \times 10 \times 7$ in x-, y- and z-direction, respectively (figure 5.7 and appendix 5.5). The window around each point was cubic and set at $11 \times 11 \times 11$ pixels. The size of the search area S is determined by the size of the window and the maximum predicted displacement of the points and is set at $35 \times 35 \times 35$ pixels.

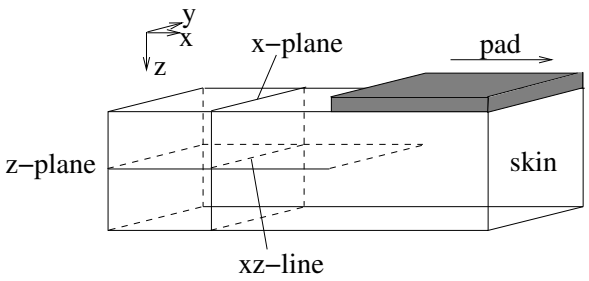

Figure 5.7: *Three-dimensional schematic representation of the skin and the pad showing an arbitrary x- and z-plane. The points are distributed* $5 \times 10 \times 7$ *in x-, y- and z-direction, respectively.*

Strain Fields

To obtain strain information from the experimentally obtained displacement data, a gradient deformation formulation was used, developed by Peters (1987) and improved by Geers et al. (1996). To compute the strains, a deformation tensor must be calculated from the discrete displacement field.

The infinitesimal deformation in a continuum can be described as follows. P_0 and Q_0 represent two neighbouring particles at time $t = 0$. The position vector of P_0 is identified by $\mathbf{x}_0$, while the position vector of Q_0 can be written as $\mathbf{x}_0 + d\mathbf{x}_0$. At time t, after deformation, the two particles move to the points P_t and Q_t identified by $\mathbf{x}_t$ for P_t and $\mathbf{x}_t + d\mathbf{x}_t$ for Q_t (figure 5.8).

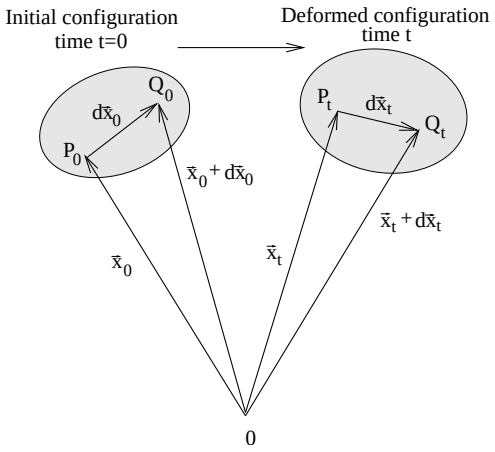

Figure 5.8: *Infinitesimal deformation in the 2D-plane. Adapted from Geers (1996).*

The deformation tensor in P_t at time t is now defined as:

$$d\mathbf{x}_t = \mathbf{F} \cdot d\mathbf{x}_0 \tag{5.11}$$

resulting in

$$\mathbf{F} = (\nabla_0 \mathbf{x}_t)^c = \frac{\partial \mathbf{x}_t}{\partial \mathbf{x}_0} \ . \tag{5.12}$$

Definition 5.11 holds for infinitesimally small $d\mathbf{x}_t$ and $d\mathbf{x}_0$. However, in the experimental situation distances between the marked points are finite $\Delta\mathbf{x}_t$ and $\Delta\mathbf{x}_0$. At a fixed time t the actual position vector $\mathbf{x}_t$ of a point P_t can be considered as a function of the initial position vector $\mathbf{x}_0$. The position vector of a neighbouring point $\mathbf{x}_t + \Delta\mathbf{x}_t$ can be written as a vectorial Taylor-series expansion, truncated after the second-order terms:

$$\Delta\mathbf{x}_t = \frac{\partial \mathbf{x}_t}{\partial \mathbf{x}_0} \cdot \Delta\mathbf{x}_0 + \frac{1}{2}\frac{\partial^2 \mathbf{x}_t}{\partial \mathbf{x}_0^2} : \Delta\mathbf{x}_0\Delta\mathbf{x}_0 + \mathbf{a} \tag{5.13}$$

where $\mathbf{a}$ represents the theoretical discretization (or truncation) error. Equation 5.13 involves the deformation tensor $\mathbf{F} = \partial\mathbf{x}_t/\partial\mathbf{x}_0$ (eqn 5.12) and the gradient deformation tensor $\partial^2\mathbf{x}_t/\partial\mathbf{x}_0^2$ of rank three. With definition

$${}^3\mathbf{G} = \frac{1}{2}\frac{\partial^2 \mathbf{x}_t}{\partial \mathbf{x}_0^2} \ , \tag{5.14}$$

equation 5.13 can be rewritten as

$$\Delta\mathbf{x}_t = \mathbf{F} \cdot \Delta\mathbf{x}_0 + \ {}^3\mathbf{G} : \Delta\mathbf{x}_0\Delta\mathbf{x}_0 + \mathbf{a}. \tag{5.15}$$

To solve the unknowns in equation 5.15, a strain group of k neigbouring particles at the points Q_{t_i} around the central particle P_t is considered (figure 5.9).

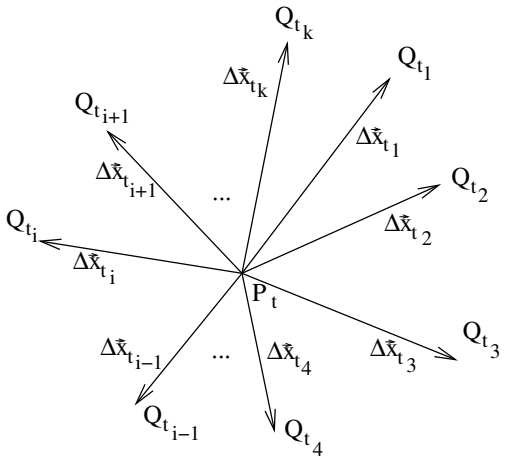

Figure 5.9: *Particle distribution around the central point. Adapted from Geers (1996).*

Equation 5.15 can then be formulated for each point Q_{ti} in the strain group involving a discretization error $\mathbf{a}_i$ for each equation. This discretization error consists of a constant average error, for the group of particles in consideration, a variable error and a measurement error caused by the DIC measurement of the particle positions. The variable error is assumed to be random and normally distributed around the null vector. At least six particles Q_{ti} are required to solve the unknown terms in equation 5.15 and thus to determine an estimation for $\mathbf{F}$ of the central particle P_t. If more than six particles are available, a statistical approach is needed, resulting in an improved approximation for $\mathbf{F}$. Yet, if the distance between the central particle and the surrounding particles becomes large, the discretization error rises significantly and will adversely influence the results.

Peters (1987) developed a linear method where the Taylor series was truncated after the first term. The method described in this section is a second order method with truncation after the second term developed by Geers et al. (1996). Geers compared the performance of both methods for a number of test cases. While giving good results for slowly varying strain fields, the linear model is sensitive to the spatial particle distribution in a strain group, and can not produce reliable results close to the edges nor at the centre of inhomogeneous strain fields. Using the second order approach of the gradient deformation model, strains at the edges and even in the central area of the strain field are much more accurate. However, if the local gradient becomes too strong, a second-order scheme may be insufficient and the discretization must be refined.

When measurement errors in the displacement data are taken into account, larger strain groups should be used. In this case, the superiority of the second-order approach diminishes somewhat, especially for slow varying strain distributions. However, for cases with high strain gradients, such as would be expected in the case of loading non-homogeneous skin, the use of the second-order approach is clearly advantageous.
Another advantage of the second-order approach is that all particles can be taken into account for the strain computation. Errors at edges and corners have approximately

the same error magnitude as in the centre of the field, and, as a consequence, strain distributions around internal boundaries such as inhomogeneities in the skin can be determined much more accurately.

The deformation tensor was estimated in each data point from the 3D-displacement field (central particle) with a least squares fit through k neighbouring particles of the displacement field. These neighbouring points were found in an ellipsoid around the central point. The radii of the ellipsoid (the estimation radius) were chosen at 3 times the spacing between two nearest surrounding points for every direction in initial state. If this number of k neighbouring points was smaller than 35, the nearest 35 points were chosen.

When the deformation tensor $\mathbf{F}$ is known, the Green-Lagrange strain tensor $\mathbf{E}$ can be derived by

$$\mathbf{E} = \frac{1}{2}(\mathbf{F}^c \cdot \mathbf{F} - \mathbf{I}), \tag{5.16}$$

where $\mathbf{I}$ is the unit tensor.

5.2.2 Results

A typical example of two-dimensional images of the skin (xy-plane) at approximately the same depth for the initial state (figure 5.10, left), after 0.1 mm (middle) and after 0.2 mm pad displacement (right) shows the pad (represented by the black area in the right of

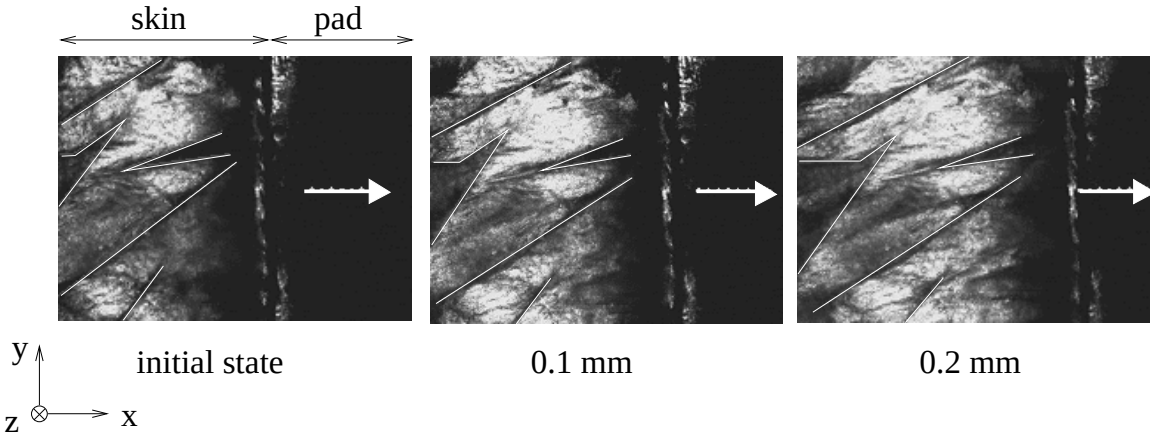

Figure 5.10: *Two-dimensional confocal images of the skin at approximately the same depth for initial state (left), after 0.1 mm pad displacement (middle) and 0.2 mm pad displacement (right).*

the images) moving to the right and the deformation of the skin which is visible from the changing wrinkle orientation (represented by lines in the figure). It also shows different skin layers in one image (at one depth): high intensity stratum corneum and dark cells

in the stratum spinosum. In addition, the figure reveals that the skin is elevated due to loading: the deformed state shows more stratum corneum than the initial state.

Figure 5.11 illustrates a calculated displacement field in confocal images at depths of 10 and 25 μm under the skin surface. The images were acquired during a shear test with a similar experimental setup. For this experiment with 0.6 $\times$ 0.4 mm^2 field of view, a 40X / 0.8 NA objective lens was used. Two-dimensional movies were made during the deformation at various depths in the skin and 63 points were followed using digital image correlation. The image shows the trajectories of the points during the deformation.
To test the performance of the digital image correlation, 50 images were made of the load pad of this set-up during a displacement of 0.5 mm corresponding to 538 pixels. Digital image correlation resulted in a displacement of 530 pixels corresponding to 0.49 mm pad displacement.

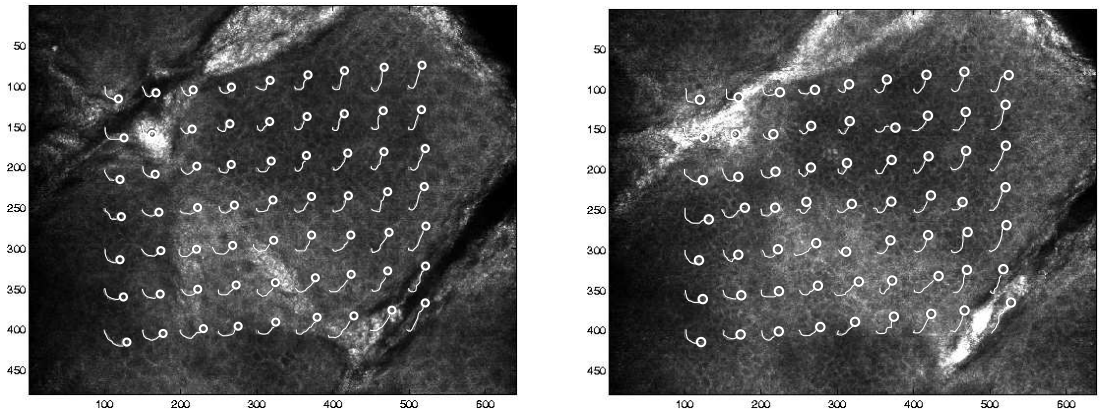

10 μm depth 25 μm depth

Figure 5.11: *Calculated displacements at different depths under the skin surface during shear loading. Circles represent the final position of a point and the lines represent the followed track. The pad left of the images was moved downwards, the pad right of the images was moved upwards. Pixel numbers are shown along the axes. Image size is 0.6 $\times$ 0.4 mm.*

Digital Image Correlation

Figure 5.7 in section 5.2.1 showed a schematic representation of the skin in the field of view. Two planes show how the points were grouped to present the results. For each x- and z-plane the results of all points which lay initially in that plane, were averaged.

Due to some initial backlash in the tensile device, probably caused by friction in the loading device, the total displacement of the pad was approximately 0.2 mm as opposed to the prescribed 0.25 mm and the first three load steps were not considered. Due to limited contrast, for example in wrinkles and in the stratum corneum, only 113 of the 350 points were accurately followed with the digital image correlation during the entire experiment. Those points were mainly located in the deeper skin layers (appendix 5.5).

Figure 5.12 shows the z-coordinate (depth) and the total x-displacement after each load step for points that started at the same depth (z-plane). Displacements were averaged for all points in a plane. Each curve represents one z-plane (one depth), each data point on a curve a load step. Also the curve representing the pad is shown. The x-displacement of the pad was larger than that of the different z-planes in every load step. Furthermore, the total x-displacement decreased with increasing depth. However, in the most superficial z-plane (at 0.04 mm depth), the total x-displacement was smallest. This is an artifact. Only a few points (4 of 50) in this plane could be followed with the DIC, and they were located far from the pad, hence showing small displacements. The negative x-displacements in the figure that were obtained for the pad and the points at all depths, could be caused by subtle movements of the subject or by an artifact.

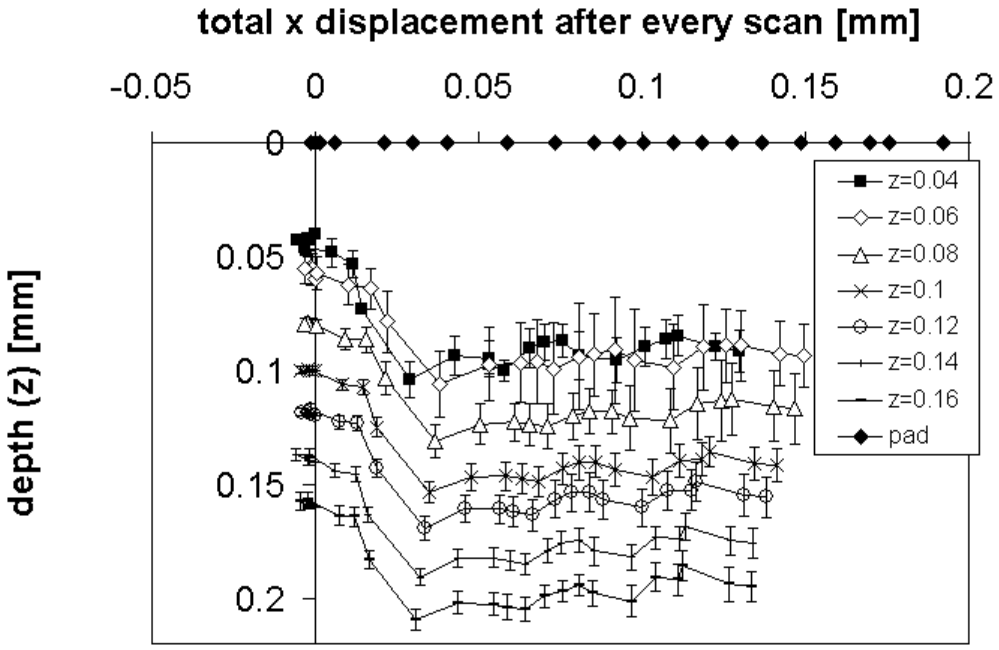

Figure 5.12: *Total x-displacement and z-coordinate after every load step of points from different z-planes (different depths). The symbols in each line represent the load steps.*

The figure also shows standard deviations in z-displacement which decreased with increasing depth. Finally, it shows a large z-displacement for all curves in the 8^{th} and 9^{th} load step (at approximately 0.02 - 0.03 mm x-displacement), probably caused by movement of the subject.

Figure 5.13 shows the total x-displacement after each load step for points at the same initial distance from the pad (x-plane). Again each data point on a curve represents a load step and the curve representing the pad is shown. The figure shows decreasing x-displacements with increasing distance from the pad. Again large displacements appear for the 8^{th} and 9^{th} load step.

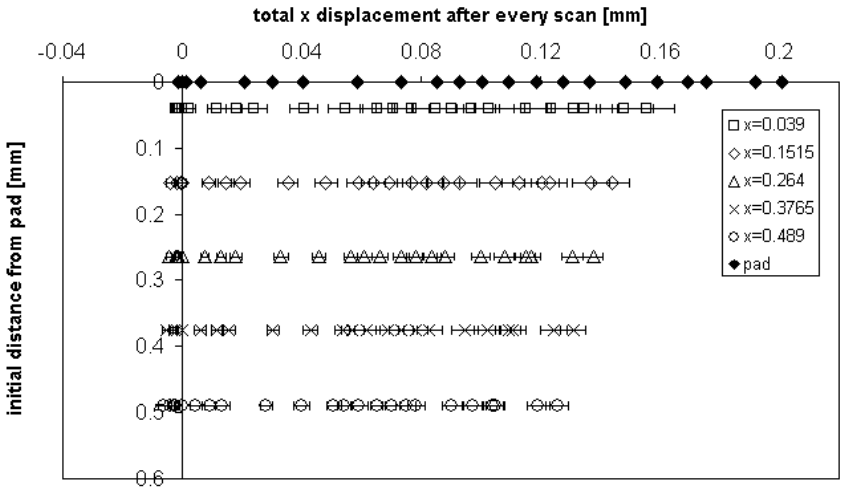

Figure 5.13: *Total x-displacement after every load step of points from different x-planes (different distance from the load pad). The symbols in each line represent the load steps.*

Forces

Figure 5.14 shows the force measured on the pad which was in the field of view during the experiment. During the first steps, the force increased to 0.02 N, with minimal change in displacement. This may be caused by friction in the loading device.
As soon as the pads move, the increase in the force was approximately linear up to a force of approximately 0.1 N.

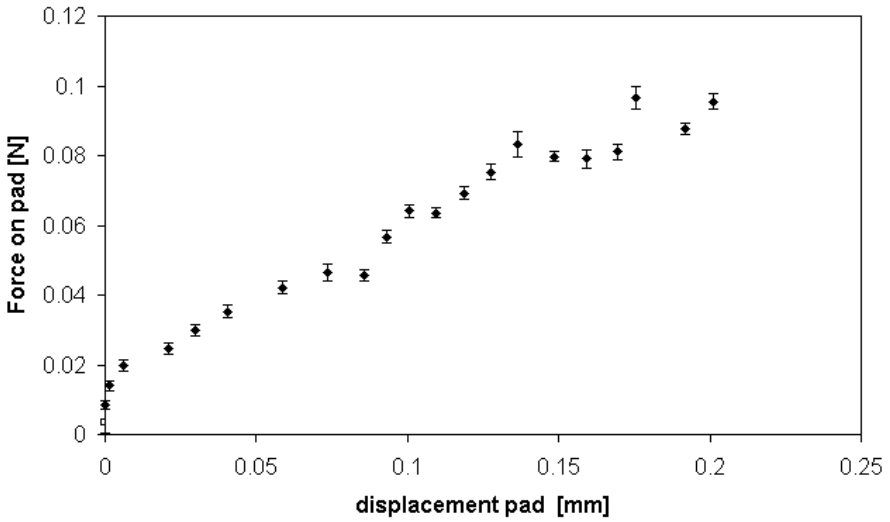

Figure 5.14: *Force on the pad versus pad displacement for all load steps.*

Strains

Figure 5.15 shows Green-Lagrange strains for different directions after a pad displacement of 0.2 mm. The left set of images shows strains averaged for points in different z-planes, whereas the right images show strains averaged for points in different x-planes.

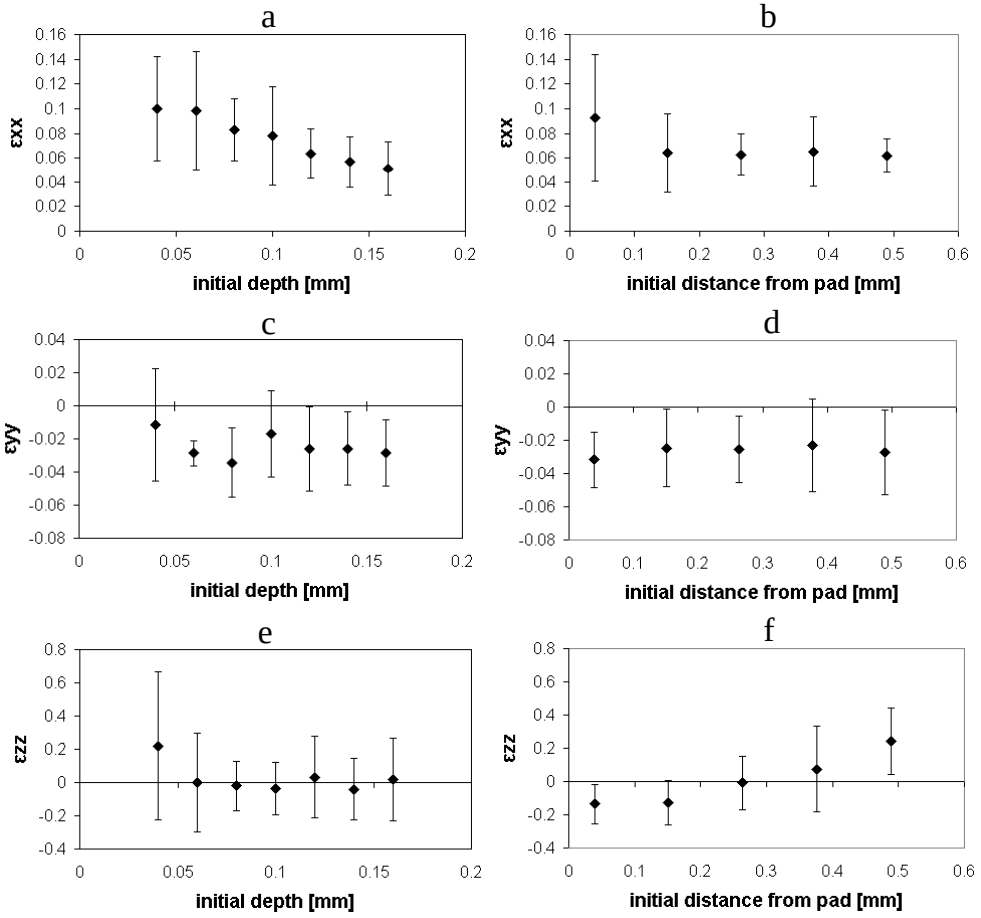

Figure 5.15: *Green Lagrange strains for x-, y- and z-direction after 2 mm pad displacement calculated for points at equal initial depth (z-planes, left) and points equal initial distance from the pad (x-planes, right).*

The figure shows a non-significant decrease for ε_{xx} with increasing depth (a). For all depths, ε_{xx} was significantly larger than ε_{yy}, which showed negative mean values indicating compression (a and c). For both ε_{yy} and ε_{zz} no clear effect of depth was evident (c and e). The mean values of ε_{zz} fluctuated around zero and at each depth both negative and positive ε_{zz} were calculated (e).

Increasing distance from the pad did not influence ε_{xx} and ε_{yy} (b and d). Again ε_{xx} was significantly larger than ε_{yy} (b and d). A non-significant increase was found for ε_{zz} with increasing distance from the pad with compression in z-direction close to the pad and extension in z-direction further from the load pad (f).

5.3 Finite element model

A finite element model was developed in MSC.MARC (MSC Software Corporation, 2001) to describe the tensile experimental results, while not attempting to characterize the mechanical behaviour of the different skin layers. The model consisted of three layers, the stratum corneum, the combined living epidermis and papillar dermis layer and the reticular dermis with thicknesses of 0.015, 0.3 and 1.0 mm, respectively (figure 5.16). As in the previous chapters, the skin was assumed to be incompressible, homogeneous and isotropic and time-dependence was ignored. Due to geometrical symmetry, only a quarter of the area under the tensile device was modelled. The width of the skin was 8 mm, which corresponded to the inner radius of the tensile device.

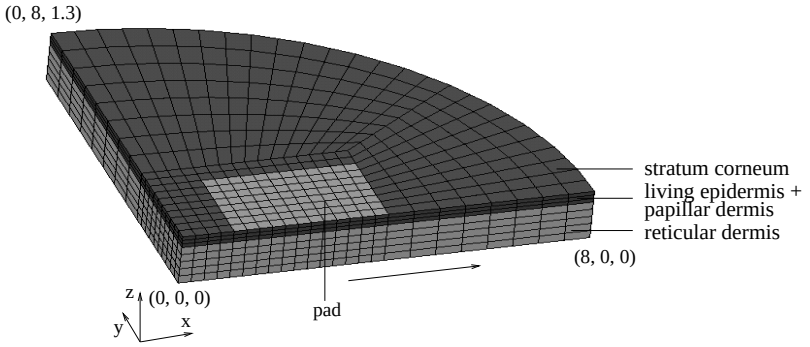

Figure 5.16: *Finite element mesh for the tensile experiment showing stratum corneum, combined living epidermis and papillar dermis and reticular dermis. Coordinates (x,y,z) are given in mm. Note that z=0 corresponds to the bottom of the dermis whereas in the experiment z=0 corresponds with the skin surface.*

The strain energy function that was used to model the reticular dermis and the combined living epidermis and papillar dermis was the same as in the previous chapters and is given by

$$W = C_{10}(\mathbf{I}_1 - 3) + C_{11}(\mathbf{I}_1 - 3)(\mathbf{I}_2 - 3). \tag{5.17}$$

Initially, it was chosen to use material parameters available from the literature as an input for the model. The parameters for the reticular dermis were based on these found in chapter 2 (age of the subject in the experiment described in this chapter is close to that of the subjects aged 19-24 in chapter 2): $C_{10,rd} = 9.4$ kPa, $C_{11,rd} = 82$ kPa. For the epidermis no values are available in the literature. As the mechanical behaviour of the epidermis is assumed to be dominated by the cells in this layer, it was assumed to exhibit a linear stress-strain relationship and $C_{10,ul}$ was set to 9.4 kPa for the combined living epidermis and papillar dermis.
The stratum corneum was modelled with membrane elements and has therefore no physical thickness in the model. Furthermore, only Hookean material behaviour can be modelled with membrane elements in MSC.MARC. The stratum corneum was assumed to behave

as a linear elastic membrane with a Young's modulus and Poisson's ratio set at 6 MPa, respectively, based on the work by Park and Baddiel (1972) who tested stratum corneum at 25° Celcius in 100% relative humidity.

The skin surface under the frame of the confocal ring was restrained in all directions. The skin surface under the pad was restrained in y- and z-direction and was subjected to a prescribed x-displacement of 20 $\times$ 0.025 mm. The fat-reticular dermis interface was left unconstrained.

5.3.1 Results

Figure 5.17 shows experimentally and numerically obtained force-displacement curves. The forces of the experimental study were corrected for the friction force. A second experiment with larger pad displacements, showing a non-linear force-displacement relationship, was performed and used as a reference for the model.
It appeared that with the initial parameters, the model led to higher forces than measured in the experiment. Furthermore, a model consisting of merely stratum corneum (not shown) resulted in forces that were higher than in the experiment. Therefore, the stratum corneum stiffness was decreased by a factor of 10 to 0.6 MPa and a non-linear component was added for the epidermis (C_{11} = 82 kPa) to describe the non-linear force-displacement curve correctly.

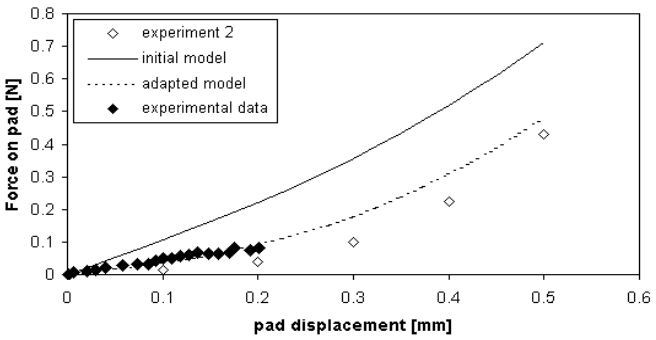

	inital model	adapted model
reticular dermis	$C_{10,rd}$= 9.4 kPa $C_{11,rd}$= 82 kPa	$C_{10,rd}$= 9.4 kPa $C_{11,rd}$= 82 kPa
ed+pd	$C_{10,ul}$= 9.4 kPa	$C_{10,ul}$= 9.4 kPa $C_{11,ul}$= 82 kPa
stratum corneum	E_{sc}= 6 MPa	E_{sc}= 0.6 MPa

Figure 5.17: *Left: Force-pad-displacement curves for the experiment (corrected for friction), the pilot study, the model with initial material parameters and the model with adapted material parameters. Right: table with material parameters for the initial and adapted model (ed+pd = living epidermis and papillar dermis)*

The model with the adapted material parameters was used to compare displacements and strains in the field of view with these obtained by digital image correlation. It appeared that the displacements in the model were smaller than in the experiment. In the plane $y = 0$, the displacements calculated by the model ranged from 0.08 to 0.2 mm, whereas they ranged from 0.12 to 0.15 mm in the experiment. However, strains in the x-direction (ε_{xx}) were overestimated by the model and ranged from 0.13 to 0.24 compared to the range of 0.03 to 0.15 measured (figure 5.15 a and b).

5.4 Discussion

A load device was developed to apply tension to the skin surface. The device was coupled to a confocal microscope to visualize subsurface deformations. Three-dimensional digital image correlation was successfully applied to calculate displacement and strain fields from the 3D-images up to 160 μm under the skin surface. Forces were measured and a finite element model was developed to interpret the experimental results.

The skin showed a clear wavy or 'mountain and valley' structure with wrinkles up to 160 μm depth leading to different skin layers in a two-dimensional confocal image parallel to the skin structure. This effect was larger than in conventional confocal images of the skin, where a glass slide is used to level the skin. Therefore, the use of 3D-images and 3D-digital image correlation should be preferred over 2D-image correlation, although this analysis is much more time consuming.

The performance of the digital image correlation was shown to be good at merely 1.5% deviation by comparing pad displacement acquired manually from the images and that calculated by the DIC. This deviation would be expected to be less than the artifacts associated with the movements of the subject. However, in the skin only one third of the points were correctly traced. Indeed in regions with poor contrast, such as at the skin surface, near the load pad and in wrinkles, few points could be traced with the DIC.

Decreasing window size caused decreasing calculation times, but also large deviations in displacements, as correlation with a window in the deformed image was no longer unique. Increasing window size led to larger calculation times and ultimately no correlation. Variation in search area was of less influence, given that the window in the deformed state was located in the search area. Increase in search area inevitably increased calculation times.

Displacement data were averaged for planes parallel to the skin surface and at equal distance from the pad. As a consequence, the pad displacement and the maximum displacement of the skin, as shown in figure 5.12, differed considerably. A second explanation for this difference can be the unwrinkling of the folds and wrinkles in the skin surface. Furthermore, displacements decreased with increasing depth and with increasing distance from the pad, as expected.

Strains in the pad direction (ε_{xx}) decreased with increasing depth. Due to the 'mountain and valley' structure of the skin, it was difficult to compare points in the same skin layer. As a consequence, it was not possible to make a statement about differences in strains for the various skin layers.

Comparison of the linear and quadratic method, which was used to compute the deformation tensor, showed that for both methods an increasing number of points in the strain group led to smaller standard deviations for the strains in a x- or z-plane (such as the data presented in figure 5.15). Thus, increasing the number of points in a strain group, resulted in both an improved approximation of $\mathbf{F}$, and a smoothing of the strains.
The range of mean values and the standard deviation for strains was larger for the quadratic method than the linear method, which was not able to describe the large strain gradients which were evident during the experiment.

A finite element model was developed to interpret the experimental results. Material parameters from the literature were adapted manually, such that there was general agreement between the numerically and experimentally produced force-displacement curves. It appeared that a smaller Young's modulus was required to be assigned to the stratum corneum and that a non-linear component was needed for the combined living epidermis and papillar dermis. Because of the wrinkled skin surface, the stratum corneum is not loaded until most wrinkles are stretched.
Comparison of the experimental and numerical results showed larger displacements and smaller strains in the experiment. The wrinkles in the surface cause large translations rather than deformation of the individual tissue. So it appears that the wrinkles, with depths up to 160 μm, influence the deformation of the skin considerably.

In conclusion, a new technique was described to visualize and quantify the mechanical response of the uppermost skin layers. The developed technique combined a tension experiment with confocal microscopy and digital image correlation and it proved to be successful in measuring displacement and strain fields under the skin surface. However, it appeared that especially in regions with poor contrast, few points could be traced with the DIC. In addition, it became clear that at this scale the inhomogeneity in the geometry and the material properties of the skin largely affects the displacement and the strain fields.

A few problems should be encountered to be able to use this technique in a numerical-experimental method to identify the mechanical behaviour of the top layers of the skin, including the stratum corneum. For example, to increase the number of points that are traced correctly with DIC, a denser point distribution can be combined with a "smart" distribution by avoiding points in regions with poor contrast. In addition, the accuracy of the DIC should be examined more thoroughly for various depths in the skin. Secondly, all skin between the load pads should be visualized with sufficient resolution to obtain appropriate displacement and strain fields for the model. Thirdly, sensitivity studies with the finite element model showed that the influence of the stratum corneum stiffness was of the same order as that of the deeper layers. Therefore, the initial distance between the pads should be decreased to increase the contribution of the uppermost layers to the total mechanical response. However, with decreasing distance, the attachment of the pads (by glue) becomes more critical. Decrease of experimental length scale also necessitates the geometric inhomogeneity of the skin to be reflected in the model. Furthermore, if the non-linear behaviour is to be characterized, larger displacements are required. This enhances experiments of longer time periods, with increasing risk of movement artifacts by the subject. Finally, to obtain reliable data, tests should be performed on more subjects and subject specific models have to be developed.

5.5 Appendix: Point distribution for DIC and confocal images at various depths

The dimensions of the scans made by the confocal microscope in pixels are 636×480×96 corresponding to 0.98×0.71×0.19 mm. The point distribution that is used for the digital image correlation is shown in table 5.1. The x-value represents the distance from the pad. The z-value represents the depth under the skin surface. Confocal images at those depths in initial position are shown in figure 5.18.
The point distribution in the x- and z-planes prior to and after digital image correlation is shown in table 5.2 and 5.3.

Table 5.1: Point distribution in pixels used for digital image correlation.

direction	start pixel	end pixel	step size	number of points
x	25	325	75	5
y	10	460	50	10
z	20	80	10	7

Table 5.2: Point distribution (in mm) prior to digital image correlation.

	$x = 0.039$	$x = 0.1515$	$x = 0.2640$	$x = 0.3765$	$x = 0.4890$	total
$z = 0.04$	10	10	10	10	10	50
$z = 0.06$	10	10	10	10	10	50
$z = 0.08$	10	10	10	10	10	50
$z = 0.10$	10	10	10	10	10	50
$z = 0.12$	10	10	10	10	10	50
$z = 0.14$	10	10	10	10	10	50
$z = 0.16$	10	10	10	10	10	50
total	70	70	70	70	70	350

Table 5.3: Point distribution (in mm) after digital image correlation.

	$x = 0.039$	$x = 0.1515$	$x = 0.2640$	$x = 0.3765$	$x = 0.4890$	total
$z = 0.04$	-	1	1	2	-	4
$z = 0.06$	3	-	-	1	-	4
$z = 0.08$	6	4	1	2	-	13
$z = 0.10$	3	8	5	4	-	20
$z = 0.12$	1	7	8	5	3	24
$z = 0.14$	-	5	8	7	5	25
$z = 0.16$	-	3	5	9	6	23
total	13	28	28	30	14	113

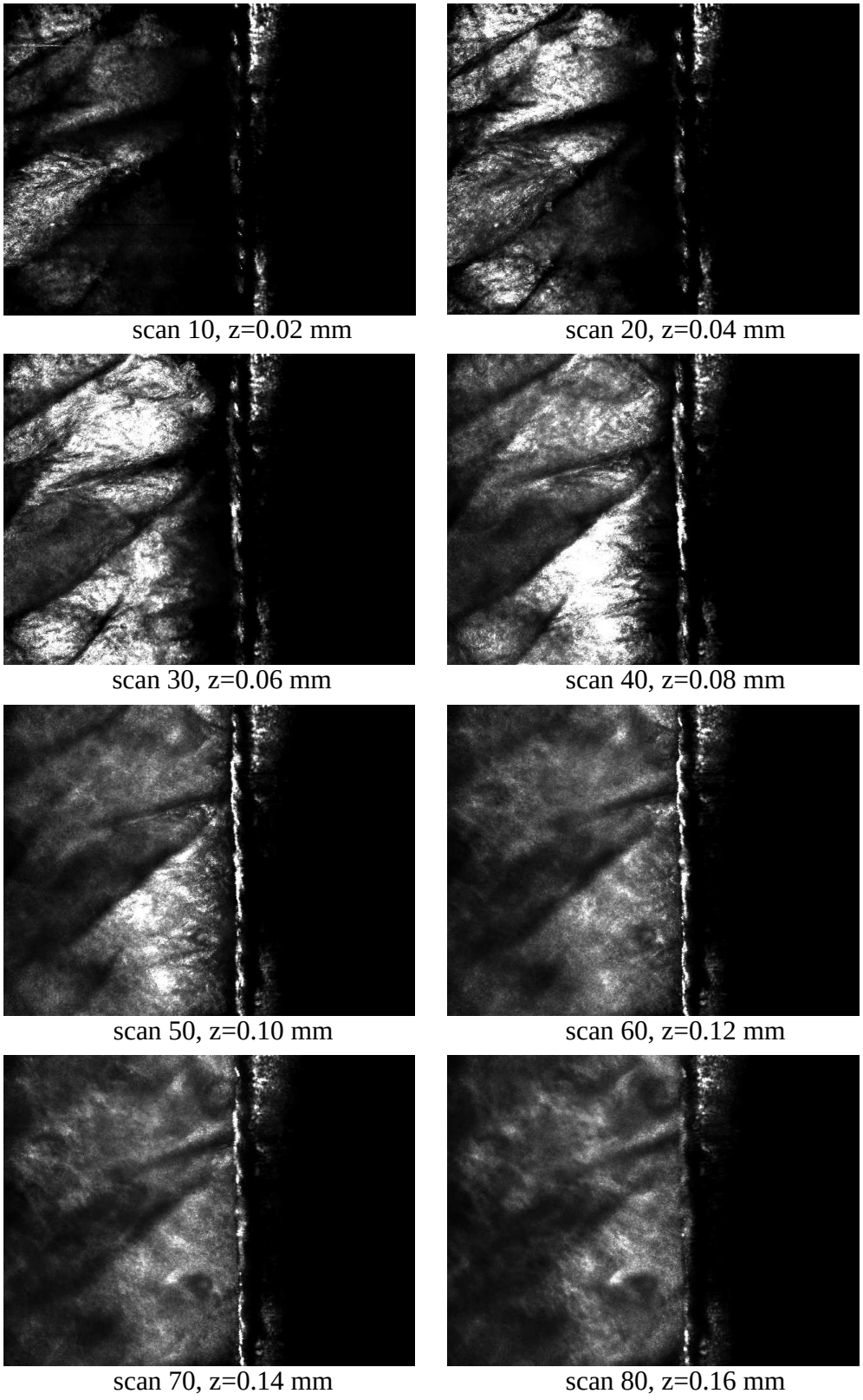

Figure 5.18: *Confocal images of the skin in initial state at various depths under the skin surface (z-planes). The load pad is visible in the right part of the images.*

Chapter 6

General Discussion

6.1 Introductory remarks

The mechanical behaviour of human skin has been the focus of research for more than 100 years. Indeed in the nineteenth century, Langer (1861) examined skin mechanics with particular reference to the orientation of its structural components. From the 1960's onwards when tissue biomechanics became a major research area, skin was often examined, not least because of its easy accessibility. Later, research was focussed on inter- and intra-individual differences, skin ageing and the effects of cosmetic treatments and skin diseases on skin mechanics. The wide availability of computers and new visualization techniques enabled new innovative research on skin biomechanics to continue.
A common feature of many of the reported studies, is that the contribution of the top layers of the skin is ignored (Wilkes et al., 1973; Marks, 1991), although this top layer has an important contribution to many clinical and cosmetic applications.

The original aim of this thesis was to examine the biomechanics of different layers of the human skin *in vivo*, including the top layers. The motivation for this was that the interaction of the top layer with personal care products is important and that the properties of this layer are believed to be influenced by environmental conditions (Park and Baddiel, 1972). The same is true for studies on the aetiology of pressure ulcers where environmental influences like humidity and temperature primarily affect the top layers. Because of these environmental influences *in vivo* experiments with human individuals, which are practically convenient with skin, were preferred over *in vitro* studies. However, the choice for *in vivo* measurements on human subjects was limited to a number of available options. For example, the experiments had to be non-invasive and could not exceed 2 hours to minimize the effort and acceptability by the subject. Furthermore, the experimental protocol had to be reproducible.

The present work was based on the hypothesis that a combination of experiments of different length scales can be used to reveal the mechanical behaviour of different skin layers. To achieve this aim, available visualization techniques, procedures for mechanical testing and digital image correlation were combined and modified to characterize the mechanical behaviour of several skin layers. Indeed three loading devices were developed. The first produced was a suction device with a 6 mm diameter aperture attached to a 20 MHz ultrasound system (chapter 2). It was used to examine the material behaviour of the skin composite, combining both dermis and epidermis. The second device was a suction device with 1, 2 and 6 mm diameter apertures connected to an optical coherence tomography system to study the contribution of the upper skin layers to the mechanical response of the skin (chapters 3 and 4). The third device incorporated tensile loading coupled to a confocal microscope (chapter 5). Digital image correlation was used to extract deformation and strain fields from the images of the confocal microscope. Furthermore, various finite element models were developed to describe the individual experiments.

The present chapter summarizes the overall conclusions that can be drawn from the described studies, and discusses the developed experimental and numerical analyses and its associated results. Finally, some recommendations and future perspectives on research on skin mechanics are proposed.

6.2 General conclusions

The aims as defined in section 1.4 were partially fulfilled namely:

- Suction experiments at various aperture sizes can indeed be successfully used to identify the mechanical behaviour of different skin layers *in vivo*.
- The suction device coupled to the ultrasound system enabled visualization of the deformation of the skin surface, the dermis-subcutaneous fat interface and, in some cases, the fat-muscle interface. The mechanical behaviour of the skin composite was characterized by comparing the experimentally derived pressure versus skin surface displacement curves with the numerical models. This approach provided a clear improvement to presentation of merely pressure versus skin displacement curves produced by the echo-rheometer described by Diridollou et al. (1998) and the results of the analytical model describing those curves presented in Diridollou et al. (2000).
- It was shown that the quasi-static stress-strain relationship of the skin composite in suction can be successfully described by an extended Mooney constitutive equation consisting of two material parameters, C_{10} and C_{11}.
- A new device using an optical coherence tomography system was introduced to visualize the deformation of the skin surface and the interface between the upper layer and the reticular dermis. It combined 1, 2 and 6 mm aperture suction experiments, which each revealed distinct characteristics.
- The response of the upper layer of the skin (epidermis and papillar dermis) and the reticular dermis were separated by combining experimental results from the OCT device with suction measurements at various aperture diameters and a two layer finite element model. It was shown that the reticular dermis is much stiffer than the upper layer, although this result was explored for only a single individual.
- Due to the limited resolution of the OCT system, the experimental length scale could not be decreased and consequently, the mechanical behaviour of the stratum corneum could not be characterized.
- The tensile device coupled to the confocal microscope, in conjunction with three-dimensional digital image correlation, allowed the measurement of three-dimensional deformation and strain fields in the epidermis and papillar dermis. However, it has not yet been employed to characterize the mechanical response of the top layers of the skin.

6.3 Ultrasound and suction

Suction techniques have been widely used to study skin mechanics (for example Barel et al. (1995); Gniadecka and Serup (1995)) and suction devices such as the Cutometer and the Dermaflex, are commercially available. These devices only measure the maximum displacement of the skin surface and often it is not specified whether the skin is restrained to the device. Moreover, the tape rings that accompany such commercial devices are only available with an aperture larger than the maximum aperture of the suction device. In addition, concentric application of the tape to the device is difficult.

The suction method has been recently improved by Diridollou et al. (1998), who developed the *echo-rheometer* combining a suction device with an ultrasound system to examine the contributions of the dermis and the fat layer to the total mechanical response. They used an analytical model assuming the skin to be an isotropic elastic thick membrane (Diridollou et al., 2000) to obtain Young's moduli in the order of 150 kPa.

In the present study, the echo-rheometer was improved by using dedicated double-sided adhesive tape rings ensuring clear boundary conditions by the use of an aperture equal and concentric to that of the suction device. Suction pressure was applied through a 6 mm diameter aperture and the intensity peaks caused by the skin surface and the dermis-fat interface in the ultrasound images were located automatically. From these locations, skin surface displacements and skin composite thickness were obtained. A large portion of the deformation occurred in the subcutaneous fat, which was in agreement with findings by Diridollou et al. (1998). Also the resulting pressure-skin surface displacement curves were of similar form to those of Diridollou et al. (2000). However, the changes in thickness of the skin composite due to loading were the same order of magnitude to the imaging systems and thus not resolvable. Finally, the developed experimental system was suited to future dynamic high-frequency measurements as the system that was used to apply the suction pressure is fully hydraulic.

Dedicated finite element models were developed to describe the experimental data. The advantage of finite element models over analytical models, such as that by Diridollou et al. (2000), is that the former are able to describe larger displacements, more complex constitutive equations for the material behaviour and are suitable for a wider range of experiments with various aperture sizes and boundary conditions. Finally, they allow material parameters to be compared, rather than pressure-displacement curves, which are dependent upon skin thickness and experimental setup. The mechanical behaviour of the skin composite was characterized using a single-layer finite element model. An extended Mooney constitutive equation using two material parameters proved to be adequate to describe the non-linear stress-strain relationship of the skin with $C_{10} = 9.4 \pm 3.6$ kPa for the linear part of the stress-strain relationship and $C_{11} = 82 \pm 60$ kPa for the non-linear part of the stress-strain relationship.

When using finite element models consisting of a fat layer and a skin composite layer, it appeared that the difference in the material parameters for those layers was so large, that numerical stability problems arose. Due to this large difference, the material identification procedure was relatively insensitive to changes in the stiffness of fat and accordingly only

a maximum value for the stiffness of fat, $C_{10,fat} = 0.02$ kPa, was obtained.
There are several options to obtain the material parameters for fat. The first is to increase the numerical stability, which could be achieved by remeshing the model during the simulation. However, in that case, some adaptations are needed to facilitate the parameter identification. Furthermore, remeshing is time consuming in combination with parameter identification. A second method to characterize the mechanical behaviour of fat would be to insert water into the device, thereby causing compression of the fat. The numerical stability for this kind of simulation could be expected to be improved compared to that for the suction experiments. Also visualization of the deformation in the fat layer by, for example MRI, may be more fruitful. However at present, there is no device commercially available to visualize fat with appropriate resolution.

Recently, Gennisson et al. (2004) have been able to obtain the mechanical properties of the skin composite and the fat of the forearm using transient elastography, a technique based on a ultrasound echographic device, which detects the propagation of shear waves generated by a mechanical vibration system. They extracted Young's moduli of approximately 3.6-9.3 MPa for the skin composite and 9-30 kPa for the subcutaneous fat. The values found in this study are higher than those found in the present work, which could be caused by the use of a distinct mechanical experiment. Furthermore, it is not clear in which part of the non-linear stress-strain curve the Young's moduli were extracted. In addition, Vogt et al. (2003) used ultrasound elastography to obtain axial strain fields in the skin composite and the hypodermis from skin subjected to suction. In the future, those techniques might be adapted such that strain fields in the epidermis and eventually its mechanical properties can be extracted.

6.4 Optical coherence tomography and suction

A new device was introduced to study the contribution of the upper skin layers to the mechanical response of the skin. 1, 2 and 6 mm aperture suction experiments were combined with an optical coherence tomography system, which distinguishes the papillar dermis from the reticular dermis. Unlike ultrasound, OCT does not need a specific coupling liquid, and hence this technique is also suitable to examine the effects of hydration on the mechanical response of the skin layers. The intensity peaks associated with the skin surface and the papillar dermis-reticular dermis interface were automatically obtained from the OCT images to calculate skin surface displacements and thickness of the upper layer. The pressure-skin surface displacement curves for the 6 and 2 mm aperture diameter suction experiments were comparable to those from Diridollou et al. (2000) and Barel et al. (1995), and results from ultrasound measurements and OCT measurements using a 6 mm aperture diameter on hydrated skin were comparable. Changes in thickness of the upper layer due to loading were of the order of the resolution of the imaging systems and thus not resolvable. Material parameter identification with single layer finite element models for experiments with different aperture diameters resulted in increasing values for the material parameters with an increased aperture diameter.

The mechanical response of the upper layer could be separated from that of the reticular

dermis by combining experiments with different aperture diameters with a two layer finite element model. This verified the hypothesis that a combination of experiments of different length scales can be used to reveal the mechanical behaviour of separate skin layers. It was shown that the reticular dermis is much stiffer than the upper layer, although this result was fully explored for a single individual only.

Several aspects of this technique need to be improved. For example, the reproducibility of measurements at different sites should be thoroughly examined to verify the hypotheses that hydration leads to an increase in the measured displacements, and that this effect increases with smaller aperture diameter. Secondly, the stability of the finite element model needs to be improved to simulate all experiments at larger deformations and to examine the mechanical response of the upper layer of the skin for all subjects. Furthermore, the refractive index and the ultrasound velocity in the skin could alter as a direct result of the tissue deformation, causing deviations in the estimated displacements and thicknesses. Future research is required to quantify the alteration of the refractive index and the ultrasound velocity in the skin. Finally, the resolution of the OCT system of 14 μm did not allow the use of suction devices with an aperture diameter smaller than 1 mm. Consequently, an imaging system with improved resolution is needed to examine the mechanical behaviour of the stratum corneum.

6.5 Confocal microscopy and tension

To study deformations in the epidermal layers, a small tensile device was designed and coupled to a confocal microscope. Applied forces were measured with miniature strain gauges. An advantage of this device is the use of a guard ring, guaranteeing a distinct boundary of the loaded skin. Three-dimensional digital image correlation was successfully applied up to depths of 160 μm under the skin surface to acquire three-dimensional deformation and strain fields in the epidermis and papillar dermis. However, only about 30 % of the data points could be correctly identified, a problem particularly associated with areas exhibiting poor contrast. Due to the 'mountain and valley' structure of the skin, it was difficult to compare points in the same skin layer.

Although the technique is very promising, several improvements must be made to ensure that this technique will characterize the mechanical response of the epidermal layers. The performance of the DIC should be examined carefully for all depths under the skin surface by application of rigid translation to the skin, for example by movement of the microscope objective, or by considering skin-mimicking phantoms. In addition, the number of points traced with the DIC should be increased and the field of view in the experiment should be increased without diminishing the resolution, to obtain appropriate displacement and strain fields for the model. Furthermore, the initial distance between the pads (figure 5.3) should be decreased to increase the influence of the stratum corneum on the total mechanical response. Also, larger displacements are required to characterize the non-linear behaviour without making the experiment more time consuming. Finally, the topography of the skin surface should be incorporated in the finite element model.

6.6 Recommendations and future perspectives

The developed techniques demonstrated the potential to examine the contributions of the reticular dermis and the upper layer to the total mechanical response. Although the results of the performed experiments strongly suggest that it is possible to examine the mechanical behaviour of the different skin layers with the described methods, and that the epidermal stiffness is much smaller than the dermal stiffness, more experiments are needed to endorse these findings. Making the loading devices fully computer controlled and automatization of the data analyses and numerical simulations would facilitate such experiments.

To examine the mechanical behaviour of the stratum corneum and the living epidermis, experiments of smaller length scales are necessary. Material properties of stratum corneum could be established by performing suction or micropipette aspiration experiments (Alexopoulos et al., 2003) at aperture sizes in the order of 1 μm, or micro indentation experiments using tip diameters in the order of 1 μm. Material properties of the living epidermis could be established by performing suction or micropipette aspiration experiments at aperture sizes in the order of 10 μm, micro indentation using tip diameters in the order of 10 μm, or tensile experiments with initial pad distance smaller than approximately 0.5 mm. When modelling these experiments, also the micro-relief of the skin surface must be incorporated. To avoid meshing problems and large computation times due to the different length scales of the different skin layers, a multi-scale finite element model, combining models of different scales, may prove beneficial.

Ideally, measurements at different aperture sizes should be performed at the same site, without effects of previous testing, and without the effect of the removal of the tape attached to the load device. Since this may not be realistic, measurements should be performed either on different sites, or at different points in time. In both cases, an extensive study on the reproducibility of the measurements should be performed. This will also facilitate studies on the effect of hydration or skin diseases on skin mechanics. Finally, it would be interesting to perform experiments with dynamic loading situations and different loading types such as tension or torsion, to establish a series of material parameters in the developed finite element models.

The combined approach involving both experimental and numerical methods are likely to be a useful tool to study the mechanical behaviour of the skin in different circumstances, such as diseased skin or to study the effect of cosmetic treatments. The approach could be used to obtain thresholds for the material parameters of several layers. In that way, knowledge of the mechanical behaviour of the different layers of the skin can help to quantify the effectiveness of cosmetic products and to study which part of the skin is affected by them. It would also be interesting to examine the effect of ageing on the mechanical response of different skin layers and to investigate whether diseased skin like psoriatic skin, tumors or scars exhibit a different mechanical behaviour in any of the skin layers. Furthermore, the material parameters of the different skin layers can be used for the development of shavers. During shaving, the skin penetrates the slits of a shaver in which the hairs are cut. To enhance shaving performance, without damaging the skin, the hair must be cut close to the skin surface. To date, the influence of the top layer

on doming, which is defined as the penetration of the skin in the slits, was neglected in the finite element simulations that predict this doming, although the small length scale of the doming necessitates the inclusion of the top layers. Incorporating the mechanical behaviour of the upper layers in the simulation may enable a better development of shavers resulting in a better shaving performance without damaging the skin surface. Moreover, the use of hydrating additives might affect the mechanical behaviour of the top layer and thereby affect the doming.

Further clinical problems such as the development of pressure ulcers is a direct result of the breakdown at the interface between the skin and its external environment. Incorporation of detailed knowledge of the skin behaviour in the human (Oomens et al., 2003), animal (Bosboom, 2001), and multiscale models (Breuls, 2003), that are used to study pressure ulcers, may increase the understanding of the basic pathways associated with pressure-induced damage. Finally, results of cosmetic and plastic surgery may be predicted and improved by application of a finite element calculation based on patient specific data.

Bibliography

Agache, P., Monneur, C., Lévêque, J., De Rigal, J., 1980. Mechanical properties and young's modulus of human skin in vivo. Archives of Dermatological Research 269, 221–232.

Agner, T., 1995. Ultrasound A-mode measurement of skin-thickness. In: Serup, J. and Jemec, G.B.E. (eds.) Handbook of Non-Invasive Methods and the skin. Boca Raton, CRC Press.

Alexander, C., Cook, T., 1977. Accounting for the natural tension in the mechanical testing of human skin. The Journal of Investigative Dermatology 69, 310–314.

Alexopoulos, L., Haider, M., Vail, T., Guilak, F., 2003. Alterations in the mechanical properties of the human chondrocyte pericellular matrix with osteoarthritis. Journal of Biomechanical Engineering 125, 323–333.

Allaire, P., Thacker, J., Edlich, R., et al., 1977. Finite deformation theory for in vivo human skin. Journal of Bioengineering 1, 239–249.

Arruda, E., Boyce, M., 1993. A three-dimensional constitutive model for the large stretch behavior of rubber elastic materials. Journal of Mechanical Physics & Solids 41, 389–412.

Auriol, F., Vaillant, L., Machet, L., Diridollou, S., Lorette, G., 1993. Effects of short-time hydration on skin extensibility. Acta Derm Venereol. 73, 344–347.

Bader, D., Bowker, P., 1983. Mechanical characteristics of skin and underlying tissues in vivo. Biomaterials 4, 305–308.

Barbanel, J., 1979. Time dependent mechanical properties of skin., ph.D. thesis, University of Strathclyde, Glasgow.

Barbanel, J., Evans, J., J.B., F., 1972. Stress-strain-time relationships for soft connective tissues. In: Kennedi, K.M. (ed), Perspectives in Biomedical Engineering.

Barel, A., Courage, W., Clarys, P., 1995. Suction method for measurement of skin mechanical properties: the Cutometer. In: Serup, J. and Jemec, G.B.E. (eds.) Handbook of Non-Invasive Methods and the skin. Boca Raton, CRC Press.

Bisschoff, J., Arruda, E., Grosh, K., 2000. Finite element modelling of human skin using an isotropic, nonlinear elastic constitutive model. Journal of Biomechanics 33, 645–652.

Bosboom, E., 2001. Deformation as a trigger for pressure sore related muscle damage., ph.D. thesis, Maastricht University, The Netherlands.

Breuls, R., 2003. Experimental and theoretical analyses of compression induced muscle damage. aetiological factors in pressure ulcers., ph.D. thesis, Eindhoven University of Technology, The Netherlands.

Coleman, T., Branch, M., Grace, A., 1999. Optimization toolbox user's guide. For use with MATLAB. The Mathworks Inc.

Cook, T., 1976. An in plane method for determining the two dimensional stress-strain behavior of living human skin. In: Proceedings 29th ACEMB. Vol. 43.

Crisp, D., 1972. Properties of tendon and skin. In: Biomechanics: Its foundations and objectives. Fung YC, Perone N and Anliker M (eds). Prentice Hall, Englewood Cliffs. pp. 141–179.

Daly, C., 1982. Biomechanical properties of dermis. The Journal of Investigative Dermatology 79, 17s–20s.

Dines, K., Sheets, P., Brink, J., Hanke, C., Condra, K., Clendenon, J., Gross, S., Smith, D., Franklin, T., 1984. High frequency ultrasonic imaging of skin: experimental results. Ultrasonic imaging 6, 408–434.

Diridollou, S., Berson, M., Vabre, V., Black, D., Karlsson, B., Auriol, F., Gregoire, J., Yvon, C., Vaillant, L., Gall, Y., Patat, F., 1998. An in vivo method for measuring the mechanical properties of the skin using ultrasound. Ultrasound in Medicine & Biology 24 (2), 215–224.

Diridollou, S., Patat, F., Gens, F., Vaillant, L., Black, D., Lagarde, J., Gall, Y., Berson, M., 2000. In vivo model of the mechanical properties of the human skin under suction. Skin Research and Technology 6, 214–221.

Douven, L., 1999. Personal care institute, philips research eindhoven, personal communication.

Ebling, F., Eady, R., Leigh, I., 1992. Anatomy and organization of human skin. In: Champion, R.H., Burrington, J.L., Ebling, F.J.G. (eds), Textbook of Dermatology, 5th edition. Blackwell Scientific Publications, New York.

Edwards, C., Payne, P., 1984. Ultrasound velocities in skin components., international Society for Bioengineering and the Skin: ultrasound in dermatology. Symposium, Liege, Belgium.

El Gammal, S., Auer, T., Hoffman, K., Altmeyer, P., Passman, C., Ermert, H., 1995. High-resolution ultrasound of the human epidermis. In: Serup, J. and Jemec, G.B.E. (eds.) Handbook of Non-Invasive Methods and the skin. Boca Raton, CRC Press.

Elsner, P., Wilhelm, D., Maibach, H., 1990. Mechanical properties of human forearm and vulvar skin. British Journal of Dermatology 122, 607–614.

Escoffier, C., de Rigal, J., Rochefort, A., Vasselet, R., Lévêque, J., Agache, P., 1989. Age-related mechanical properties of human skin: An in vivo study. The Journal of Investigative Dermatology 93, 353–357.

Escoffier, C., Querleux, B., de Rigal, J., Lévêque, J., 1986. In vitro study of the velocity of ultrasound in the skin. Bioengineering and the skin 2, 87–94.

Finlay, B., 1969. Scanning electron microscopy of the human dermis under uni-axial strain. Bio-medical Engineering 4, 322–327.

Fung, Y., 1973. Biorheology of soft tissues. Biorheology 10, 139–155.

Fung, Y., 1981. Biomechanics. Mechanical properties of living tissues. Springer-Verlag, New York.

Geers, M., de Borst, R., Brekelmans, W., 1996. Computing strain fields from discrete displacement fields in 2d-solids. Int. Journal Solids Structures 33 (29), 4293–4307.

Gennisson, L., Baldeweck, T., Tanter, M., Catheline, S., Fink, M., L., S., Cornillon, C., Querleux, B., 2004. Assessment of elastic parameters of human skin using dynamic elastography. IEEE Trans Ultrason Ferroelectr Freq Control. 51 (8), 980–989.

Gill, P., Murray, W., Wright, M., 1981. Practical Optimization. Academic Press, California.

Ginefri, J., Darasse, L., Crozat, P., 2001. High-temperature superconducting surface coil for in vivo microimaging of the human skin. Magnetic Resonance in Medicine 45, 376–382.

Gladkova, N., Petrova, G., Nikulin, N., et al., 2000. In vivo optical coherence tomography imaging of human skin: norm and pathology. Skin Research and Technology 6, 6–16.

Gniadecka, M., Serup, J., 1995. Suction chamber method for measurement of skin mechanical properties: The Dermaflex. In: Serup, J. and Jemec, G.B.E. (eds.) Handbook of Non-Invasive Methods and the skin. Boca Raton, CRC Press.

Grahame, R., 1970. A method for measuring human skin elasticity in vivo with observations on the effects of age, sex and pregnancy. Clinical Science 39, 223–238.

Guyton, A., 1985. Anatomy and Physiology. Saunders College Publishing, New York.

Hendley, A. Marks, R., Payne, P., 1982. Measurement of forces for point indentation of the stratum corneum in vivo: the influences of age, sex, site delipidisation and hydration. Bioengineering and the Skin 3, 234–240.

Hendriks, F., Brokken, D., Oomens, C., Baaijens, F., 2004a. Influence of hydration and experimental length scale on the mechanical response of human skin *in vivo*, using optical coherence tomography. Skin Research and Technology 10, 231–241.

Hendriks, F., Brokken, D., Oomens, C., Bader, D., Baaijens, F., 2004b. The relative contributions of the different skin layers to the mechanical behaviour of human skin *in vivo* using suction experiments. Medical Engineering and Physics, *Submitted* .

Hendriks, F., Brokken, D., van Eemeren, J., Oomens, C., Baaijens, F., Horsten, J., 2003. A numerical-experimental method to characterize the non-linear mechanical behaviour of human skin. Skin Research and Technology 9, 274–283.

Hendriks, R., Lucassen, G., 2001. Two photon fluorescence and confocal video microscopy of in-vivo human skin. In: Proceedings SPIE BIOS 2001, 4262, 287–293.

Huang, D., Swanson, E., Lin, C., Schuman, J., Stinson, W., Chang, W., Hee, M., Flotte, T., Gergory, K., Puliafito, C., Fujimoto, J., 1991. Optical coherence tomography. Science 254, 1178–1181.

Hughes, T., 1987. The finite element method. Linear statistic and dynamic finite element analysis. Prentice-Hall.

Jemec, G., Gniadecka, M., Jemec, B., 1996. Measurement of skin mechanics. a study of inter- and intra- individual variation using the dermaflex a. Skin Research and Technology 2, 164–166.

Jemec, G., Jemec, B., Jemec, B., Serup, J., 1990. The effect of superficial hydration on the mechanical properties of human skin in vivo: Implication for plastical surgery. Plast. Reconstr. Surg. 85, 100–103.

Jemec, G., Serup, J., 1990. Epidermal hydration and skin mechanics. the relationship between electrical capacitance and the mechanical properties of human skin in vivo. Acta. Derm. Venereol. 70, 245–247.

Kirby, S., Wang, B., Solomon To, C., Lampe, H., 1998. Nonlinear three-dimensional finite element model of skin biomechanics. Journal of Otolaryngology 27 (3), 153–160.

Langer, K., 1861. Zur anatomie und physiologie de haut 1. ueber der spaltbarkeit der cutis. Sitzungsbericht der Akademie der Wissenschaften in Wien 44, 19.

Lanir, Y., 1979. A structural theory for the homogeneous bixial stress-strain relationships in flat collagenous tissues. Journal of Biomechanics 12, 423–436.

Lanir, Y., 1983. Constitutive equations for fibrous connective tissues. Journal of Biomechanics 16 (1), 1–12.

Lanir, Y., Fung, Y., 1974. Two-dimensional mechanical properties of rabbit skin. ii. experimental results. Journal of Biomechanics 7, 171–182.

Larrabee, W., Galt, J., 1986. A finite element model of skin deformation. iii. the finite element model. Laryngoscope .

Larrabee, W., Sutton, D., 1986. A finite element model of skin deformation. ii. an experimental mode of skin deformation. Laryngoscope .

Lenderink, E., Lucassen, G., van Kemenade, P., Steenwinkel, M., Vink, A., 2002. In vivo measurements of epidermal thickness with optical coherence tomography and confocal laser scanning microscopy: a comparison of methods. In: SPIE's BIOS 2002, California, USA. pp. 121–122.

Lucassen, G., Neerken, S., Hendriks, R., Caspers, P., Puppels, G., 2002. Confocal imaging and spectroscopy of human skin in vivo. Biomedical Topical Meeting, MA5-April 8, 2002, Miami Florida, USA .

Magrab, E., Azarm, S., Balachandran, B., Duncan, J., Herold, K., Walsh, K., 2000. An Engineer's Guide to MATLAB. Prentice Hall.

Manschot, J., 1985. The mechanical properties of human skin in vivo., ph.D. thesis, Catholic University of Nijmegen.

Manschot, J., Brakkee, A., 1986. The measurement and modelling of the mechanical properties of human skin in vivo - i. the measurement. Journal of Biomechanics 19 (7), 511–515.

Marcellier, H., Vescovo, P., Varchon, D., Vacher, P., Humbert, P., 2001. Optical analysis of displacement and strain fields on human skin. Skin Research and Technology 7, 246–253.

Marks, R., 1991. Mechanical Properties of the skin. In: Goldsmith, L.A. (editor) Physiology, biochemistry, and molecular biology of the skin. Oxford University Press, Oxford.

Maurel, W., Wu, Y., Magnenat Thalmann, N., Thalmann, D., 1998. Biomechanical Models for Soft Tissue Simulation. Esprit Basic Research Series. Springer-Verlag, Berlin.

Meijer, R., Douven, L., Oomens, C., 1999. Characterization of anisotropic and non-linear behaviour of human skin in vivo. Computer Methods in Biomechanics and Biomedical Engineering 1, 13–27.

MSC Software Corporation, A., 2000. Nonlinear finite element analysis of elastomers.

MSC Software Corporation, A., 2001. MSC.MARC, Volume A: Theory and user information, Version 2001.

Murray, B., Wickett, R., 1996. Sensivity of cutometer data to stratum corneum hydration level. a preliminary study. Skin Research and Technology 2, 167–172.

Neerken, S., Lucassen, G., Bisschop, M., Lenderink, E., Nuijs, T., 2003. Characterization of age-related effects in human skin: A comparative study applying confocal laser scanning microscopy and optical coherence tomography. Biomedical Optics, In Press .

Odland, G., 1991. Structure of the skin. In: Goldsmith, L.A. (editor) Physiology, biochemistry, and molecular biology of the skin. Oxford University Press, Oxford.

Oomens, C., Bressers, O., Bosboom, E., Bouten, C., Bader, D., 2003. Can loaded interface characteristics influence strain distributions in muscle adjacent to bony prominences? Computer Methods in Biomechanics and Biomedical Engineering 6, 171–180.

Oomens, C., Van Campen, D., Grootenboer, H., 1987. A mixture approach to the mechanics of skin. Journal of Biomechanics 20 (9), 877–885.

Oomens, C., Van Ratingen, M., Janssen, J., Kok, J., Hendriks, M., 1993. A numerical-experimental method for a mechanical characterization of biological materials. Journal of Biomechanics 26 (4/5), 617–621.

Oxlund, H., Manschot, J., Viidik, A., 1988. The role of elastin in the mechanical properties of skin. Journal of Biomechanics 21 (3), 213–218.

Pan, Y., Lankenau, E., Welzel, J., Birngruber, R., Engelhardt, R., 1996. Optical coherence-gated imaging of biological tissues. IEEE Journal of Selected Topics in Quantum Electronics 2 (4), 1029–1034.

Papir, Y., Hsu, K., Wildnauer, R., 1975. The mechanical properties of stratum corneum i. the effect of water and ambient temperature on the tensile properties of newborn rat stratum corneum. Biochimica et Biophysica Acta 399, 170–180.

Park, A., Baddiel, C., 1972. Rheology of stratum corneum i. a molecular interpretation of the stress-strain curve. Journal of the Society of Cosmetic Chemists 23, 3–12.

Peters, G., 1987. Tools for measurement of stress and strain fields in soft tissue, ph.D. thesis, Eindhoven University of Technology.

Piérard, G., Nikkels-Tassoudji, N., Piérard-Franchimont, C., 1995. Influence of the test area on the mechanical properties of skin. Dermatology 191, 9–15.

Querleux, B., 1995. Nuclear Magnetic Resonance (NMR) examination of the epidermis in vivo. In: Serup, J. and Jemec, G.B.E. (eds.) Handbook of Non-Invasive Methods and the skin. Boca Raton, CRC Press.

Rajadhyaksha, M., Anderson, R., Webb, R., 1999a. Video-rate confocal scanning laser microscope for imaging human tissues in vivo. Applied Optics .

Rajadhyaksha, M., González, S., Zavislan, J., Anderson, R., Webb, R., 1999b. In vivo confocal scanning laser microscopy of human skin ii: Advances in instrumentation and comparison with histology. The Journal of Investigative Dermatology .

Rajadhyaksha, M., Zavislan, J., 1997. Confocal laser microscope images tissue in vivo. Laser Focus World 33 (2), 119–128.

Retel, V., Vescovo, P., Jacquet, E., Trivaudey, F., Varchon, D., Burtheret, A., 2001. Nonlinear model of skin mechanical behaviour analysis with finite element method. Skin Research and Technology 7, 152–158.

Rigal, J. d., Lévêque, J., 1985. In vivo measurement of the stratum corneum elasticity. Bioengineering and the Skin 1, 13–23.

Rigal, J. d., Lévêque, J., Agache, P., Monneur, C., 1980. Influence of ageing on the in vivo extensibility of human skin at low stress. Archives of Dermatological Research 269, 127–135.

Rodrigues, L., the EEMCO group, 2001. Eemco guidance to the in vivo assessment of tensile functional properties of the skin. part ii: Instrumentation and test methods. Skin Pharmacology and Applied Skin Physiology 14, 52–67.

Schmitt, J., Yadlowski, M., Bonner, R., 1995. Subsurface imaging of living skin with optical coherence microscopy. Dermatology 191, 93–98.

Serup, J. ad Keiding, J., Fullerton, A., Gniadecka, M., Gniadecki, R., 1995. High-Frequency Ultrasound Examination of the skin: Introduction and Guide. In: Serup, J. and Jemec, G.B.E. (eds.) Handbook of Non-Invasive Methods and the skin. Boca Raton, CRC Press.

Sheppard, C., Shotton, D., 1997. Confocal Laser Scanning Microscopy. Royal Microscopical Society Microscopic Handbooks. Bios Scientific Publishers, Oxford.

Sol, H., Oomens, C. e., 1997. Material identification using mixed numerical-experimental methods. Proceedings of EUROMECH Colloquium, 7-9 april 1997, Kerkrade, The Netherlands. Kluwer Academic Publishers.

Sutton, M., Wolters, W., Peters III, W., Ranson, W., McNeill, S., 1983. Determination of displacements using an improved digital correlation method. Image and Vision Computing 1, 133–139.

Tearney, G., Brezinski, M., Southern, J., Bouma, B., Hee, M., Fujimoto, J., 1995. Determination of the refractive index of highly scattering human tissue by optical coherence tomography. Optics Letters. 20, 2258–2260.

Tong, P., Fung, Y., 1976. The stress-strain relationship for the skin. Journal of Biomechanics 9, 649–657.

Verhulp, E., van Rietbergen, B., Huiskes, R., 2004. A three-dimensional difital image correlation technique fir strain measurements in microstructures. Journal of Biomechanics 37 (9), 1313–1320.

Veronda, D., Westman, R., 1970. Mechanical characterization of skin - finite deformations. Journal of Biomechanics 3, 111–124.

Vlasblom, D., 1967. Skin elasticity, ph.D. thesis, Catholic University of Utrecht.

Vogt, M., Scharenberg, S., Scharenberg, R., Hoffmann, K., Altmeyer, P., Ermert, H., 2003. A high frequency ultrasound elastography system for in vivo skin elasticity imaging. In: Proceedings of the World Congress on Ultrasonics 2003, Paris, France. pp. 393–396.

Wan Abas, W., Barbanel, J., 1982. Uniaxial tension test of human skin in vivo. Journal of Biomedical Engineering 4.

Welzel, J., Lankenau, E., Birngruber, R., Engelhardt, R., 1998. Optical coherence tomography of the skin. Current Problems in Dermatology 26, 27–37.

Wijn, P., 1980. The alinear viscoelastic properties of human skin in vivo for small deformations., ph.D. thesis, Catholic University of Nijmegen.

Wildnauer, R., Bothwell, J., Douglass, A., 1971. Stratum corneum biomechanical properties. i. influence of relative humidity on normal and extracted human stratum corneum. The Journal of Investigative Dermatology 56 (1), 72–78.

Wilkes, G., Brown, I., Wildnauer, R., 1973. The biomechanical properties of skin. Critical Reviews in Bioengineering , 453–495.

Zemtsov, A., 1995. Nuclear Magnetic Resonance (NMR) examination of the skin. In: Serup, J. and Jemec, G.B.E. (eds.) Handbook of Non-Invasive Methods and the skin. Boca Raton, CRC Press.

Samenvatting

De huid is het grootste orgaan van het menselijk lichaam. Het mechanische gedrag van de huid wordt sinds geruime tijd onderzocht. Kennis hiervan is van belang voor zowel cosmetische als klinische toepassingen zoals de ontwikkeling van crèmes en producten voor persoonlijke verzorging, of voor het begrijpen van huidziekten en huidveroudering.

Vooral kennis van de mechanica van de epidermis, de meest oppervlakkige laag, is cruciaal, omdat de epidermis in contact staat met cosmetische producten en omdat huidziekten zich openbaren in deze laag. Verder wordt het mechanische gedrag van de epidermis sterk beïnvloed door omgevingsfactoren zoals temperatuur en relatieve vochtigheid. Aangezien de toplaag *in vivo* ook gehydrateerd wordt door de diepere huidlagen, moet het mechanisch gedrag in een niet-invasieve studie onderzocht worden.

Er zijn verschillende mechanische experimenten gedaan op de huid en verschillende numerieke modellen voorgesteld om het mechanische gedrag te beschrijven. Een algemeen kenmerk van deze studies is de aanname dat het gedrag van de huid gedomineerd wordt door de collageen-rijke dermis. De bijdrage van de epidermis, die een andere structuur heeft, wordt meestal verwaarloosd.

Het doel van deze studie is het mechanisch gedrag van de verschillende lagen van de huid, inclusief de toplagen, *in vivo* te onderzoeken. Het werk is gebaseerd op de hypothese dat een combinatie van suctie-experimenten met verschillende gatdiameters gebruikt kan worden om het mechanisch gedrag van de verschillende huidlagen te karakteriseren. Oftewel, met een kleine gatdiameter kan het gedrag van de meest oppervlakkige lagen bestudeerd worden, terwijl een grote gatdiameter goed werkt voor het gedrag van de dieper liggende lagen.

Om de vervorming in de huid te visualiseren zijn drie experimentele opstellingen ontwikkeld die een mechanisch experiment en een beeldvormende techniek combineren. Elke opstelling is gebruikt om verschillende huidlagen te bestuderen. Om de experimenten te simuleren en het mechanisch gedrag van de verschillende lagen te karakteriseren zijn verschillende eindige elementen modellen ontwikkeld. Teneinde het mechanisch gedrag van de gecombineerde dermis en epidermis en het onderhuids vet te bestuderen is een suctie-apparaat met een gatdiameter van 6 mm gekoppeld met een ultrasound systeem. Op de huid van de onderarm van 10 proefpersonen van 19 tot 24 jaar zijn suctie-metingen met verschillende drukken uitgevoerd. De experimenten zijn gesimuleerd met een eindige elementen model waarin een 'extended Mooney' constitutieve vergelijking is gebruikt om het niet-lineaire gedrag van de huid te beschrijven. De materiaalparameters van het

model zijn bepaald met een identificatie procedure die de experimentele en numerieke resultaten vergelijkt. Dit resulteerde in $C_{10} = 9.4 \pm 3.6$ kPa en $C_{11} = 82 \pm 60$ kPa voor de gecombineerde dermis en epidermis. Een eerste schatting voor de stijfheid van vet leidde tot $C_{10,vet} = 0.02$ kPa.

De bijdrage van de epidermis aan de totale mechanische respons van de huid is onderzocht met een suctie-apparaat met 1, 2 en 6 mm gatdiameter. Op de huid van de onderarm van 13 proefpersonen van 29 tot 47 jaar oud zijn suctie-metingen met verschillende drukken en gat diameters uitgevoerd. De deformatie van de gecombineerde dermis en epidermis is in kaart gebracht met ultrasound, de deformatie van de epidermis en papillair dermis met optical coherence tomography (OCT). Het effect van hydratatie is onderzocht door ultrasound metingen met 6 mm gatdiameter uit te voeren op gehydrateerde huid en door OCT metingen met 1, 2 en 6 mm gatdiameter op zowel droge als gehydrateerde huid uit te voeren. Het effect van hydratatie op de mechanische respons was onduidelijk. De experimenten zijn gesimuleerd met een eindige elementen model bestaande uit één laag (gecombineerde dermis en epidermis) en gebruikmakend van een 'extended Mooney' constitutieve vergelijking. Uit deze experimenten bleek dat de combinatie van experimenten met verschillende gatdiameters gebruikt kan worden om het mechanisch gedrag van verschillende huidlagen te onderscheiden. Een toenemende gatdiameter leidt tot grotere waarden voor de materiaalparameters, hoewel in alle gevallen hetzelfde materiaal gemodelleerd is.

Daarom zijn de experimenten voor kleine verplaatsingen gemodelleerd met een model dat bestond uit twee lagen: de reticulaire dermis en de gecombineerde epidermis en papillaire dermis. De materiaalparameters voor beide lagen die met dit model gevonden werden verschilden sterk: $C_{10,rd} = 0.16$ MPa and $C_{10,ed+pd} = 0.11$ kPa. Het twee-laags model was in staat de 1 en 6 mm experimenten correct te beschrijven, in tegenstelling tot het experiment met 2 mm gatdiameter. Echter, deze resultaten zijn slechts voor één proefpersoon volledig onderzocht vanwege numerieke problemen. Het softwarepakket dat het twee-laags model ondersteunde, bleek niet in staat de grote vervormingen die bij sommige proefpersonen gemeten zijn te beschrijven als gevolg van het grote verschil in stijfheid tussen beide lagen.

Omdat de resolutie van het OCT systeem het gebruik van kleinere gatdiameters niet toeliet, werd er teneinde de vervormingen in de epidermale lagen te bestuderen een klein trekapparaatje ontwikkeld dat gekoppeld werd aan een confocale microscoop. Met drie-dimensionale beeldcorrelatie zijn drie-dimensionale deformatie- en rekvelden met succes verkregen uit de confocale beelden van de epidermis en de papillaire dermis tot een diepte van 160 μm onder het huidoppervlak. Hoewel de techniek veelbelovend is, zijn er nog verschillende verbeteringen nodig om de techniek geschikt te maken om het mechanisch gedrag van de epidermale lagen te karakteriseren.

Samenvattend kan geconcludeerd worden dat de in deze studie ontwikkelde technieken die erop gericht zijn experimenten van verschillende lengteschalen te combineren, succesvol blijken in het onderscheiden van het mechanisch gedrag van verschillende lagen van de huid, inclusief de oppervlakkige lagen.

Dankwoord

Graag wil ik iedereen bedanken die een bijdrage heeft geleverd aan dit proefschrift.
Allereerst wil ik Cees Oomens en Dirk Brokken bedanken voor hun begeleiding, enthousiasme en betrokkenheid. Cees, bedankt ook voor je goede raad en luisterend oor. Dirk, bedankt voor je hulp met slimme computer weetjes. Ook dank ik Joost Horsten en Frank Baaijens, die door hun samenwerking dit onderzoek mogelijk maakten en die hun licht lieten schijnen over de inhoudelijke lijnen van het onderzoek. Frank, Cees en Dirk, bedankt voor het vertrouwen dat jullie stelden in de goede afloop van mijn onderzoek.
Dan Bader, thank you for your contribution to the contents of this thesis, the fruitful discussions on my research and your beautiful English.
Mannen van de werkplaats, Piet, Ben, Henk en Arjan hartelijk dank voor jullie inzet en ideeën die leidden tot prachtige experimentele opstellingen.
De afstudeersters en stagiair(e)s, Judith Schuurman, Eva Korthagen, Petra van den Berg, Mark van Turnhout en Martijn Froeling dank ik voor hun bijdrage aan het onderzoek. Eelco Verhulp wil ik danken voor zijn hulp bij het gebruiken en verder ontwikkelen van de digital image correlation software. Henrike, dank je wel voor het gewillig proefpersoon spelen tijdens de voorbereiding van mijn experimenten en de lunchwandelingen. Johan, hartelijk bedankt voor je hulp bij het uitvoeren van de eerste paneltest. Gerald, Tom en Sigi, bedankt voor de hulp met alle beeldvormende technieken. Patricia, dank je wel voor de hulp bij het opzetten van de panelexperimenten. Judith de Goede, bedankt voor het mechanisch testen van de tape.
Al mijn kamergenoten, en in het bijzonder Marco, Michiel en Frank, dank ik voor alle praktische hulp, het aanhoren van mijn frustraties en overwinningen en de gezelligheid.
Tenslotte wil ik mijn familie en vrienden bedanken voor de nodige ontspanning door etentjes, spelletjes en wandelingen. Mijn kleine vriendjes maakten het makkelijk om alles in een ander licht te zien dankzij hun kinderlijke nieuwsgierigheid, voortreffelijk eenvoudige logica en hun heerlijke enthousiasme. Wim en Joke, bedankt voor alle hulp, de bijna wekelijkse etentjes en de bijbehorende ontspanning. Pap en mam, bedankt voor jullie onvoorwaardelijke steun, alle discussies en wijsheid. Sterre, wat ben je een lieve meid. En natuurlijk Ronald, naar jou gaat de grootste dank. Als team en met jouw steun en liefde is het ons gelukt.

Falke Hendriks
Eindhoven, oktober 2004

Curriculum Vitæ

Falke Hendriks werd geboren op 2 juli 1976 te Sittard. In 1994 behaalde zij haar Gymnasium diploma aan het College Sittard (tegenwoordig Trevianum). Daarna vervolgde ze haar opleiding aan de Technische Universiteit in Eindhoven. Na de propaedeuse Werktuigbouwkunde rondde ze in juli 1999 de postpropedeutische opleiding Werktuigkundige Medische Technologie af. Haar afstudeerproject bestond uit een experimenteel deel waarin de passieve transversale stijfheid van spiercellen van slangen werd bestudeerd, uitgevoerd aan de Washington University in St. Louis (USA), en een numeriek deel waarin de viabiliteit van spiercellen onder compressie werd bestudeerd. Vanwege haar interesse in het onderzoek naar de biomechanica van zachte weefsels, besloot zij verder te gaan met een promotie-onderzoek. Dit proefschrift is het resultaat van haar onderzoek dat viel binnen een samenwerkingsverband tussen de Technische Universiteit Eindhoven en het Personal Care Institute van Philips NatLab.
Sinds januari 2005 is zij werkzaam als development engineer bij TNO Automotive in Helmond.